THEORETICAL PERFORMANCE BOUNDS FOR THE ESTIMATION OF TARGET PARAMETERS FROM ELECTROMAGNETIC INDUCTION DATA

A Dissertation
Presented to
The Academic Faculty

By

Andrew J. Kerr

In Partial Fulfillment
of the Requirements for the Degree
Doctor of Philosophy in the
School of Electrical and Computer Engineering

Georgia Institute of Technology

May 2020

THEORETICAL PERFORMANCE BOUNDS FOR THE ESTIMATION OF TARGET PARAMETERS FROM ELECTROMAGNETIC INDUCTION DATA

Approved by:

Dr. Waymond Scott Jr., Advisor
School of Electrical and Computer Engineering
Georgia Institute of Technology

Dr. James McClellan, Advisor
School of Electrical and Computer Engineering
Georgia Institute of Technology

Dr. Aaron Lanterman
School of Electrical and Computer Engineering
Georgia Institute of Technology

Dr. Gregory Durgin
School of Electrical and Computer Engineering
Georgia Institute of Technology

Dr. Morris Cohen
School of Electrical and Computer Engineering
Georgia Institute of Technology

Dr. Yao Xie
School of Industrial and Systems Engineering
Georgia Institute of Technology

Date Approved: April 21, 2020

To my soon-to-be-wife Cali, my family, and my friends.

ACKNOWLEDGEMENTS

There are a number of people I would like to thank for their support in completing this thesis. First and foremost, I would like to thank my advisors Dr. Waymond Scott and Dr. Jim McClellan for their advice and encouragement throughout the Ph.D. process. I learned a tremendous amount from each of them over the last six years and am extremely appreciative and grateful for the time they spent mentoring me.

I would also like to thank my soon-to-be wife Cali Robocker for her love, support, and encouragement during this journey that was filled with its ups and downs. Without her, I certainly would not have made it this far. I think she might be more excited than me about my thesis being completed.

Thank you to my parents Jeff and Sallie for all the sacrifices they made over the past 28 years that allowed me to make it this far, and for encouraging me to strive for more than I thought I was capable of.

I am also extremely appreciative of the friends I made in graduate school. In particular, I would like to acknowledge Dr. Motaz Alfarraj who helped me survive my first semester at Georgia Tech and who became a very dear friend of mine. Additionally, I would like to thank my lab-mates Ethan Hayes and Dr. Yoni Gabbay. I was fortunate to have my graduate studies overlap with theirs and am thankful for their friendships and the things I learned from each of them.

I also owe a debt of gratitude to too many people at the Georgia Tech Research Institute to list. However, I would like to give special mention to my boss for the past 6 years, Dr. Scott D. Berger, for his guidance, patience, and flexibility as I tried to balance work with school (and I did not always balance them well).

A special thank you to my good friends and colleagues Christopher Weeks and Breneman Whitfield for reading (suffering?) through my draft journal papers and making sure that I got out of my office every once in a while.

Additionally, I would like to thank my childhood friends Omar Haque, MD, and Bryan Haywood for their support over the past six years as I pursued this degree. I wasn't (and still am not) entirely convinced they knew what I was researching, but they were supportive nonetheless, especially when things were difficult.

Lastly, I would like to thank the Georgia Tech Research Institute for their financial support in the last year of my Ph.D. studies. Without their support, completing this degree would likely have taken another 2+ years to finish. Finally, I would like to thank the Army Night Vision and Electronic Sensors Directorate for their financial support of this work.

TABLE OF CONTENTS

LIST OF FIGURES

SUMMARY

Electromagnetic induction (EMI) sensors are widely used for buried target detection and classification. One important application is their use in the humanitarian demining of landmines. It is estimated that there are around 50 to 100 million anti-personnel landmines in more than 80 countries around the world, and that these mines kill or injure a person every 20 minutes [1].

These sensors function by transmitting a time-varying magnetic field into the ground and measuring the induced response from metallic objects due to the field. EMI sensors are able to detect shrapnel, nails, mines, and other small pieces of metallic clutter. Consequently, it is important to be able to discriminate between clutter and actual targets of interest. Fortunately, there are many target-dependent parameters that can be estimated from EMI measurements and used for target classification. These include the target tensors and the associated relaxation frequencies, equivalent to decay rates in the time domain. The ability to estimate these target parameters, along with its location, is critical for accurately identifying and mitigating buried landmines, which is why the estimation of these unknown parameters continues to be of high interest to the EMI community [2, 3, 4, 5, 6, 7, 8, 9, 10, 11].

The objective of this research is to derive and analyze the theoretical performance bounds for the variance of any unbiased estimator (i.e. Cramer-Rao lower bounds) of these target parameters given a set of EMI measurements of a target. The goal is to provide a framework for assessing the performance of current and future EMI systems and to generate a benchmark for current estimation techniques of these parameters. The framework and corresponding analysis will provide a better understanding of the factors that influence these bounds, giving researchers additional insight to develop better EMI systems and estimators.

CHAPTER 1

INTRODUCTION

1.1 Motivation

Electromagnetic induction (EMI) sensors are widely used for buried target detection and classification. One important application is their use in the humanitarian demining of landmines. It is estimated that there are around 50 to 100 million anti-personnel landmines in more than 80 countries around the world, and that these mines kill or injure a person every 20 minutes [1].

These sensors function by transmitting a time-varying magnetic field into the ground which excites currents in nearby conducting media. These currents induce a secondary magnetic field that can be measured using a receive sensor. This operating principle of electromagnetic induction sensors is shown in Figure 1.1.

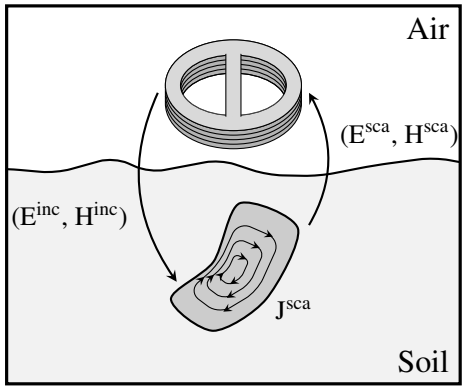

Figure 1.1: The operating principle of an EMI sensor. Illuminating a conductor with a time-varying magnetic field, H^{inc}, causes eddy currents, J^{sca}, to flow in conducting media. According to Lenz's law, these eddy currents induce a scattered magnetic field, H^{sca}, that opposes the magnetic excitation, and are characterized by exponential decay in time. Graphic and caption from [12], used with permission.

There are two classes of electromagnetic induction sensors: time-domain and frequency-domain. Time-domain sensors operate by exciting eddy currents in conducting media using

a high power step response and measuring the secondary magnetic field over time as the eddy currents discharge. On the other hand, frequency-domain sensors operate by exciting eddy currents in conducting media using a periodic, time-varying magnetic field at a chosen frequency or set of frequencies and measuring the induced response at each frequency.

In addition to the two different classes of sensors, EMI systems can differ in sensor configuration. For example, the Georgia Tech experimental handheld EMI system uses a single transmit-receive coil pair that is scanned across an area of interest [13]. Another Georgia Tech system uses a single transmit sensor with multiple receive sensors (i.e., receive array) to survey an area [14]. Alternatively, the Time-Domain Electro-Magnetic Multi-sensor Towed Array Detection system (TEMTADS) uses a multistatic configuration of 25 transmit sensors and 25 receive sensors, where each transmit coil transmits in succession, and all receive sensors receive for each transmission [15]. These sensors are shown in Figure 1.2.

Regardless of the sensing modality or configuration, these systems ultimately use temporal/frequency and spatial degrees of freedom (i.e., multiple measurement positions) to detect, localize, and classify buried targets. As pointed out in [16], the most difficult task in humanitarian demining is typically discriminating between clutter and actual targets of interest. Fortunately, there are many target-dependent parameters that can be estimated from EMI measurements and used for target classification. These include the target tensors and the associated relaxation frequencies, equivalent to decay rates in the time-domain. The ability to estimate these target parameters, along with its location, is critical for accurately identifying and mitigating buried landmines, which is why the estimation of these unknown parameters has been and continues to be of high interest to the EMI community[2, 3, 4, 6, 7, 8, 9, 10, 11, 17, 18].

Despite the abundance of research on developing algorithms for parameter estimation and target classification, there is comparatively little research attempting to quantify theoretical performance bounds for estimators of these parameters. This is especially true for

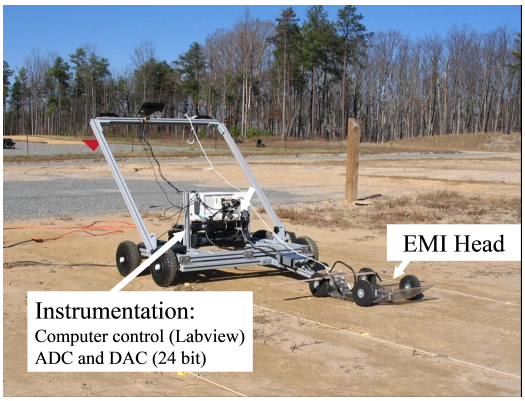

(a) Experimental GT frequency-domain system with a single transmit and a single receive channel.

(b) Experimental GT frequency-domain system with a single transmit channel and three receive channels.

(c) TEMTADS, a 5×5 array time-domain system with 25 transmit and 25 receive channels.

Figure 1.2: Three example EMI systems.

frequency-domain EMI systems, where to the author's knowledge there have been no published studies on the topic at the time of this thesis. For time-domain systems, there are a few research papers that focus on Cramer-Rao bounds for estimating target decay rates [5][19].

As such, the objective of this research is to derive and analyze the theoretical performance bounds for the variance of any unbiased estimator (i.e. Cramer-Rao bounds) of these target parameters given a set of EMI measurements, with an emphasis on frequency-domain EMI systems. The goal is to provide a framework for assessing the performance of current and future EMI systems and to generate a benchmark for current estimators of these parameters. The framework and corresponding analysis will provide a better understanding

of the factors that influence these bounds, giving researchers additional insight and tools to develop better signal processing algorithms, sensors, and EMI systems.

1.2 Thesis Organization

This thesis is organized into nine chapters. **Chapter 1** motivates the research topic and describes the organization of the thesis. In **Chapter 2** we describe the necessary background material including the Cramer-Rao lower bound, maximum likelihood estimation, and two equivalent but distinct forms of the signal model for describing electromagnetic induction measurements of a target made with a frequency-domain EMI system. The two signal model forms are the *sum of dipoles* (SoD) form and the *sum of tensors* (SoT) form. In **Chapter 3** we derive and validate the Cramer-Rao lower bounds for the unknown target parameters under the SoD form of the signal model. The bounds derived in this chapter directly correspond to physical target parameters, but are not immediately related to current processing algorithms for EMI data because these algorithms take advantage of a more efficient representation of the target (i.e., the SoT form) which requires either the same or fewer unknowns to model the same target. In **Chapter 4**, we derive the Cramer-Rao lower bounds for the unknown target parameters associated with the SoT form of the signal model for rank-one targets — a special class of targets that can be described using a single independent tensor. The signal model for a rank-one target allows for a simpler treatment of the derivation and a direct connection with the signal processing techniques used for processing EMI data. In **Chapter 5**, we describe a signal processing technique that uses the SVD to factor EMI measurements into separate frequency and spatial responses. We illustrate how this factorization relates to the SoT form of the signal model, and then compare the maximum likelihood estimator performance of the unknown parameters in the factored response to the CRBs under the SoT model from Chapter 4 for different example targets. In **Chapter 6**, we use the connection between the factored models from Chapter 5 and the Cramer-Rao bounds from Chapter 4 to derive approximate Cramer-Rao lower

bound expressions that are simpler and more insightful than the CRB expressions in Chapter 5. In **Chapter 7**, we perform different analyses using the approximate Cramer-Rao lower bound expressions from Chapter 6. These analyses provide a variety of insights into the factors that impact the bounds of the unknown parameters. In **Chapter 8**, we extend the derivation of Chapter 6 from rank-one targets to targets of arbitrary rank, removing any restriction on the number of independent tensors required to model the target. In **Chapter 9**, we summarize the contributions of the thesis and suggest areas for future work.

CHAPTER 2
BACKGROUND

In this chapter, we provide the background material for this thesis. The background material begins with an overview of the Cramer-Rao lower bound (CRB) and maximum likelihood estimation. The discussion of the CRB motivates the need to introduce and to develop the physics-based signal model for frequency-domain electromagnetic induction measurements of a target. We develop two forms of the signal model: the sum of dipoles (SoD) form, which directly connects to the physical target parameters we are interested in estimating, as well as the sum of tensors (SoT) form, which better connects to how EMI data is processed. To provide context and to develop a more concrete understanding of the two different forms of the signal model, we exercise the signal models for three different targets as examples. Lastly, we discuss the unknown target parameters we are interested in estimating in the context of classification.

2.1 Cramer-Rao Lower Bound

In this thesis, it is of interest to quantify how well (in the variance sense) the unknown target parameters can be estimated given a set of EMI measurements of the target. The unknown target parameters, which are fully introduced in Section 2.3.1, are the target tensors $\boldsymbol{t}_p$, the target location $\boldsymbol{l}_t$, and the relaxation frequencies ζ_p.

A widely accepted lower bound on the variance of unbiased estimators is the Cramer-Rao lower bound (CRB) [20], which is the performance measure that we focus on in this thesis. The CRB is useful because it provides a benchmark for comparison for any unbiased estimator, and it allows us to determine if an estimator exists that achieves the bound. The CRB is also the easiest of the variance bounds in the literature to compute [20].

For a vector parameter of unknowns $\boldsymbol{\theta}$, as is the case for EMI targets, the CRB for a

given parameter θ_i in $\boldsymbol{\theta}$ is

$$\mathrm{CRB}(\theta_i) = \left[\boldsymbol{I}^{-1}(\boldsymbol{\theta})\right]_{\mathrm{ii}} \tag{2.1}$$

where $\boldsymbol{I}^{-1}(\boldsymbol{\theta})$ is the inverse of the Fisher information matrix (FIM). The expression in (2.1) is then related to any unbiased estimator of $\hat{\theta}_i$ as $\mathrm{Var}(\hat{\theta}_i) \geq \mathrm{CRB}(\theta_i)$.

Thus, in order to calculate the CRBs, we need to calculate the entries in FIM. The ij entry of the FIM is defined as

$$[\boldsymbol{I}(\boldsymbol{\theta})]_{\mathrm{ij}} = -\mathbb{E}\left[\frac{\partial^2 \ln p(\boldsymbol{m};\boldsymbol{\theta})}{\partial\theta_i \partial\theta_j}\right] \tag{2.2}$$

where $p(\boldsymbol{m};\boldsymbol{\theta})$ is the probability density function (PDF) (i.e., likelihood function) of the measured data $\boldsymbol{m}$. This PDF is a function of the noise model used to describe the measured data as well the signal model $\boldsymbol{r}(\boldsymbol{\theta})$ describing how the signal model $\boldsymbol{r}$ changes as a function of the unknown parameters $\boldsymbol{\theta}$.

When a zero-mean independent, identically distributed complex white Gaussian noise model is assumed for a complex measurement, the likelihood function takes the general form in (2.3).

$$p(\boldsymbol{m};\boldsymbol{\theta}) = \frac{1}{(\pi\sigma_n^2)^N} \cdot \exp\left\{\frac{1}{\sigma_n^2}\left[\boldsymbol{m} - \boldsymbol{r}(\boldsymbol{\theta})\right]^H \left[\boldsymbol{m} - \boldsymbol{r}(\boldsymbol{\theta})\right]\right\} \tag{2.3}$$

where N is the dimensionality of the signal model and measurement, and σ_n^2 is the noise variance. In other words, $\boldsymbol{m} \in \mathbb{C}^{N\times 1}$ and $\boldsymbol{r} \in \mathbb{C}^{N\times 1}$. When the likelihood function is of the form in (2.3), a general expression for the FIM can be written as shown in (2.4).

$$[\boldsymbol{I}(\boldsymbol{\theta})]_{ij} = \frac{2}{\sigma_n^2}\,\mathrm{Re}\left\{\left(\frac{\partial \boldsymbol{r}(\boldsymbol{\theta})}{\partial\theta_i}\right)^H \left(\frac{\partial \boldsymbol{r}(\boldsymbol{\theta})}{\partial\theta_j}\right)\right\} \tag{2.4}$$

In summary, once the signal model is defined, computing the CRBs for a vector parameter of unknowns in the zero-mean i.i.d. Gaussian noise case involves taking partial derivatives of the signal model with respect to the unknown parameters to compute the en-

tries of the FIM, and then inverting this FIM. The CRB can be calculated as a function of the different model parameters, measurement parameters, as well as signal-to-noise ratio, as examples.

2.2 Maximum Likelihood Estimation

A closely related topic to the CRB is maximum likelihood estimation. A maximum likelihood estimate is defined as the estimate of the unknown parameters $\hat{\boldsymbol{\theta}}$ that maximizes the likelihood function $p(\boldsymbol{m};\boldsymbol{\theta})$. Maximum likelihood estimators (MLEs) are closely connected to CRBs because they have the asymptotic properties of being unbiased, achieving the CRB, and having a Gaussian PDF, and as such are described as asymptotically optimal [20]. For a vector parameter of unknowns, these asymptotic properties can be described succinctly as

$$\hat{\boldsymbol{\theta}}_{MLE} \overset{a}{\sim} N\left(\boldsymbol{\theta}, \boldsymbol{I}^{-1}(\boldsymbol{\theta})\right) \tag{2.5}$$

where $\boldsymbol{I}^{-1}(\boldsymbol{\theta})$ is the inverse of the FIM and $\overset{a}{\sim}$ indicates the asymptotic distribution.

These properties of the MLE can be numerically captured using Monte Carlo simulations, allowing one to validate the CRB derivations and the subsequent results via simulation. As such, it is important to understand the mathematical form of the MLE in the Gaussian noise case. As mentioned previously, the MLE is the value of $\boldsymbol{\theta}$ that maximizes the likelihood function $p(\boldsymbol{m};\boldsymbol{\theta})$. Maximizing the likelihood function is equivalent to minimizing the argument of the exponential in (2.3), which can be written as a cost function $\boldsymbol{C}(\boldsymbol{\theta})$, shown in multiple forms in (2.6).

$$\boldsymbol{C}(\boldsymbol{\theta}) = (\boldsymbol{m} - \boldsymbol{r}(\boldsymbol{\theta}))^H (\boldsymbol{m} - \boldsymbol{r}(\boldsymbol{\theta})) = \|\boldsymbol{m} - \boldsymbol{r}(\boldsymbol{\theta})\|_2^2 \tag{2.6}$$

A variety of optimization techniques exist for solving (2.6). The most common include grid searches over the possible values of $\boldsymbol{\theta}$ as well as iterative methods like gradient descent. In this thesis, we often make use of the built-in MATLAB function fminsearch$(\cdot)$ which

uses the Nelder-Mead simplex method [21].

In this thesis, we use Monte Carlo analysis to estimate the asymptotic distribution of the MLE in (2.5). The general procedure behind the Monte Carlo analysis is to generate many measurement realizations and estimate the unknown parameters using the MLE in (2.6). If enough realizations are generated, the sample covariance matrix generated from the maximum likelihood estimates will be nearly equal to the analytic calculation of $\boldsymbol{I}^{-1}(\boldsymbol{\theta})$, thus allowing one to validate the derived CRBs.

2.3 Frequency-Domain EMI Signal Models

In this section, we introduce the signal models used to describe the physical interaction between frequency-domain EMI sensors and metallic objects. The chapter begins by describing the target response of a metallic object subjected to a magnetic field at a single transmit frequency and a single spatial position. This response serves as the building block for the mathematical framework that is subsequently developed to describe the response of a metallic target subjected to a magnetic field at *multiple* transmit frequencies and *multiple* spatial positions, which is how many frequency-domain EMI systems operate. We first present the sum of dipoles form of the signal model, and then show how it relates to the sum of tensors form.

2.3.1 Sum of Dipoles Form of the Signal Model

EMI sensors for target detection and identification operate by transmitting a time-varying magnetic field into the ground. When a target is subjected to this field, a magnetic dipole moment is generated on the target due to both eddy currents and the bulk magnetic permeability of the target. The magnetic dipole moment induces a secondary magnetic field that can then be measured by a receive coil. This interaction can be modeled using reciprocity [22].

Assuming a point target where a sum of dipoles model can be used to model the

magnetic polarizability of the target, the complex response r of the system for a single transmitter-receiver (T-R) position relative to the target location, $\boldsymbol{l}_T - \boldsymbol{l}_t$ and $\boldsymbol{l}_R - \boldsymbol{l}_t$, and at one transmit frequency ω can be written as

$$r(\omega, \boldsymbol{l}_T, \boldsymbol{l}_R, \boldsymbol{l}_t) = \boldsymbol{h}_R^T(\boldsymbol{l}_R - \boldsymbol{l}_t)\boldsymbol{T}(\omega)\boldsymbol{h}_T(\boldsymbol{l}_T - \boldsymbol{l}_t) \tag{2.7}$$

The vectors $\boldsymbol{h}_R,\ \boldsymbol{h}_T \in \mathbb{R}^{3\times 1}$ contain the Cartesian components of the received and transmitted magnetic fields, respectively, that are computed using the Biot-Savart law from the geometry of the coils used in the sensor. In (2.7), multiple real constants have been folded into $\boldsymbol{h}_R$.

The *symmetric* matrix $\boldsymbol{T}(\omega) \in \mathbb{C}^{3\times 3}$ is the magnetic polarizability of the target which can be expanded as

$$\boldsymbol{T}(\omega) = \boldsymbol{T}_0 - \sum_{p=1}^{P} \frac{j\omega/\zeta_p}{1 + j\omega/\zeta_p}\boldsymbol{T}_p \tag{2.8}$$

where $\zeta_p \in \mathbb{R}$ is the p^{th} relaxation frequency corresponding to the p^{th} tensor $\boldsymbol{T}_p \in \mathbb{R}^{3\times 3}$, which represents the strength and direction of the p-th magnetic dipole. The tensors $\boldsymbol{T}_p$ are positive semi-definite, frequency independent, and due to the eddy currents induced on the target [23]. The tensor $\boldsymbol{T}_0 \in \mathbb{R}^{3\times 3}$ is positive semi-definite, frequency independent, and is a result of the bulk magnetic permeability of the target[1] [23]. We can form a more compact expression of $\boldsymbol{T}(\omega)$ by moving $\boldsymbol{T}_0$ inside the summation and defining a new quantity $g_p(\omega)$ which is the frequency response corresponding to the p-th tensor.

$$\boldsymbol{T}(\omega) = \sum_{p=0}^{P} \boldsymbol{T}_p g_p(\omega) \tag{2.9}$$

where $g_0(\omega) = 1$ and $g_p(\omega) = -\dfrac{j\omega/\zeta_p}{1 + j\omega/\zeta_p}$ for $p \geq 1$. The summation in (2.9) can be

[1]Here it is assumed that the magnetic susceptibility of the target is positive, linear, and frequency independent. This is generally true for practical applications.

substituted into (2.7) to yield

$$r(\omega, \boldsymbol{l}_T, \boldsymbol{l}_R, \boldsymbol{l}_t) = \sum_p g_p(\omega) \underbrace{\boldsymbol{h}_R^T(\boldsymbol{l}_R - \boldsymbol{l}_t)\boldsymbol{T}_p\boldsymbol{h}_T(\boldsymbol{l}_T - \boldsymbol{l}_t)}_{\text{bilinear product}} \tag{2.10}$$

The bilinear product $\boldsymbol{h}_R^T(\boldsymbol{l}_R - \boldsymbol{l}_t)\boldsymbol{T}_p\boldsymbol{h}_T(\boldsymbol{l}_T - \boldsymbol{l}_t)$ can be written as a linear inner product $\boldsymbol{h}^T\boldsymbol{t}_p$ using the following relationship, noting that $t_{ij} = t_{ji}$ [24].

$$\begin{bmatrix} h_{rx} \\ h_{ry} \\ h_{rz} \end{bmatrix}^T \begin{bmatrix} t_{xx} & t_{xy} & t_{xz} \\ t_{yx} & t_{yy} & t_{yz} \\ t_{zx} & t_{zy} & t_{zz} \end{bmatrix} \begin{bmatrix} h_{tx} \\ h_{ty} \\ h_{tz} \end{bmatrix} = \begin{bmatrix} h_{tx}h_{rx} \\ h_{ty}h_{ry} \\ h_{tz}h_{rz} \\ h_{tx}h_{ry} + h_{ty}h_{rx} \\ h_{tx}h_{rz} + h_{tz}h_{rx} \\ h_{ty}h_{rz} + h_{tz}h_{ry} \end{bmatrix}^T \begin{bmatrix} t_{xx} \\ t_{yy} \\ t_{zz} \\ t_{xy} \\ t_{xz} \\ t_{yz} \end{bmatrix} \tag{2.11}$$

This reformulation allows us to write (2.10) as

$$r(\omega, ((\boldsymbol{l}_T, \boldsymbol{l}_R) - \boldsymbol{l}_t)) = \sum_p g_p(\omega)\boldsymbol{h}^T\boldsymbol{t}_p \tag{2.12}$$

where $\boldsymbol{h} = \boldsymbol{h}((\boldsymbol{l}_T, \boldsymbol{l}_R) - \boldsymbol{l}_t) \in \mathbb{R}^{6\times 1}$ is independent of frequency, and depends only on relative positions.

A typical frequency-domain EMI sensor takes measurements at a finite set of M frequencies, so that measurements at one T-R position $(\boldsymbol{l}_{TR})_i = (\boldsymbol{l}_T, \boldsymbol{l}_R)_i$ yield a vector $\boldsymbol{r}_i \in \mathbb{C}^{M\times 1}$. The measurements are also taken at a variety of T-R positions. Assuming N_R receivers for each of N_T transmit locations, the total number of positional measurements is $N = N_R N_T$. All N spatial measurements can be concatenated into the columns of a matrix $\boldsymbol{R}(\boldsymbol{\omega}, \boldsymbol{l}_{TR}) \in \mathbb{C}^{M\times N}$ where the ordering of the columns depends on how the transmit and

receive pairs are enumerated.

$$\boldsymbol{R}(\boldsymbol{\omega}, \boldsymbol{l}_{TR}) = \sum_{p} \boldsymbol{g}_p(\boldsymbol{\omega}) \left[\boldsymbol{H}_s(\boldsymbol{l}_t)\boldsymbol{t}_p\right]^T \tag{2.13}$$

In this expression, $\boldsymbol{g}_p(\boldsymbol{\omega}) = \left[g_p(\omega_1), g_p(\omega_2), \ \ldots, g_p(\omega_M)\right]^T \in \mathbb{C}^{M\times 1}$ is the sampled frequency response associated with the p-th tensor. The magnetic scene matrix $\boldsymbol{H}_s(\boldsymbol{l}_t) \in \mathbb{R}^{N\times 6}$ has rows containing $\boldsymbol{h}^T$ vectors, one for each T-R combination. The subscript s is used to denote that $\boldsymbol{H}_s$ is the magnetic scene for a specific set of measurement positions, and the dependence of that matrix on $\boldsymbol{l}_{TR}$ is implied through s. We also emphasize that for a given measurement frequency, $\boldsymbol{g}_p(\boldsymbol{\omega})$ is the only complex term and also the only frequency-dependent term. The magnetic scene $\boldsymbol{H}_s$ depends only on position and sensor geometry, and the tensors $\boldsymbol{t}_p$ are a function of the target orientation and strength.

The model in (2.13) can also be written in vector form

$$\boldsymbol{r}(\boldsymbol{\omega}, \boldsymbol{l}_{TR}) = \sum_{p} \boldsymbol{H}_s(\boldsymbol{l}_t)\boldsymbol{t}_p \otimes \boldsymbol{g}_p(\boldsymbol{\omega}) \tag{2.14}$$

where $\otimes$ is the Kronecker product. The vector $\boldsymbol{r} \in \mathbb{C}^{MN\times 1}$ can be thought of as a vector where the frequency measurements at each spatial position have been stacked on top of each other. The expressions in (2.13) and (2.14) are the *sum of dipoles* form of the signal model.

2.3.2 Sum of Tensors Form of the Signal Model

We can also express the signal model in what we refer to in this thesis as the sum of tensors (SoT) form of the signal model based on the low-rank model perspective in [25]. This model perspective enables a direct connection between the model and the signal processing used to estimate the target parameters from EMI data [26]. Additionally, this model allows

for a more efficient representation[2] of the target than the the SoD form when the number of relaxation frequencies is larger than the number of *basis* tensors. When the number of relaxations is equal to the number of *basis* tensors, the SoD and SoT forms of the model are equivalent. This is discussed later in this section and shown for some example targets in Section 2.4.

To put the model in the SoT form, we start with the expression in (2.8). We can express $\boldsymbol{T}_p$ as a sum of linearly independent basis tensors $\tilde{\boldsymbol{T}}_k$.

$$\boldsymbol{T}_p = \sum_{k=1}^{K} \alpha_{pk} \tilde{\boldsymbol{T}}_k \tag{2.15}$$

where $K \leq P$ is the number of independent basis tensors required to model the target (we refer to this quantity as the *rank* of the target), and α_{pk} is the amplitude of the p-th relaxation frequency and the k-th basis tensor. The choice of basis and normalization between the amplitudes and basis tensors in (2.15) is arbitrary.[3][4]

We can substitute (2.15) into (2.8) to arrive at

$$\boldsymbol{T}(\omega) = \sum_{k} \alpha_{0k} \tilde{\boldsymbol{T}}_k - \sum_{p} \left(\frac{j\omega/\zeta_p}{1 + j\omega/\zeta_p} \right) \sum_{k} \alpha_{pk} \tilde{\boldsymbol{T}}_k \tag{2.16}$$

We can move the summation over k to the front of the expression and factor out $\tilde{\boldsymbol{T}}_k$ to re-write (2.16)

$$\boldsymbol{T}(\omega) = \sum_{k} \tilde{\boldsymbol{T}}_k \left(\alpha_{0k} - \sum_{p} \alpha_{pk} \left(\frac{j\omega/\zeta_p}{1 + j\omega/\zeta_p} \right) \right) \tag{2.17}$$

[2] By more efficient, we mean that we can model the same target using the same or fewer unknown parameters.

[3] However, it can't be arbitrary in the context of the CRB because all of the parameters need to be identifiable. This is discussed further in the first section of Chapter 4.

[4] We note that when the number of relaxation frequencies is equivalent to the number of basis tensors, each $\boldsymbol{T}_p$ corresponds to a unique $\tilde{\boldsymbol{T}}_k$. Thus, the basis tensors can be made equivalent to the corresponding $\boldsymbol{T}_p$ terms by forcing $\alpha_{pk} = 1$ for all p and k. As such, for targets where $P = K$, the SoT and SoD forms of the model end up being the same.

We define the continuous frequency response of the k-th basis tensor to be

$$f_k(\omega) = \alpha_{0k} - \sum_p \alpha_{pk} \left(\frac{j\omega/\zeta_p}{1 + j\omega/\zeta_p} \right) \tag{2.18}$$

and use (2.18) to re-write $\boldsymbol{T}(\omega)$ as a sum of products of basis tensors and their corresponding frequency responses.

$$\boldsymbol{T}(\omega) = \sum_{k=1}^{K} \tilde{\boldsymbol{T}}_k f_k(\omega) \tag{2.19}$$

We note that $f_k(\omega)$ is related to $g_p(\omega)$ through $f_k(\omega) = \sum_p \alpha_{pk} g_p(\omega)$. This can be seen by substituting (2.15) into (2.9) and re-arranging the summations, as shown below.

$$\begin{aligned}
\boldsymbol{T}(\omega) &= \sum_p g_p(\omega) \boldsymbol{T}_p && \text{(2.20a)} \\
&= \sum_p g_p(\omega) \sum_k \alpha_{pk} \tilde{\boldsymbol{T}}_k && \text{(2.20b)} \\
&= \sum_k \underbrace{\sum_p \alpha_{pk} g_p(\omega)}_{f_k(\omega)} \tilde{\boldsymbol{T}}_k && \text{(2.20c)} \\
&= \sum_k f_k(\omega) \tilde{\boldsymbol{T}}_k && \text{(2.20d)}
\end{aligned}$$

Because (2.19) and (2.9) are similar in form, the procedure to go from (2.10) to (2.13) and (2.14) can be followed for the sum of tensors form of the polarizability tensor. Using this procedure, the SoT form of the signal model is shown in matrix form in (2.21) and in vector form in (2.22).

$$\boldsymbol{R}(\boldsymbol{\omega}, \boldsymbol{l}_{TR}) = \sum_k \boldsymbol{f}_k(\boldsymbol{\omega}) \left[\boldsymbol{H}_s(\boldsymbol{l}_t) \tilde{\boldsymbol{t}}_k \right]^T \tag{2.21}$$

$$\boldsymbol{r}(\boldsymbol{\omega}, \boldsymbol{l}_{TR}) = \sum_k \boldsymbol{H}_s(\boldsymbol{l}_t) \tilde{\boldsymbol{t}}_k \otimes \boldsymbol{f}_k(\boldsymbol{\omega}) \tag{2.22}$$

We note that in these expressions, $\boldsymbol{f}_k(\boldsymbol{\omega}) = \left[f_k(\omega_1), f_k(\omega_2), \ \ldots, f_k(\omega_M) \right]^T \in \mathbb{C}^{M \times 1}$ is the sampled frequency response associated with the k-th basis tensor, and the quantity $\boldsymbol{H}_s(\boldsymbol{l}_t)$

is the same as in (2.13). The form of the expressions in (2.21) and (2.22) highlights how the target response can be thought of as a sum of K co-located rank-one targets, each with a distinct relaxation frequency response.

The matrix and the vector expressions of both forms of the signal model are used in this thesis. The matrix form is used to describe how frequency-domain EMI data is processed, while both vector forms are used in deriving the CRBs.

2.4 Example Targets

In this section, we illustrate the SoD and SoT forms of the signal model for some canonical targets with different symmetries to help develop a better understanding of the different models and their numerous unknown parameters. The chosen target examples also facilitate the discussion of the various target unknowns in the subsequent section, and why each unknown is important for classification.

2.4.1 Wire Loop Target

A loop of conductive, non-magnetic wire is a rank-one, non-magnetic target with a single relaxation frequency.[5] For this example, we assume the axis of the loop is oriented along the z-axis.

SoD Form of the Model

The target is non-magnetic, so $\boldsymbol{t}_0$ and $\boldsymbol{g}_0(\omega)$ are not part of the model. Additionally, because there is one relaxation frequency, $P = 1$, and there is only one tensor $\boldsymbol{t}_1 = [0, 0, \alpha_1, 0, 0, 0]^T$. The frequency response of the tensor is

$$\boldsymbol{g}_1(\omega) = -\frac{j\omega/\zeta_1}{1 + j\omega/\zeta_1} \tag{2.23}$$

[5] A simple idealized model for a loop of wire only has a single relaxation frequency [23]. This is a good model when the diameter of the wire is much smaller than the diameter of the loop. The relaxation frequencies and tensors are more complex when the wire diameter is larger [27].

and the dipole form of the full signal model is

$$\boldsymbol{r}(\omega, \boldsymbol{l}_{TR}) = \boldsymbol{H}_s(\boldsymbol{l}_t)\boldsymbol{t}_1 \otimes \boldsymbol{g}_1(\omega) \tag{2.24}$$

SoT Form of the Model

The target is non-magnetic and rank-one, α_0 is not a part of the model and there is only one basis tensor $\tilde{\boldsymbol{t}}_1 = [0, 0, 1, 0, 0, 0]^T$. The relaxation frequency response (2.18) corresponding to this basis tensor is written as

$$\boldsymbol{f}_1(\omega) = -\alpha_1 \frac{j\omega/\zeta_1}{1 + j\omega/\zeta_1} \tag{2.25}$$

The full signal model for this target is

$$\boldsymbol{r}(\omega, \boldsymbol{l}_{TR}) = \boldsymbol{H}_s(\boldsymbol{l}_t)\tilde{\boldsymbol{t}}_1 \otimes \boldsymbol{f}_1(\omega) \tag{2.26}$$

2.4.2 Two Orthogonal Wire Loops with Different Relaxation Frequencies

The target described in this subsection consists of two non-magnetic co-located loops of wire, with one loop oriented along the x-axis and the other oriented along the z-axis.

SoD Form of the Model

The target is non-magnetic, so $\boldsymbol{t}_0$ and $\boldsymbol{g}_0(\omega)$ are not part of the model. The target has two relaxation frequencies and two tensors. The expressions for the tensors are $\boldsymbol{t}_1 = [\alpha_1, 0, 0, 0, 0, 0]^T$ and $\boldsymbol{t}_2 = [0, 0, \alpha_2, 0, 0, 0]^T$, where $\boldsymbol{t}_1$ describes the strength and orientation of the x-oriented loop and $\boldsymbol{t}_2$ describes the strength and orientation of the z-oriented

loop. The frequency responses of the dipoles are

$$\boldsymbol{g}_1(\boldsymbol{\omega}) = -\frac{j\boldsymbol{\omega}/\zeta_1}{1 + j\boldsymbol{\omega}/\zeta_1} \tag{2.27a}$$

$$\boldsymbol{g}_2(\boldsymbol{\omega}) = -\frac{j\boldsymbol{\omega}/\zeta_2}{1 + j\boldsymbol{\omega}/\zeta_2} \tag{2.27b}$$

The dipole form of the full signal model is

$$\boldsymbol{r}(\boldsymbol{\omega}, \boldsymbol{l}_{TR}) = \sum_{p=1}^{2} \boldsymbol{H}_s(\boldsymbol{l}_t)\boldsymbol{t}_p \otimes \boldsymbol{g}_p(\boldsymbol{\omega}) \tag{2.28}$$

SoT Form of the Model

This target is a rank-two non-magnetic target with 2 relaxation frequencies. The tensors for this target are expressed as $\tilde{\boldsymbol{t}}_1 = [1, 0, 0, 0, 0, 0]^T$ and $\tilde{\boldsymbol{t}}_2 = [0, 0, 1, 0, 0, 0]^T$, where $\tilde{\boldsymbol{t}}_1$ describes the x-oriented loop and $\tilde{\boldsymbol{t}}_2$ describes the z-oriented loop. The relaxation frequency response corresponding to each is

$$\boldsymbol{f}_1(\boldsymbol{\omega}) = -\alpha_{11}\frac{j\boldsymbol{\omega}/\zeta_1}{1 + j\boldsymbol{\omega}/\zeta_1} \tag{2.29a}$$

$$\boldsymbol{f}_2(\boldsymbol{\omega}) = -\alpha_{22}\frac{j\boldsymbol{\omega}/\zeta_2}{1 + j\boldsymbol{\omega}/\zeta_2} \tag{2.29b}$$

The rank form of the full signal model for this target is

$$\boldsymbol{r}(\boldsymbol{\omega}, \boldsymbol{l}_{TR}) = \sum_{k=1}^{2} \boldsymbol{H}_s(\boldsymbol{l}_t)\tilde{\boldsymbol{t}}_k \otimes \boldsymbol{f}_k(\boldsymbol{\omega}) \tag{2.30}$$

2.4.3 Two Co-Axial, Non-Magnetic Wire Loops with Different Relaxation Frequencies

The target described in this subsection consists of two conductive, non-magnetic wire loops oriented along the same axis (the x-axis in this case) with different relaxation frequencies. This target highlights how the SoT form of the signal model can represent targets with

fewer unknowns than the SoD form.

SoD Form of the Model

The target has two distinct relaxation frequencies and two tensors. The tensors are modeled as $\boldsymbol{t}_1 = [\alpha_1, 0, 0, 0, 0, 0]^T$ and $\boldsymbol{t}_2 = [\alpha_2, 0, 0, 0, 0, 0]^T$. The frequency response corresponding to each is

$$\boldsymbol{g}_1(\boldsymbol{\omega}) = -\frac{j\boldsymbol{\omega}/\zeta_1}{1 + j\boldsymbol{\omega}/\zeta_1} \tag{2.31a}$$

$$\boldsymbol{g}_2(\boldsymbol{\omega}) = -\frac{j\boldsymbol{\omega}/\zeta_2}{1 + j\boldsymbol{\omega}/\zeta_2} \tag{2.31b}$$

The dipole form of the full signal model is

$$\boldsymbol{r}(\boldsymbol{\omega}, \boldsymbol{l}_{TR}) = \sum_{p=1}^{2} \boldsymbol{H}_s(\boldsymbol{l}_t)\boldsymbol{t}_p \otimes \boldsymbol{g}_p(\boldsymbol{\omega}) \tag{2.32}$$

SoT Form of the Model

This target is a rank-one target with two relaxation frequencies. The rank of the target can be observed by noting that $\boldsymbol{t}_1$ and $\boldsymbol{t}_2$ are scalar multiples of each other. As such, the basis tensor for this target can be defined as $\tilde{\boldsymbol{t}}_1 = [1, 0, 0, 0, 0, 0]^T$, and the frequency response corresponding to this basis tensor is

$$\boldsymbol{f}_1(\boldsymbol{\omega}) = -\alpha_1 \frac{j\boldsymbol{\omega}/\zeta_1}{1 + j\boldsymbol{\omega}/\zeta_1} - \alpha_2 \frac{j\boldsymbol{\omega}/\zeta_2}{1 + j\boldsymbol{\omega}/\zeta_2} \tag{2.33}$$

The rank form of the full signal model is

$$\boldsymbol{r}(\boldsymbol{\omega}, \boldsymbol{l}_{TR}) = \boldsymbol{H}_s(\boldsymbol{l}_t)\tilde{\boldsymbol{t}}_1 \otimes \boldsymbol{f}_1(\boldsymbol{\omega}) \tag{2.34}$$

2.5 Discussion of Target Parameters

The purpose of this subsection is to discuss the target-dependent parameters which we are interested in estimating. These parameters include the tensors $\boldsymbol{t}_p$, the relaxation frequencies, ζ_p, and the target location $\boldsymbol{l}_t$. From the SoT perspective, we are interested in estimating the basis tensors $\tilde{\boldsymbol{t}}_k$, the relaxation frequencies, ζ_p, their corresponding amplitudes, α_{pk}, and the target location $\boldsymbol{l}_t$.

2.5.1 Target Tensors

The tensors in the dipole form of the signal model contain information about the strength and orientation of the magnetic dipoles used to model the target. Quantities that can be derived from these parameters such as the strength of each dipole, the relative orientation of the dipoles, and the number of independent basis tensors required to model the target are all useful quantities for classification.

To demonstrate the utility of the tensors for classification, we consider the notional problem of distinguishing between the Orthogonal Wire Loops Target in Section 2.4.2 and the Co-Axial Wire Loops Target in Section 2.4.3. If the two targets have the same relaxation frequencies, they differ in only the form of the tensors, which can be used to differentiate them.

The utility of the tensors for classification is complicated by the fact that they are a function of the orientation of the target. The orientation dependence can be illustrated by considering the wire loop target in the Section 2.4.1. If the loop were rotated such that the loop axis was along the x-axis rather than the z-axis, the tensor would be expressed as $\boldsymbol{t}_1 = [\alpha_1, 0, 0, 0, 0, 0]^T$. Because of this dependence on orientation, using the tensors directly for classifying targets may result in classifying the same target at two different rotations as different targets. This issue also motivates the SoT form of the model. When the wire loop target is rotated, the form of the tensor changes, but α_1 remains the same. In the SoT

perspective, α_1 describes the strength of a relaxation frequency, and $\tilde{\boldsymbol{t}}_1$ captures the dipole orientation separately. As such, the α_{pk} terms are candidates for classification as they are independent of orientation. Additionally, the number of basis tensors required to model the target is a candidate for classification as this quantity is independent of orientation as well.

The tensor dependence on rotation is accounted for in the literature by augmenting (2.7) to include rotation matrices around the polarizability tensor [4] [28].

$$r(\omega, \boldsymbol{l}_T, \boldsymbol{l}_R, \boldsymbol{l}_t) = \boldsymbol{h}_R^T(\boldsymbol{l}_R - \boldsymbol{l}_t)\boldsymbol{R}^T(\alpha, \beta, \gamma)\boldsymbol{\Lambda}(\omega)\boldsymbol{R}(\alpha, \beta, \gamma)\boldsymbol{h}_T(\boldsymbol{l}_T - \boldsymbol{l}_t) \tag{2.35}$$

Compared to (2.7), we have made the following substitution $\boldsymbol{T}(\omega) = \boldsymbol{R}^T\boldsymbol{\Lambda}(\omega)\boldsymbol{R}$ in (2.35), where $\boldsymbol{R}$ is a unitary rotation matrix consisting of the following angles: the yaw angle, α, which describes the rotation about the z-axis, the pitch angle, β, which describes the rotation about the y-axis, and the roll angle, γ, which describes the rotation about the x-axis. These rotation axes are shown graphically in Figure 2.1, while the rotation matrix $\boldsymbol{R}$ is mathematically described by the expression in (2.36).

$$\mathbf{R}(\alpha, \beta, \gamma) = \begin{bmatrix} \cos\alpha\cos\beta & \cos\alpha\sin\beta\sin\gamma - \sin\alpha\cos\gamma & \cos\alpha\sin\beta\cos\gamma + \sin\alpha\sin\gamma \\ \sin\alpha\cos\beta & \sin\alpha\sin\beta\sin\gamma + \cos\alpha\cos\gamma & \sin\alpha\sin\beta\cos\gamma - \cos\alpha\sin\gamma \\ -\sin\beta & \cos\beta\sin\gamma & \cos\beta\cos\gamma \end{bmatrix} \tag{2.36}$$

The quantity $\boldsymbol{\Lambda}(\omega)$ is the magnetic polarizability tensor in some reference orientation in the Cartesian coordinate system, and the rotations are defined relative to this reference orientation.

The rotation matrices can be extended from the magnetic polarizability tensor to the basis tensors by combining (2.15) with (2.36) and moving the rotation matrices inside the summation.[6]

$$\boldsymbol{T}(\omega) = \boldsymbol{R}^T\boldsymbol{\Lambda}(\omega)\boldsymbol{R} = \sum_k f_k(\omega)\boldsymbol{R}^T\tilde{\boldsymbol{\Lambda}}_k\boldsymbol{R} \tag{2.37}$$

[6]This can be accomplished in the same manner for the tensors in the sum of dipoles model.

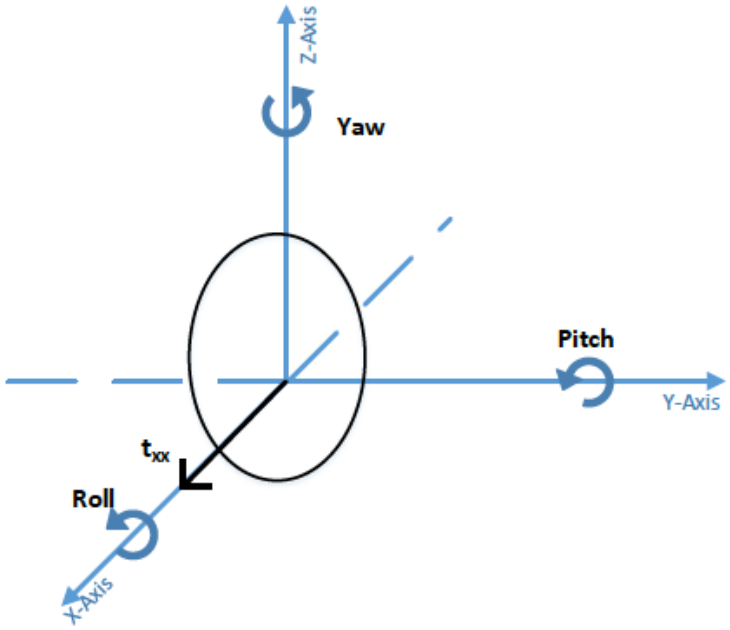

Figure 2.1: Illustration of the target rotation axes corresponding to (2.36). α, β, γ are the yaw, pitch, and roll angles, respectively.

The bilinear form of the rotation matrix in (2.37) can be written in a linear form to accommodate the form of the model in (2.12).

$$\boldsymbol{t}(\omega) = \boldsymbol{Q}\boldsymbol{\lambda}(\omega) = \sum_k f_k(\omega)\boldsymbol{Q}\tilde{\boldsymbol{\lambda}}_k \tag{2.38}$$

where $\boldsymbol{Q}(\alpha, \beta, \gamma)$ is the linear form of the rotation.

An important concept closely related to the rotation matrices is the idea of the *target coordinate system* (TCS). The *target coordinate system* is defined as the three dimensional coordinate system in which the reference orientation of the target results in all of the target's tensors being diagonal, and they are all diagonalized by the same rotation matrix. In other words, the target coordinate system is the coordinate system in which the target's dipoles are aligned with the coordinate axes. We can express an arbitrary rotation of a target in the target coordinate system using (2.39). Many man-made targets (like landmines) can be represented in this form due to their intrinsic symmetry about an XYZ coordinate system.

In fact, for applicable man-made targets, a target whose tensors are diagonal is akin to aligning the Cartesian axes with the target's intrinsic XYZ coordinate system.

$$\boldsymbol{T}_p = \boldsymbol{R}^T \boldsymbol{\Lambda}_p \boldsymbol{R} = \boldsymbol{R}^T \begin{bmatrix} \lambda_1 & 0 & 0 \\ 0 & \lambda_2 & 0 \\ 0 & 0 & \lambda_3 \end{bmatrix} \boldsymbol{R} \tag{2.39}$$

In general, targets are not measured in the target coordinate system and we are interested in calculating the diagonal form of the tensors from the rotated form. We can accomplish this using (2.40).[7]

$$\boldsymbol{\Lambda}_p = \boldsymbol{R} \boldsymbol{T}_p \boldsymbol{R}^T \tag{2.40}$$

where we have made use of the fact that because $\boldsymbol{R}$ is unitary, $\boldsymbol{R}^{-1} = \boldsymbol{R}^T$ and $(\boldsymbol{R}^T)^{-1} = \boldsymbol{R}$.

Without being explicitly stated, the TCS was introduced in Section 2.4. By aligning the various wire loops with the XYZ coordinate axes, we are aligning the TCS with the XYZ coordinate system. In this thesis, we align these two coordinate systems whenever possible as the TCS is a convenient coordinate system for analysis.

2.5.2 Relaxation Frequencies and Amplitudes

In addition to the target tensors, the relaxation frequencies and their corresponding amplitudes (from the SoT perspective) are useful for target classification. This can be illustrated by considering the wire loop target from Section 2.4.1, where one is trying to differentiate between two loops with the same tensor but different relaxation frequencies. While the tensors of these two targets are indistinguishable, the relaxation frequency responses differ in frequency and possibly amplitude, allowing them to be distinguished.

The relaxation frequencies are a function of the target's physical attributes including its geometry and the types of metals that compose it. In the EMI literature, researchers have suggested that the relaxation frequencies (or decay rates in the time-domain) are effective

[7] We relate the linear form of the tensors $\boldsymbol{t}_p$ to the diagonal entries of $\boldsymbol{\Lambda}_p$ in Appendix A.

parameters for classification because they are "intrinsic to the target and are not a function of the target/sensor orientation" [29].

2.5.3 Location

Target location is not directly useful for classification but is necessary for the mitigation of landmines once they are detected and identified. Additionally, this information is useful for fusion/correlation with other systems like ground penetrating radar (GPR) to refine estimates and to potentially mitigate false alarms.

2.6 Georgia Tech Frequency-Domain EMI System

In performing Monte Carlo analysis in this thesis, we typically simulate measurements from the Georgia Tech (GT) frequency-domain EMI system [30] because there is an abundance of laboratory and field data that already exists for this sensor, which allows for an easier translation of this thesis to available data. As such, this section is devoted to describing the system parameters for reference later in the thesis.

The sensor for this system has a single transmit coil and an array of three receive coils. To approximate a handheld EMI sensor, we only use the center receive coil in simulating measurements. The center receive coil and transmit coil are shown in Figure 2.2. This configuration is referred to as a dipole-quadrupole sensor, where the transmit coil is a dipole and the receive coil is a quadrupole. The two disregarded receive coils account for the gaps above and below the center receive coil.

In this thesis, we assume that the sensor is scanned in a grid, where measurements are taken every 0.5 cm in the x-dimension between -50 and $+50$ cm and every 10 cm between -30 and $+30$ cm in the y-dimension. There are 201 measurement positions in x for each of the 7 positions in y yielding 1407 total measurement positions. A visualization of the measurement scan over a notional target located at a depth of 5 cm in the center of the measurement scan is shown in Figure 2.3.

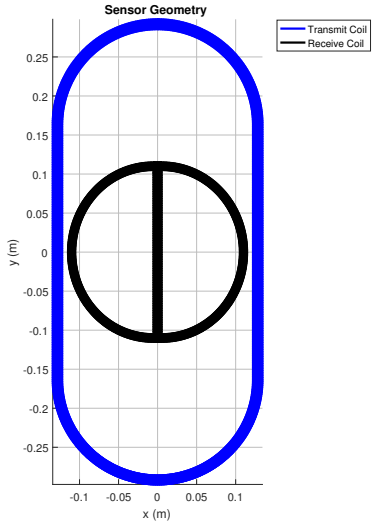

Figure 2.2: Georgia Tech frequency-domain sensor geometry with one transmit coil (outer loop) and one receive coil (inner loop).

At each spatial position, the system takes measurements at 21 discrete frequencies logarithmically spaced between 330 and 90.03 kHz. As such, the measurement matrix for this system is $\boldsymbol{M} \in \mathbb{C}^{21\times1407}$.

In certain sections of this thesis, we generate measurements using the "optimal dipole-quadrupole sensor" from [31] in conjunction with the scan pattern in Figure 2.3. This sensor is shown in Figure 2.4.

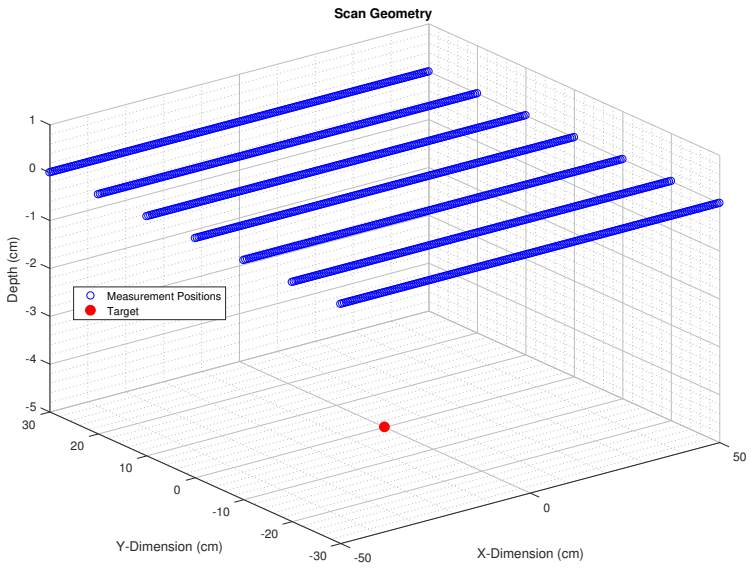

Figure 2.3: Measurement scan positions used with GT frequency-domain EMI system over notional target.

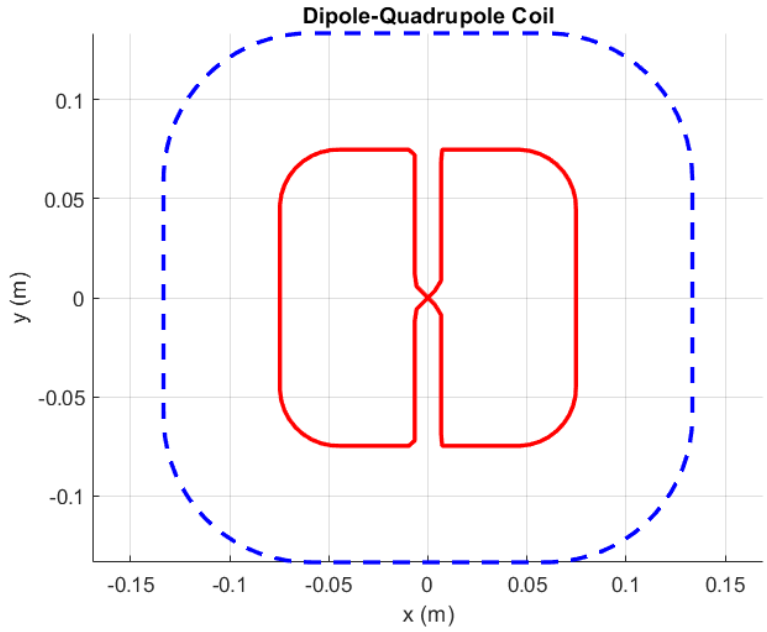

Figure 2.4: An alternative dipole-quadrupole sensor used to simulate measurements in this thesis. Sensor design is from [31]. The dipole transmit coil is shown as the dashed blue line, and the quadrupole receive coil is shown as the solid red line.

CHAPTER 3

CRAMER-RAO LOWER BOUNDS FOR THE SUM OF DIPOLES MODEL

In this chapter, we derive the CRBs for the target tensors $\boldsymbol{t}_p$, their corresponding relaxation frequencies ζ_p, and the target location $\boldsymbol{l}_t$ under the sum of dipoles form of the signal model. These bounds describe parameters that are directly related to the physical signal model, and are completely general in that the derivation is valid for an arbitrary frequency-domain EMI sensor, system, array architecture, frequency measurement scheme, and any target satisfying the sum of dipoles assumption.

For the derivation, we assume that measurements of the target are made in the presence of zero-mean complex white Gaussian noise (CWGN).

3.1 Derivation

We begin the derivation by considering the model for the measurement of a target described by the signal model in (2.14) made in the presence of complex white Gaussian noise (CWGN). The measurement model is

$$\boldsymbol{m}(\boldsymbol{\omega}, \boldsymbol{l}_{TR}) = \underbrace{\sum_{p} \boldsymbol{H}_s(\boldsymbol{l}_t)\boldsymbol{t}_p \otimes \boldsymbol{g}_p(\boldsymbol{\omega})}_{\boldsymbol{r}(\boldsymbol{\theta})} + \boldsymbol{n} \tag{3.1}$$

where $\boldsymbol{n} \sim CN(\boldsymbol{0}, \sigma_n^2 \boldsymbol{I})$, and $\boldsymbol{r}(\boldsymbol{\theta}) \in \mathbb{C}^{MN\times 1}$ is a compact form of the signal model parameterized by the unknowns in $\boldsymbol{\theta} = \left[\boldsymbol{t}_0, \boldsymbol{t}_1, \ \ldots, \boldsymbol{t}_p, \boldsymbol{\zeta}, \boldsymbol{l}_t\right]$ rather than the measurement parameters $\boldsymbol{l}_{TR}$ and $\boldsymbol{\omega}$. The parameters in $\boldsymbol{\theta}$ include P tensors, each of which is $\boldsymbol{t}_p \in \mathbb{R}^{6\times 1}$, the target location $\boldsymbol{l}_t \in \mathbb{R}^{3\times 1}$, and a vector of the relaxation frequencies $\boldsymbol{\zeta} = [\zeta_1, \zeta_2, \ \ldots, \zeta_p]^T \in \mathbb{R}^{P\times 1}$.

The likelihood function of the data is

$$p(\boldsymbol{m};\boldsymbol{\theta}) = \frac{1}{(\pi\sigma_n^2)^{MN}} \cdot \exp\left\{ \frac{1}{\sigma_n^2} \left[\boldsymbol{m} - \boldsymbol{r}(\boldsymbol{\theta})\right]^H \left[\boldsymbol{m} - \boldsymbol{r}(\boldsymbol{\theta})\right] \right\} \tag{3.2}$$

When the likelihood function is of the form in (3.2), the entries for the Fisher Information Matrix (FIM) are well understood to be [20]

$$[\boldsymbol{I}(\boldsymbol{\theta})]_{ij} = \frac{2}{\sigma_n^2} \mathrm{Re}\left\{ \left(\frac{\partial \boldsymbol{r}(\boldsymbol{\theta})}{\partial \theta_i} \right)^H \left(\frac{\partial \boldsymbol{r}(\boldsymbol{\theta})}{\partial \theta_j} \right) \right\} \tag{3.3}$$

As can be seen from (3.3), determining the entries of the FIM amounts to calculating partial derivatives of the signal model with respect to the unknown parameters in $\boldsymbol{\theta}$. The partial of the model with respect to ζ_p is

$$\boldsymbol{d}_{\zeta_p} = \frac{\partial \boldsymbol{r}}{\partial \zeta_p} = \boldsymbol{H}_s(\boldsymbol{l}_t)\boldsymbol{t}_p \otimes \boldsymbol{g}'_{\zeta_p} \tag{3.4}$$

where

$$\boldsymbol{g}'_{\zeta_p} = \frac{\partial \boldsymbol{g}_p(\boldsymbol{\omega})}{\partial \zeta_p} = \frac{j\boldsymbol{\omega}}{(j\boldsymbol{\omega} + \zeta_p)^2} \tag{3.5}$$

The partial of the model with respect to the target's $x-$position is

$$\boldsymbol{d}_{x_t} = \frac{\partial \boldsymbol{r}}{\partial x_t} = \sum_p \boldsymbol{H}'_{s,x}(\boldsymbol{l}_t)\boldsymbol{t}_p \otimes \boldsymbol{g}_p(\boldsymbol{\omega}) \tag{3.6}$$

where $\boldsymbol{H}'_{s,x} \in \mathbb{R}^{N\times 6}$ is the derivative of the magnetic scene matrix with respect to the x-coordinate of the target location. The partials of the model with respect to the target's $y-$position and $z-$position are similar in form:

$$\boldsymbol{d}_{y_t} = \frac{\partial \boldsymbol{r}}{\partial y_t} = \sum_p \boldsymbol{H}'_{s,y}(\boldsymbol{l}_t)\boldsymbol{t}_p \otimes \boldsymbol{g}_p(\boldsymbol{\omega}) \tag{3.7a}$$

$$\boldsymbol{d}_{z_t} = \frac{\partial \boldsymbol{r}}{\partial z_t} = \sum_p \boldsymbol{H}'_{s,z}(\boldsymbol{l}_t)\boldsymbol{t}_p \otimes \boldsymbol{g}_p(\boldsymbol{\omega}) \tag{3.7b}$$

The partial of the model with respect to $\boldsymbol{t}_p$ is

$$\begin{aligned}\boldsymbol{D}_{\boldsymbol{t}_p} = \frac{\partial \boldsymbol{r}}{\partial \boldsymbol{t}_p} &= \left[\frac{\partial \boldsymbol{r}}{\partial t_{xx,p}}, \frac{\partial \boldsymbol{r}}{\partial t_{yy,p}}, \frac{\partial \boldsymbol{r}}{\partial t_{zz,p}}, \frac{\partial \boldsymbol{r}}{\partial t_{xy,p}}, \frac{\partial \boldsymbol{r}}{\partial t_{xz,p}}, \frac{\partial \boldsymbol{r}}{\partial t_{yz,p}}\right] \\ &= \boldsymbol{H}_s(\boldsymbol{l}_t) \otimes \boldsymbol{g}_p(\boldsymbol{\omega})\end{aligned} \tag{3.8}$$

where the columns of $\boldsymbol{D}_{\boldsymbol{t}_p} \in \mathbb{C}^{MN\times 6}$ are the partial derivatives with respect to the 6 components of the p-th tensor. Each column of $\boldsymbol{D}_{\boldsymbol{t}_p}$ is thus $\boldsymbol{d}_{t_{ij,k}} \in \mathbb{C}^{MN\times 1}$. We can group the other model derivatives in a similar fashion according to their associated parameter set. Continuing the notation $\boldsymbol{D}_{[\cdot]}$ to indicate a matrix of partial derivatives of the model with respect to a parameter, we define $\boldsymbol{D}_{\zeta} \in \mathbb{C}^{MN\times P}$ to be

$$\boldsymbol{D}_{\zeta} = \left[\boldsymbol{d}_{\zeta_1}, \boldsymbol{d}_{\zeta_2}, \ \ldots\ , \boldsymbol{d}_{\zeta_p}\right] \tag{3.9}$$

Similarly, we define $\boldsymbol{D}_{\boldsymbol{l}_t} \in \mathbb{C}^{MN\times 3}$, and $\boldsymbol{D}_{\boldsymbol{t}} \in \mathbb{C}^{MN\times 6P}$ to be

$$\boldsymbol{D}_{\boldsymbol{l}_t} = \left[\boldsymbol{d}_{x_t}, \boldsymbol{d}_{y_t}, \boldsymbol{d}_{z_t}\right] \tag{3.10}$$

$$\boldsymbol{D}_{\boldsymbol{t}} = \left[\boldsymbol{D}_{\boldsymbol{t}_0}, \boldsymbol{D}_{\boldsymbol{t}_1}, \ \ldots\ , \boldsymbol{D}_{\boldsymbol{t}_P}\right] \tag{3.11}$$

Note that if the target is non-magnetic, then $\boldsymbol{D}_{\boldsymbol{t}_0}$ is dropped from $\boldsymbol{D}_{\boldsymbol{t}}$. We define $\boldsymbol{J}(\boldsymbol{\theta}) \in \mathbb{R}^{MN\times(7P+3)}$ as

$$\boldsymbol{J}(\boldsymbol{\theta}) = \left[\boldsymbol{D}_{\boldsymbol{\zeta}} \quad \boldsymbol{D}_{\boldsymbol{t}} \quad \boldsymbol{D}_{\boldsymbol{l}_t}\right] \tag{3.12}$$

then the Fisher Information matrix (FIM) $\boldsymbol{I}(\boldsymbol{\theta}) \in \mathbb{R}^{(7P+3)\times(7P+3)}$ for a magnetic target[1] can be written as

$$\boldsymbol{I}(\boldsymbol{\theta}) = \frac{2}{\sigma_n^2} \operatorname{Re}\left\{\boldsymbol{J}^H(\boldsymbol{\theta})\boldsymbol{J}(\boldsymbol{\theta})\right\} \tag{3.13}$$

[1] If the target is non-magnetic, then $\boldsymbol{I}(\boldsymbol{\theta}) \in \mathbb{R}^{(6P+3)\times(6P+3)}$ and $\boldsymbol{J}(\boldsymbol{\theta}) \in \mathbb{R}^{MN\times(6P+3)}$.

In partitioned form, this matrix can be expressed as

$$\boldsymbol{I}(\boldsymbol{\theta}) = \frac{2}{\sigma_n^2}\,\mathrm{Re}\left\{\begin{bmatrix} \boldsymbol{D}_{\boldsymbol{\zeta}}^H \boldsymbol{D}_{\boldsymbol{\zeta}} & \boldsymbol{D}_{\boldsymbol{\zeta}}^H \boldsymbol{D}_{\boldsymbol{t}} & \boldsymbol{D}_{\boldsymbol{\zeta}}^H \boldsymbol{D}_{\boldsymbol{l}_t} \\ \boldsymbol{D}_{\boldsymbol{t}}^H \boldsymbol{D}_{\boldsymbol{\zeta}} & \boldsymbol{D}_{\boldsymbol{t}}^H \boldsymbol{D}_{\boldsymbol{t}} & \boldsymbol{D}_{\boldsymbol{t}}^H \boldsymbol{D}_{\boldsymbol{l}_t} \\ \boldsymbol{D}_{\boldsymbol{l}_t}^H \boldsymbol{D}_{\boldsymbol{\zeta}} & \boldsymbol{D}_{\boldsymbol{l}_t}^H \boldsymbol{D}_{\boldsymbol{t}} & \boldsymbol{D}_{\boldsymbol{l}_t}^H \boldsymbol{D}_{\boldsymbol{l}_t} \end{bmatrix}\right\} \tag{3.14}$$

The CRB matrix $\boldsymbol{C}_{CR}(\boldsymbol{\theta})$, which is a lower bound on the covariance of any unbiased estimator of these parameters, is written as

$$\boldsymbol{C}_{CR}(\boldsymbol{\theta}) = \boldsymbol{I}^{-1}(\boldsymbol{\theta}) = \begin{bmatrix} \boldsymbol{C}_{CR}(\boldsymbol{\zeta}) & \boldsymbol{C}_{CR}(\boldsymbol{\zeta}, \boldsymbol{t}) & \boldsymbol{C}_{CR}(\boldsymbol{\zeta}, \boldsymbol{l}_t) \\ \boldsymbol{C}_{CR}(\boldsymbol{t}, \boldsymbol{\zeta}) & \boldsymbol{C}_{CR}(\boldsymbol{t}) & \boldsymbol{C}_{CR}(\boldsymbol{t}, \boldsymbol{l}_t) \\ \boldsymbol{C}_{CR}(\boldsymbol{l}_t, \boldsymbol{\zeta}) & \boldsymbol{C}_{CR}(\boldsymbol{l}_t, \boldsymbol{t}) & \boldsymbol{C}_{CR}(\boldsymbol{l}_t) \end{bmatrix} \tag{3.15}$$

where the noise variance fraction has been included in the matrix entries. Each $\boldsymbol{C}_{CR}(\cdot)$ matrix is the lower bound on the covariance of any unbiased estimator of the parameter(s) in parentheses. For example, $\boldsymbol{C}_{CR}(\boldsymbol{\zeta})$ is the lower bound on the covariance of any unbiased estimator of the $\boldsymbol{\zeta}$ terms. Similarly, $\boldsymbol{C}_{CR}(\boldsymbol{l}_t, \boldsymbol{\zeta})$ is the lower bound on the covariance of any unbiased estimator of $\boldsymbol{l}_t$ and $\boldsymbol{\zeta}$. Lastly, the matrices along the diagonal in (3.15), $\boldsymbol{C}_{CR}(\boldsymbol{\zeta})$, $\boldsymbol{C}_{CR}(\boldsymbol{t})$, and $\boldsymbol{C}_{CR}(\boldsymbol{l}_t)$, are of interest because their diagonal entries are the CRBs of the unknown parameters.

3.2 Alternate Forms of the Parameters

In Section 2.5.1, we found that the tensors in their form $\boldsymbol{t}_p$ or $\tilde{\boldsymbol{t}}_k$ are dependent on the orientation of the target being measured. For classification, it is desirable to estimate quantities that are invariant to rotation, either directly from the measurement or derived from estimated parameters. One possibility is some measure of the *strength* corresponding to a particular magnetic dipole. As it relates to the tensors, this measure could be the spectral norm, $\|\boldsymbol{T}_p\|_2$, or the Frobenius norm, $\|\boldsymbol{T}_p\|_F$, of each tensor.

In the next two sections, we show how to relate the CRBs of the tensors to the CRBs

of the spectral norm and the Frobenius norm. Again, this is motivated by the desire to use a rotationally-invariant quantity for classification, and naturally one would like to know how well unbiased estimators can estimate these parameters in the variance sense. For notational simplicity, in these sections we index the tensor using integers rather than with their Cartesian components.

$$\boldsymbol{T}_p = \begin{bmatrix} t_{xx} & t_{xy} & t_{xz} \\ t_{xy} & t_{yy} & t_{yz} \\ t_{xz} & t_{yz} & t_{zz} \end{bmatrix} = \begin{bmatrix} t_1 & t_4 & t_6 \\ t_4 & t_2 & t_5 \\ t_6 & t_5 & t_3 \end{bmatrix} \tag{3.16}$$

3.2.1 CRB for the Spectral Norm of a Tensor

We discuss in Section 2.5.1 that for man-made targets, it is possible to diagonalize all of the target tensors using a single rotation matrix $\boldsymbol{R}$. The diagonal form of the p-th tensor, $\boldsymbol{\Lambda}_p$, is related to $\boldsymbol{T}_p$ through

$$\boldsymbol{\Lambda}_p = \begin{bmatrix} \lambda_1 & 0 & 0 \\ 0 & \lambda_2 & 0 \\ 0 & 0 & \lambda_3 \end{bmatrix} = \boldsymbol{R} \begin{bmatrix} t_1 & t_4 & t_6 \\ t_4 & t_2 & t_5 \\ t_6 & t_5 & t_3 \end{bmatrix} \boldsymbol{R}^T \tag{3.17}$$

where $\boldsymbol{R}$ is the rotation matrix that diagonalizes $\boldsymbol{T}_p$ in a way such that $\lambda_1 \geq \lambda_2 \geq \lambda_3$. Because the tensors are symmetric positive semi-definite, the largest eigenvalue of $\boldsymbol{T}_p$ is equal to the largest singular value of $\boldsymbol{T}_p$ which is equal to the spectral norm of $\boldsymbol{T}_p$, $\lambda_1 = \sigma_{\max}(\boldsymbol{T}_p) = \|\boldsymbol{T}_p\|_2$.

It is of interest to calculate the lower bound on an unbiased estimator of $\lambda_1 = \|\boldsymbol{T}_p\|_2$ given an arbitrarily rotated tensor $\boldsymbol{T}_p$, or more generally all of the diagonal terms, λ_1, λ_2, and λ_3. This can be accomplished by first considering the linear form of the tensor rotation[2]

[2]The expression for $\boldsymbol{U}$ is shown in Appendix A.

$$\boldsymbol{\lambda_p} = \boldsymbol{U}\boldsymbol{t}_p \tag{3.18}$$

where $\boldsymbol{\lambda}_p \in \mathbb{R}^{3\times1}$, $\boldsymbol{U} \in \mathbb{R}^{3\ times6}$, and $\boldsymbol{t}_p \in \mathbb{R}^{6\times1}$ are the diagonal entires of the diagonal tensor, the linear form of the rotation, and the linear form of the rotated tensor, respectively. We can calculate the lower bound on the $\boldsymbol{\lambda}_p$ terms by noting that $\text{Var}(\boldsymbol{U}\boldsymbol{t}_p) = \boldsymbol{U}\text{Var}(\boldsymbol{t}_p)\boldsymbol{U}^T$. Thus,

$$\boldsymbol{C}_{CR}(\boldsymbol{\lambda}_p) = \boldsymbol{U}\boldsymbol{C}_{CR}(\boldsymbol{t}_p)\boldsymbol{U}^T \tag{3.19}$$

where the bounds on the diagonal terms of $\boldsymbol{\Lambda}_p$ are the diagonal entries of $\boldsymbol{C}_{CR}(\boldsymbol{\lambda}_p)$, and the bound for the spectral norm of $\boldsymbol{T}_p$ is the first entry in $\boldsymbol{C}_{CR}(\boldsymbol{\lambda}_p)$.

3.2.2 CRB for the Frobenius Norm of a Tensor

The Frobenius norm of the matrix form of the tensor $\boldsymbol{t}_p$ is

$$g(\boldsymbol{t}_p) = \|\boldsymbol{T}_p\|_F = \sqrt{\text{Tr}(\boldsymbol{T}_p^T\boldsymbol{T}_p)} = \sqrt{\sum_{i=1}^{3} t_i^2 + 2\sum_{i=4}^{6} t_i^2} \tag{3.20}$$

The rotational invariance of this norm can be seen by

$$\begin{aligned}
\|\boldsymbol{R}^T\boldsymbol{T}_p\boldsymbol{R}\|_F &= \sqrt{\text{Tr}((\boldsymbol{R}^T\boldsymbol{T}_p\boldsymbol{R})^T(\boldsymbol{R}^T\boldsymbol{T}_p\boldsymbol{R}))} && \text{(3.21a)}\\
&= \sqrt{\text{Tr}(\boldsymbol{R}^T\boldsymbol{T}_p^T\underbrace{\boldsymbol{R}\boldsymbol{R}^T}_{\boldsymbol{I}_{3\times3}}\boldsymbol{T}_p\boldsymbol{R})} && \text{(3.21b)}\\
&= \sqrt{\text{Tr}(\underbrace{\boldsymbol{R}\boldsymbol{R}^T}_{\boldsymbol{I}_{3\times3}}\boldsymbol{T}_p^T\boldsymbol{T}_p)} && \text{(3.21c)}\\
&= \sqrt{\text{Tr}(\boldsymbol{T}_p^T\boldsymbol{T}_p)} && \text{(3.21d)}\\
&= \|\boldsymbol{T}_p\|_F && \text{(3.21e)}
\end{aligned}$$

where (3.21c) results from from the cyclic property of the trace [32]. We define the following scalar functional of the six tensor values $g(\boldsymbol{t}_p) = \|\boldsymbol{T}_p\|_F$. Using the transformation

property of the CRB [20], we can relate the CRB matrix of the tensors, $\boldsymbol{C}_{CR}(\boldsymbol{t}_p)$, to the CRB of the Frobenius norm, $\text{CRB}(\|\boldsymbol{T}_p\|_F)$, as

$$\text{CRB}(\|\boldsymbol{T}_p\|_F) = \left(\frac{\partial g(\boldsymbol{t}_p)}{\partial \boldsymbol{t}_p}\right) \boldsymbol{C}_{CR}(\boldsymbol{t}_p) \left(\frac{\partial g(\boldsymbol{t}_p)}{\partial \boldsymbol{t}_p}\right)^T \tag{3.22}$$

where

$$\frac{\partial g(\boldsymbol{t}_p)}{\partial \boldsymbol{t}_p} = \frac{1}{\|\boldsymbol{T}_p\|_F} \begin{bmatrix} t_1 & t_2 & t_3 & 2t_4 & 2t_5 & 2t_6 \end{bmatrix} \tag{3.23}$$

To summarize, calculating the CRB of the Frobenius norm of tensor $\boldsymbol{T}_p$ involves calculating $\boldsymbol{C}_{CR}(\boldsymbol{t}_p)$ from (3.15), calculating $\frac{\partial g(\boldsymbol{t}_p)}{\partial \boldsymbol{t}_p}$ from (3.23), and computing $\text{CRB}(\|\boldsymbol{T}_p\|_F)$ from (3.22).

3.3 Validation

In this section, we perform Monte Carlo analysis to validate the derived bounds in Section 3.1. We consider two targets: a target consisting of a single dipole and a single relaxation frequency, and a target consisting of three orthogonal loops with three relaxation frequencies. These two targets are chosen for validation to exercise the CRBs for a simple target (the single dipole target) as well as a more complicated target (the three dipole target).

3.3.1 Preliminaries

SNR Definition

For each target model, 200 measurement realizations are generated according to (3.1) at three different target SNRs, denoted SNR_T, and the unknown parameters are estimated using a maximum likelihood estimator for each trial. The sample standard deviation is calculated across all trials for each parameter at each SNR_T. The sample standard deviations for each parameter are shown as blue markers on the subsequent figures. We define SNR_T

as

$$\text{SNR}_T = \frac{\left\| \sum_p \boldsymbol{H}_s(\boldsymbol{l}_t)\boldsymbol{t}_p \otimes \boldsymbol{g}_p(\boldsymbol{\omega}) \right\|^2}{\sigma_n^2} \tag{3.24}$$

Maximum Likelihood Estimator Description

The MLE used for the Monte Carlo analysis takes form in (3.25), where $\boldsymbol{\theta}$ is the same as in (3.1).

$$\min_{\boldsymbol{\theta}} \|\boldsymbol{m} - \boldsymbol{r}(\boldsymbol{\theta})\|_2^2 \tag{3.25}$$

In solving (3.25), we use the MATLAB built-in function *fminsearch*$(\cdot)$ with the default parameters, except for the following: TolFun = $3 \cdot 10^{-3}$, TolX = 10^{-8}, MaxIter = 10^5, MaxFunEvals = 10^5.

Description of Measurement Parameters

We use the same measurement scheme as the Georgia Tech system described in Section 2.6. However, we use the dipole-quadrupole sensor in Figure 2.4 for these simulations. The target is assumed to be located in the center of the grid at a depth of 7.5 cm (i.e., $\boldsymbol{l}_t = (0, 0, 7.5)$ cm).

3.3.2 Single Dipole Target with One Relaxation Frequency

The signal model for the rotated single dipole target considered in this section is

$$\boldsymbol{r}(\boldsymbol{\omega}, \boldsymbol{l}_{TR}) = \boldsymbol{H}_s(\boldsymbol{l}_t)\boldsymbol{t}_1 \otimes \boldsymbol{g}_1(\boldsymbol{\omega}) \tag{3.26}$$

The relaxation frequency response is $\boldsymbol{g}_1(\boldsymbol{\omega}) = -\dfrac{j\boldsymbol{\omega}/\zeta_1}{1 + j\boldsymbol{\omega}/\zeta_1}$. The target in this section has the following vector representation in the TCS: $\boldsymbol{\lambda}_1 = [4, 1, 0, 0, 0, 0]^T$. We rotate this target by 45 degrees in yaw and 45 degrees in pitch so that the resulting tensor is $\boldsymbol{t}_1 = [1.25, 2.50, 1.25, -1.06, -1.06, 1.25]^T$, which is the form of the tensor we consider in this example to exercise the CRBs derived for the Frobenius and spectral norms. There are a

total of 10 unknowns to be estimated: the 6 tensor components, 1 relaxation frequency, and the 3 location coordinates. We use Monte Carlo analysis to validate the bounds for all of the unknown parameters as well as the derived parameters. However, we only show the bounds and Monte Carlo results for the Frobenius and spectral norms for this target. We present figures for the other bounds (position, relaxations, and nonzero tensor components) for the target consisting of three orthogonal wire loops in Section 3.3.3.

The comparisons of the normalized CRBs for the Frobenius and spectral norms to the Monte Carlo results for this target are shown in Figure 3.1. We observe that the two normalized norm bounds are similar for this target, and that for both cases, the Monte Carlo results match the bounds, giving us confidence that the derived bounds are correct.

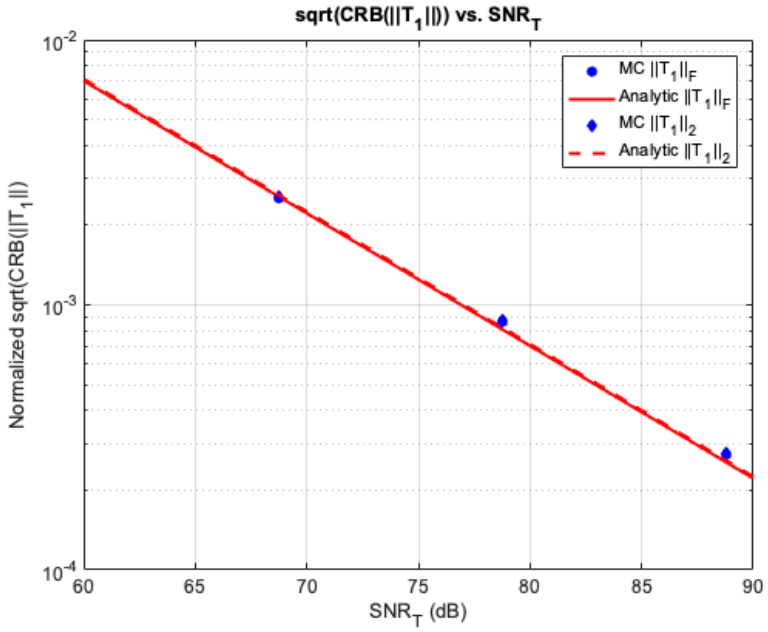

Figure 3.1: Comparison of *normalized* tensor norm bounds and the Monte Carlo results for the single dipole target. The bounds are normalized by the true norm value.

3.3.3 Three Orthogonal Wire Loops Target and Three Relaxation Frequencies

The signal model for the target with three orthogonal loops and three relaxation frequencies considered in this section is

$$\boldsymbol{r}(\boldsymbol{\omega}, \boldsymbol{l}_{TR}) = \sum_{p=1}^{3} \boldsymbol{H}_s(\boldsymbol{l}_t)\boldsymbol{t}_p \otimes \boldsymbol{g}_p(\boldsymbol{\omega}) \tag{3.27}$$

The tensors for this target are $\boldsymbol{t}_1 = [t_1, 0, 0, 0, 0, 0]^T$, $\boldsymbol{t}_2 = [0, 0, t_2, 0, 0, 0]^T$, and $\boldsymbol{t}_3 = [0, t_3, 0, 0, 0, 0]^T$ where $t_1 = t_2 = t_3 = 1$. The target is located at $\boldsymbol{l}_t = (0, 0, 7.5)$ cm. The relaxation frequency response corresponding to each tensor is

$$\boldsymbol{g}_1(\boldsymbol{\omega}) = -\frac{j\boldsymbol{\omega}/\zeta_1}{1 + j\boldsymbol{\omega}/\zeta_1} \tag{3.28a}$$

$$\boldsymbol{g}_2(\boldsymbol{\omega}) = -\frac{j\boldsymbol{\omega}/\zeta_2}{1 + j\boldsymbol{\omega}/\zeta_2} \tag{3.28b}$$

$$\boldsymbol{g}_3(\boldsymbol{\omega}) = -\frac{j\boldsymbol{\omega}/\zeta_3}{1 + j\boldsymbol{\omega}/\zeta_3} \tag{3.28c}$$

where $\zeta_1 = 330$ Hz , $\zeta_2 = 5.451$ kHz, and $\zeta_3 = 90.03$ kHz.

There are a total of 24 unknowns to be estimated: $6 * 3$ tensor components, 3 relaxation frequencies, and the 3 location coordinates. To limit the number of plots, we show the CRBs and the corresponding Monte Carlo results for the relaxation frequencies, the target's location coordinates, and only the nonzero components of the tensors in Figure 3.2, Figure 3.3, and Figure 3.4, respectively. The CRBs of the other parameters not shown also match the Monte Carlo results.

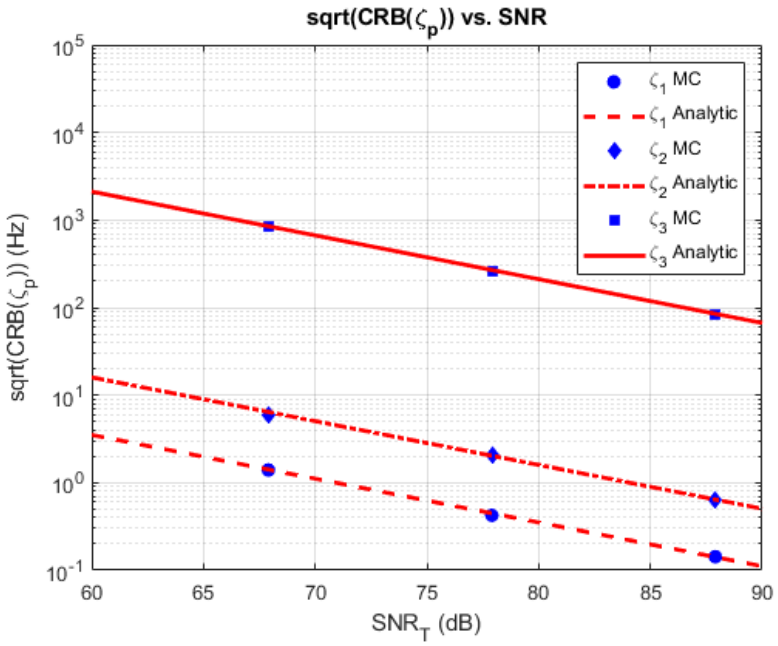

Figure 3.2: Comparison between the CRBs of the relaxation frequencies and the Monte Carlo results for the three orthogonal wire loops target.

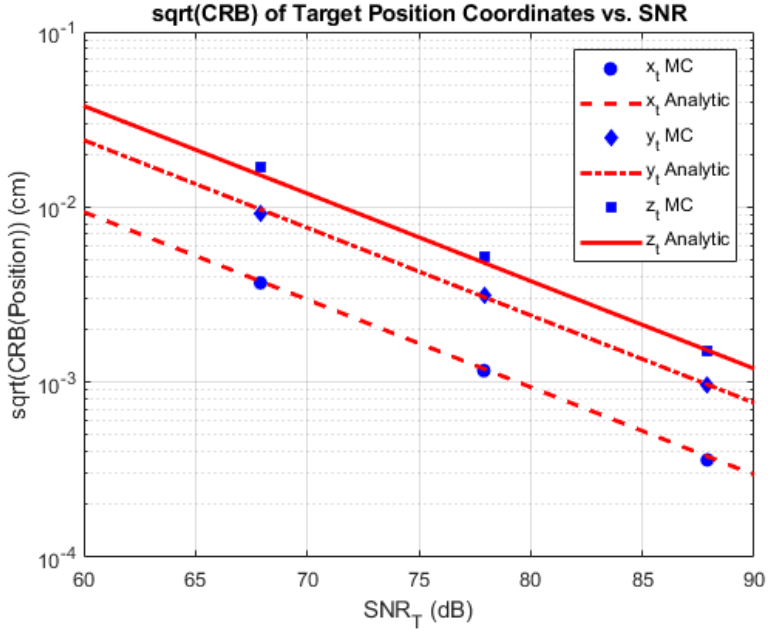

Figure 3.3: Comparison between the CRBs of the target's location coordinates and the Monte Carlo results for the three orthogonal wire loops target.

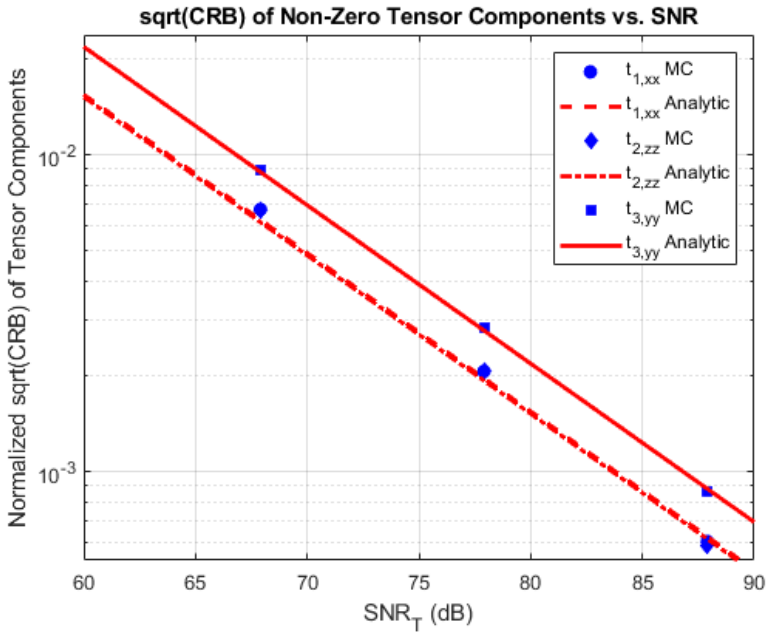

Figure 3.4: Comparison between the CRBs of the nonzero tensor components and the Monte Carlo results for the three orthogonal wire loops target. The Monte Carlo and analytic results for $t_{1,xx}$ and $t_{2,zz}$ are essentially overlaid. Corresponding tensor bounds are normalized by either t_1, t_2, or t_3.

CHAPTER 4

CRAMER-RAO LOWER BOUNDS FOR RANK-ONE TARGETS FOR THE SUM OF TENSORS MODEL

In this chapter, we derive the CRBs for targets that can be represented using a single basis tensor (i.e., rank-one targets) under the sum of tensors (SoT) form of the signal model.[1] As mentioned previously, this form of the model can represent targets using fewer unknowns compared to the sum of dipoles form of the model, and these bounds are directly connected to how the unknown target parameters are estimated in practice [25]. The bounds derived in this section apply to the single-wire loop target in Section 2.4.1 as well as the co-axial loops target in Section 2.4.3, which are just two examples of rank-one targets.

4.1 Model Preliminaries

As mentioned in Section 2.4.1, the choice of basis in the SoT form of the model in (2.15) is arbitrary. However, in order to derive the CRBs, the choice of basis must be defined such that the parameters are identifiable. If the parameters are not identifiable, the Fisher information matrix will be singular and non-invertible. The need for a basis that makes all the parameters identifiable can be illustrated for the signal model of the wire loop target in Section 2.4.1. By examining the relaxation frequency response together with the basis tensor in (2.26), one can see that the α_1 parameter is redundant, as a new parameter $\tilde{\boldsymbol{t}}_{new} = \alpha_1 \cdot \tilde{\boldsymbol{t}}_1$ could equivalently be defined in the SoT model to reduce the number of unknowns by 1.

This motivates the need for a basis that can express $\boldsymbol{T}_p$ using the fewest number of model unknowns possible. In the rank-one case, which we are considering in this chapter, we can do this by embedding one of the α_p terms in $\tilde{\boldsymbol{T}}_1$, and defining the remaining amplitudes

[1] The derivations in this chapter are extended to targets of arbitrary rank in Chapter 8.

relative to it. For this chapter, we choose the embedded amplitude to be the largest such that the remaining $\alpha_p \leq 1$.

To make this basis definition more clear, we apply it to the co-axial loops target in Section 2.4.3 as an example. We define the basis tensor as $\tilde{\boldsymbol{t}}_1 = [\alpha_1, 0, 0, 0, 0, 0]^T$, and thus the relaxation frequency response is

$$\boldsymbol{f}_1(\boldsymbol{\omega}) = -\frac{j\boldsymbol{\omega}/\zeta_1}{1 + j\boldsymbol{\omega}/\zeta_1} - \alpha_2^{'}\frac{j\boldsymbol{\omega}/\zeta_2}{1 + j\boldsymbol{\omega}/\zeta_2} \tag{4.1}$$

where $\alpha_2^{'}$ is related to α_2 in Section 2.4.3 as $\alpha_2^{'} = \alpha_2/\alpha_1$. As can be seen from (4.1), there is only a single unknown amplitude in $\boldsymbol{f}_1(\boldsymbol{\omega})$, as the other has been absorbed into $\tilde{\boldsymbol{t}}_1$. We forgo the prime notation in this section for simplicity, such that it should be implicity understood that the α_p terms are relative quantities.

The choice of embedded amplitude changes the CRBs of $\tilde{\boldsymbol{t}}$ and the other α_p terms, but this is inconsequential, as we are interested in $\boldsymbol{t}_p = \alpha_p\tilde{\boldsymbol{t}}$, whose bounds are unaffected by the choice of the embedded amplitude. This is illustrated in Section 4.6 for an example target.

4.2 Derivation

Under the rank-one target assumption, we can concentrate on a single tensor and drop the k dependence of the signal model. The measurement model, assuming a zero-mean complex white Gaussian noise model, is

$$\boldsymbol{m}(\boldsymbol{\omega}, \boldsymbol{l}_{TR}) = \underbrace{\boldsymbol{H}_s(\boldsymbol{l}_t)\tilde{\boldsymbol{t}} \otimes \boldsymbol{f}(\boldsymbol{\omega})}_{\boldsymbol{r}(\boldsymbol{\theta})} + \boldsymbol{n} \tag{4.2}$$

where $\boldsymbol{n} \sim CN(\boldsymbol{0}, \sigma_n^2\boldsymbol{I})$, and $\boldsymbol{r}(\boldsymbol{\theta}) \in \mathbb{C}^{MN\times 1}$ is a compact form of the signal model parameterized by the unknowns in $\boldsymbol{\theta} = \left[\boldsymbol{\alpha}, \boldsymbol{\zeta}, \tilde{\boldsymbol{t}}, \boldsymbol{l}_t\right]$ rather than the measurement parameters $\boldsymbol{\omega}$ and $\boldsymbol{l}_{TR}$. The unknown parameters that constitute $\boldsymbol{\theta}$ include the relaxation frequency amplitudes

$\boldsymbol{\alpha} = [\alpha_0, \alpha_2, \ldots, \alpha_p]^T \in \mathbb{R}^{P\times 1}$, the relaxation frequencies $\boldsymbol{\zeta} = [\zeta_1, \zeta_2, \ldots, \zeta_p]^T \in \mathbb{R}^{P\times 1}$, the tensor $\tilde{\boldsymbol{t}} \in \mathbb{R}^{6\times 1}$, and the target location $\boldsymbol{l}_t \in \mathbb{R}^{3\times 1}$. We emphasize that we have assumed α_1 is the embedded amplitude, resulting in only P amplitudes to be estimated rather than $P+1$. This assumption does not impact the derivation. In total, there are $2P+9$ unknowns in this model. The likelihood function of the data is

$$p(\boldsymbol{m};\boldsymbol{\theta}) = \frac{1}{(\pi\sigma_n^2)^{MN}} \cdot \exp\left\{ \frac{1}{\sigma_n^2} [\boldsymbol{m} - \boldsymbol{r}(\boldsymbol{\theta})]^H [\boldsymbol{m} - \boldsymbol{r}(\boldsymbol{\theta})] \right\} \tag{4.3}$$

When the likelihood function is in the form of (4.3), the entries for the Fisher Information Matrix (FIM) are well understood to be [20]

$$[\boldsymbol{I}(\boldsymbol{\theta})]_{ij} = \frac{2}{\sigma_n^2} \mathrm{Re}\left\{ \left(\frac{\partial \boldsymbol{r}(\boldsymbol{\theta})}{\partial \theta_i} \right)^H \left(\frac{\partial \boldsymbol{r}(\boldsymbol{\theta})}{\partial \theta_j} \right) \right\} \tag{4.4}$$

The partial of the model with respect to ζ_p is

$$\boldsymbol{d}_{\zeta_p} = \frac{\partial \boldsymbol{r}}{\partial \zeta_p} = \boldsymbol{H}_s(\boldsymbol{l}_t)\tilde{\boldsymbol{t}} \otimes \boldsymbol{f}'_{\zeta_p} \tag{4.5}$$

where

$$\boldsymbol{f}'_{\zeta_p} = \frac{j\boldsymbol{\omega}}{(j\boldsymbol{\omega} + \zeta_p)^2} \alpha_p \tag{4.6}$$

We can concatenate all of the $\boldsymbol{f}'_{\zeta}$ terms into a matrix $\boldsymbol{F}'_{\zeta}$.

$$\boldsymbol{F}'_{\zeta} = \left[\boldsymbol{f}'_{\zeta_1}, \boldsymbol{f}'_{\zeta_2}, \ldots, \boldsymbol{f}'_{\zeta_P} \right] \tag{4.7}$$

The partial of the model with respect to α_p is

$$\boldsymbol{d}_{\alpha_p} = \frac{\partial \boldsymbol{r}}{\partial \alpha_p} = \boldsymbol{H}_s(\boldsymbol{l}_t)\tilde{\boldsymbol{t}} \otimes \boldsymbol{f}'_{\alpha_p} \tag{4.8}$$

where for $p \geq 1$,

$$\boldsymbol{f}'_{\alpha_p} = -\frac{j\boldsymbol{\omega}/\zeta_p}{1 + j\boldsymbol{\omega}/\zeta_p} \tag{4.9}$$

and when $p = 0$,

$$\boldsymbol{f}'_{\alpha_0} = \mathbf{1}_{M\times 1} \tag{4.10}$$

We can concatenate all of the $\boldsymbol{f}'_{\alpha_p}$ terms into a matrix $\boldsymbol{F}'_{\alpha-1}$, where the $\alpha - 1$ subscript indicates that there is no $\boldsymbol{f}'_{\alpha_1}$ term included in this matrix.[2]

$$\boldsymbol{F}'_{\alpha-1} = \left[\boldsymbol{f}'_{\alpha_0}, \boldsymbol{f}'_{\alpha_2}, \ \ldots, \boldsymbol{f}'_{\alpha_P}\right] \tag{4.11}$$

The partial of the model with respect to target's x-position is:

$$\boldsymbol{d}_{x_t} = \frac{\partial \boldsymbol{r}}{\partial x_t} = \boldsymbol{H}'_{s,x}(\boldsymbol{l}_t)\tilde{\boldsymbol{t}} \otimes \boldsymbol{f}(\boldsymbol{\omega}) \tag{4.12}$$

where $\boldsymbol{H}'_{s,x} \in \mathbb{R}^{N\times 6}$ is the derivative of the magnetic scene matrix with respect to the x-coordinate of the target location. The partials of the model with respect to the target's y-position and z-position are similar in form:

$$\boldsymbol{d}_{y_t} = \frac{\partial \boldsymbol{r}}{\partial y_t} = \boldsymbol{H}'_{s,y}(\boldsymbol{l}_t)\tilde{\boldsymbol{t}} \otimes \boldsymbol{f}(\boldsymbol{\omega}) \tag{4.13a}$$

$$\boldsymbol{d}_{z_t} = \frac{\partial \boldsymbol{r}}{\partial z_t} = \boldsymbol{H}'_{s,z}(\boldsymbol{l}_t)\tilde{\boldsymbol{t}} \otimes \boldsymbol{f}(\boldsymbol{\omega}) \tag{4.13b}$$

The partial of the model with respect to $\tilde{\boldsymbol{t}}$ is

$$\begin{aligned} \boldsymbol{D}_{\tilde{\boldsymbol{t}}} = \frac{\partial \boldsymbol{r}}{\partial \tilde{\boldsymbol{t}}} &= \left[\frac{\partial \boldsymbol{r}}{\partial \tilde{t}_{xx}}, \frac{\partial \boldsymbol{r}}{\partial \tilde{t}_{yy}}, \frac{\partial \boldsymbol{r}}{\partial \tilde{t}_{zz}}, \frac{\partial \boldsymbol{r}}{\partial \tilde{t}_{xy}}, \frac{\partial \boldsymbol{r}}{\partial \tilde{t}_{xz}}, \frac{\partial \boldsymbol{r}}{\partial \tilde{t}_{yz}}\right] \\ &= \boldsymbol{H}_s(\boldsymbol{l}_t) \otimes \boldsymbol{f}(\boldsymbol{\omega}) \end{aligned} \tag{4.14}$$

where the columns of $\boldsymbol{D}_{\boldsymbol{t}} \in \mathbb{C}^{MN\times 6}$ are the partial derivatives with respect to the 6 compo-

[2]The derivative of the amplitude term embedded in $\tilde{\boldsymbol{T}}$ is omitted from $\boldsymbol{F}'_{\alpha-1}$. Additionally, if the target is non-magnetic, then $\boldsymbol{f}'_{\alpha_0}$ is not a part of the model and thus omitted from $\boldsymbol{F}'_{\alpha-1}$.

nents of the k-th tensor. Each column of $\boldsymbol{D}_{\tilde{\boldsymbol{t}}}$ is thus $\boldsymbol{d}_{\tilde{t}_{ij}} \in \mathbb{C}^{MN\times 1}$. We can group the other model derivatives in a similar fashion according to their associated parameter set. Continuing the notation $\boldsymbol{D}_{[\cdot]}$ to indicate a matrix of partial derivatives of the model with respect to a parameter, we define $\boldsymbol{D}_{\zeta} \in \mathbb{C}^{MN\times P}$ to be

$$\boldsymbol{D}_{\zeta} = \left[\boldsymbol{d}_{\zeta_1}, \boldsymbol{d}_{\zeta_2}, \ \ldots\ , \boldsymbol{d}_{\zeta_p}\right] = \boldsymbol{H}_s(\boldsymbol{l}_t) \otimes \boldsymbol{F}'_{\zeta} \tag{4.15}$$

Similarly, we define $\boldsymbol{D}_{\alpha} \in \mathbb{C}^{MN\times P}$, and $\boldsymbol{D}_{\boldsymbol{l}_t} \in \mathbb{C}^{MN\times 3}$ to be

$$\boldsymbol{D}_{\alpha} = \left[\boldsymbol{d}_{\alpha_0}, \boldsymbol{d}_{\alpha_2}, \ \ldots\ , \boldsymbol{d}_{\alpha_P}\right] = \boldsymbol{H}_s(\boldsymbol{l}_t) \otimes \boldsymbol{F}'_{\alpha-1} \tag{4.16}$$

and

$$\boldsymbol{D}_{\boldsymbol{l}_t} = \left[\boldsymbol{d}_{x_t}, \boldsymbol{d}_{y_t}, \boldsymbol{d}_{z_t}\right] \tag{4.17}$$

If the $MN \times (2P + 9)$ matrix $\boldsymbol{J}(\boldsymbol{\theta})$ is defined as

$$\boldsymbol{J}(\boldsymbol{\theta}) = \begin{bmatrix}\boldsymbol{D}_{\boldsymbol{\zeta}} & \boldsymbol{D}_{\boldsymbol{\alpha}} & \boldsymbol{D}_{\boldsymbol{t}} & \boldsymbol{D}_{\boldsymbol{l}_t}\end{bmatrix} \tag{4.18}$$

then the FIM can be written as

$$\boldsymbol{I}(\boldsymbol{\theta}) = \frac{2}{\sigma_n^2}\,\mathrm{Re}\left\{\boldsymbol{J}^H(\boldsymbol{\theta})\boldsymbol{J}(\boldsymbol{\theta})\right\} \tag{4.19}$$

In partitioned form, this matrix can be expressed as

$$\boldsymbol{I}(\boldsymbol{\theta}) = \frac{2}{\sigma_n^2}\,\mathrm{Re}\left\{\begin{bmatrix}\boldsymbol{D}_{\boldsymbol{\zeta}}^H\boldsymbol{D}_{\boldsymbol{\zeta}} & \boldsymbol{D}_{\boldsymbol{\zeta}}^H\boldsymbol{D}_{\boldsymbol{\alpha}} & \boldsymbol{D}_{\boldsymbol{\zeta}}^H\boldsymbol{D}_{\boldsymbol{t}} & \boldsymbol{D}_{\boldsymbol{\zeta}}^H\boldsymbol{D}_{\boldsymbol{l}_t} \\ \boldsymbol{D}_{\boldsymbol{\alpha}}^H\boldsymbol{D}_{\boldsymbol{\zeta}} & \boldsymbol{D}_{\boldsymbol{\alpha}}^H\boldsymbol{D}_{\boldsymbol{\alpha}} & \boldsymbol{D}_{\boldsymbol{\alpha}}^H\boldsymbol{D}_{\boldsymbol{t}} & \boldsymbol{D}_{\boldsymbol{\alpha}}^H\boldsymbol{D}_{\boldsymbol{l}_t} \\ \boldsymbol{D}_{\boldsymbol{t}}^H\boldsymbol{D}_{\boldsymbol{\zeta}} & \boldsymbol{D}_{\boldsymbol{t}}^H\boldsymbol{D}_{\boldsymbol{\alpha}} & \boldsymbol{D}_{\boldsymbol{t}}^H\boldsymbol{D}_{\boldsymbol{t}} & \boldsymbol{D}_{\boldsymbol{t}}^H\boldsymbol{D}_{\boldsymbol{l}_t} \\ \boldsymbol{D}_{\boldsymbol{l}_t}^H\boldsymbol{D}_{\boldsymbol{\zeta}} & \boldsymbol{D}_{\boldsymbol{l}_t}^H\boldsymbol{D}_{\boldsymbol{\alpha}} & \boldsymbol{D}_{\boldsymbol{l}_t}^H\boldsymbol{D}_{\boldsymbol{t}} & \boldsymbol{D}_{\boldsymbol{l}_t}^H\boldsymbol{D}_{\boldsymbol{l}_t}\end{bmatrix}\right\} \tag{4.20}$$

The CRB matrix $\boldsymbol{C}_{CR}(\boldsymbol{\theta})$, which is a lower bound on the covariance of any unbiased esti-

mator of these parameters, is the inverse of $\boldsymbol{I}(\boldsymbol{\theta})$ which can be written as

$$\boldsymbol{C}_{CR}(\boldsymbol{\theta}) = \boldsymbol{I}^{-1}(\boldsymbol{\theta}) = \begin{bmatrix} \boldsymbol{C}_{CR}(\boldsymbol{\zeta}) & \boldsymbol{C}_{CR}(\boldsymbol{\zeta},\boldsymbol{\alpha}) & \boldsymbol{C}_{CR}(\boldsymbol{\zeta},\boldsymbol{t}) & \boldsymbol{C}_{CR}(\boldsymbol{\zeta},\boldsymbol{l}_t) \\ \boldsymbol{C}_{CR}(\boldsymbol{\alpha},\boldsymbol{\zeta}) & \boldsymbol{C}_{CR}(\boldsymbol{\alpha}) & \boldsymbol{C}_{CR}(\boldsymbol{\alpha},\boldsymbol{t}) & \boldsymbol{C}_{CR}(\boldsymbol{\alpha},\boldsymbol{l}_t) \\ \boldsymbol{C}_{CR}(\boldsymbol{t},\boldsymbol{\zeta}) & \boldsymbol{C}_{CR}(\boldsymbol{t},\boldsymbol{\alpha}) & \boldsymbol{C}_{CR}(\boldsymbol{t}) & \boldsymbol{C}_{CR}(\boldsymbol{t},\boldsymbol{l}_t) \\ \boldsymbol{C}_{CR}(\boldsymbol{l}_t,\boldsymbol{\zeta}) & \boldsymbol{C}_{CR}(\boldsymbol{l}_t,\boldsymbol{\alpha}) & \boldsymbol{C}_{CR}(\boldsymbol{l}_t,\boldsymbol{t}) & \boldsymbol{C}_{CR}(\boldsymbol{l}_t) \end{bmatrix} \tag{4.21}$$

where the $\sigma_n^2/2$ term has been included in the matrix entries. Each $\boldsymbol{C}_{CR}(\cdot)$ matrix is the lower bound on the covariance of any unbiased estimator of the parameter(s) in parentheses. For example, $\boldsymbol{C}_{CR}(\boldsymbol{\zeta})$ is the lower bound on the covariance of any unbiased estimator of the $\boldsymbol{\zeta}$ terms. Similarly, $\boldsymbol{C}_{CR}(\boldsymbol{\alpha},\boldsymbol{\zeta})$ is the lower bound on the covariance of any unbiased estimator of $\boldsymbol{\alpha}$ and $\boldsymbol{\zeta}$.

The matrices along the diagonal in (4.21), $\boldsymbol{C}_{CR}(\boldsymbol{\zeta})$, $\boldsymbol{C}_{CR}(\boldsymbol{\alpha})$, $\boldsymbol{C}_{CR}(\boldsymbol{t})$, and $\boldsymbol{C}_{CR}(\boldsymbol{l}_t)$ are of interest because their diagonal entries are the CRBs of the unknown parameters. The CRBs in (4.21) are referred to as the SoT CRBs for rank-one targets.

4.3 Summary of Procedure for Calculating the CRBs

The procedure for calculating the CRBs for the unknown parameters associated with the measurement of a rank-one target in complex white Gaussian noise for this SoT model can be summarized as follows:

- Calculate $\boldsymbol{h}_i$ in (2.11) using the Biot-Savart law for all N transmit-receive positions in the measurement.
- Form $\boldsymbol{H}_s(\boldsymbol{l}_t)$ by stacking the N $\boldsymbol{h}_i^T$ vectors.
- Calculate $\boldsymbol{f}(\boldsymbol{\omega})$ using (2.18).
- Calculate $\boldsymbol{F}'_{\zeta}$ by computing (4.6) for each ζ and then concatenate them as in (4.7).

- Calculate $\boldsymbol{F}'_{\alpha-1}$ by computing (4.9) and/or (4.10) for all of the ζ_p parameters depending on the model, and then concatenate them as in (4.11).
- Calculate $\boldsymbol{D}_{\zeta}$ using (4.15), $\boldsymbol{D}_{\alpha}$ using (4.16), and $\boldsymbol{D}_{l_t}$ using (4.17).
- Form the FIM in (4.19) and then compute the inverse to arrive at (4.21).

Issues can arise during the computation of the inverse of the FIM when the relaxation frequency values are much larger than their corresponding amplitudes. This disproportionality can cause the FIM to be ill-conditioned which prevents an accurate inverse from being computed. We find it necessary to normalize the relaxation and measurement frequencies prior to computing and inverting the FIM. After the inverse is computed, we remove the normalization to show the CRBs of the relaxation frequencies in hertz or radians. We find the center frequency of the measurement band to be a convenient normalization factor, though others certainly work just as well.

4.4 Relationship between SoT CRBs and SoD CRBs

In this section, we discuss how to compare the SoT CRBs to the SoD CRBs in Chapter 3.

The relationship between the location unknowns and relaxation frequency unknowns is straightforward as those parameters are the same in both models so they are directly comparable. In the SoT form of the model, however, we split the tensors $\boldsymbol{t}_p$ from the SoD model into relative strength terms (α_{pk}) and basis tensor terms ($\tilde{\boldsymbol{t}}_k$) which represent strength and orientation information. This split is shown in (4.22) in the linear form for the rank-one case.

$$\boldsymbol{t}_p = \alpha_p \tilde{\boldsymbol{t}} \tag{4.22}$$

For the embedded amplitude in the SoT model, there is a straightforward relationship between the basis tensor in the SoT model and the tensor in the SoD model, shown in (4.23).

$$\mathrm{CRB}_{SOT}(\boldsymbol{t}_1) = \mathrm{CRB}(\tilde{\boldsymbol{t}}) \tag{4.23}$$

For the other tensors whose corresponding amplitudes are not embedded in the basis tensor, we can use the parameter transformation property of the CRB to calculate $\boldsymbol{C}_{CR,\mathrm{SoT}}(\boldsymbol{t}_p)$, which is the lower bound on the covariance of $\boldsymbol{t}_p$ based on the SoT model. To use this property, we define the CRB matrix of α_p and the basis tensor $\tilde{\boldsymbol{t}}$ as

$$\boldsymbol{C}_{CR}(\alpha_p;\ \tilde{\boldsymbol{t}}) = \begin{bmatrix} \boldsymbol{C}_{CR}(\alpha_p) & \boldsymbol{C}_{CR}(\alpha_p, \tilde{\boldsymbol{t}}) \\ \boldsymbol{C}_{CR}(\tilde{\boldsymbol{t}}, \alpha_p) & \boldsymbol{C}_{CR}(\tilde{\boldsymbol{t}}) \end{bmatrix} \tag{4.24}$$

where $\boldsymbol{C}_{CR}(\alpha_p)$ is the corresponding diagonal entry in $\boldsymbol{C}_{CR}(\boldsymbol{\alpha})$ from (4.21), $\boldsymbol{C}_{CR}(\tilde{\boldsymbol{t}}, \alpha_p) \in \mathbb{R}^{6\times 1}$ is the column vector in $\boldsymbol{C}_{CR}(\tilde{\boldsymbol{t}}, \boldsymbol{\alpha})$ describing the lower bound on the covariance of $\tilde{\boldsymbol{t}}$ and α_p. $\boldsymbol{C}_{CR}(\tilde{\boldsymbol{t}}) \in \mathbb{R}^{6\times 6}$ is the same as in (4.21), and $\boldsymbol{C}_{CR}(\alpha_p, \tilde{\boldsymbol{t}}) \in \mathbb{R}^{1\times 6}$ is the row vector from the matrix $\boldsymbol{C}_{CR}(\boldsymbol{\alpha}, \tilde{\boldsymbol{t}})$ in (4.21) describing the lower bound on the covariance of α_p and $\tilde{\boldsymbol{t}}$. If we define $\boldsymbol{g}(\boldsymbol{\theta}) = \boldsymbol{g}(\alpha_p, \tilde{\boldsymbol{t}}) = \alpha_p \tilde{\boldsymbol{t}}$, we can write $\boldsymbol{C}_{CR,\mathrm{SoT}}(\boldsymbol{t}_p)$ as a function of $\boldsymbol{C}_{CR}(\alpha_p;\ \tilde{\boldsymbol{t}})$ and $\boldsymbol{g}(\boldsymbol{\theta})$.

$$\boldsymbol{C}_{CR,\mathrm{SoT}}(\boldsymbol{t}_p) = \left(\frac{\partial \boldsymbol{g}(\boldsymbol{\theta})}{\partial \boldsymbol{\theta}}\right) \boldsymbol{C}_{CR}(\alpha_p;\ \tilde{\boldsymbol{t}}) \left(\frac{\partial \boldsymbol{g}(\boldsymbol{\theta})}{\partial \boldsymbol{\theta}}\right)^T \tag{4.25}$$

The matrix $\dfrac{\partial \boldsymbol{g}(\boldsymbol{\theta})}{\partial \boldsymbol{\theta}} \in \mathbb{R}^{6\times 7}$ is the partial of the function $\boldsymbol{g}$ with respect to α_p and $\tilde{\boldsymbol{t}}$. The expression for this quantity is shown in (4.26).

$$\frac{\partial \boldsymbol{g}(\boldsymbol{\theta})}{\partial \boldsymbol{\theta}} = \begin{bmatrix} \dfrac{\partial \boldsymbol{g}(\boldsymbol{\theta})}{\partial \alpha_p} & \dfrac{\partial \boldsymbol{g}(\boldsymbol{\theta})}{\partial \tilde{\boldsymbol{t}}} \end{bmatrix} = \begin{bmatrix} \tilde{\boldsymbol{t}} & \alpha_p \boldsymbol{I}_{6\times 6} \end{bmatrix} \tag{4.26}$$

The diagonal entries of $\boldsymbol{C}_{CR,\mathrm{SoT}}(\boldsymbol{t}_p)$ can be compared with the corresponding diagonal entries of $\boldsymbol{C}_{CR}(\boldsymbol{t}_p)$ from Chapter 3.

4.5 Validation

In this section, we validate the CRB derivation from Section 4.2 by performing Monte Carlo analysis. We consider a wire loop target with one relaxation frequency from Section

2.4.1.

4.5.1 Simulation Description

For the simulation in this section, we use the sensor in Figure 2.4 in conjunction with the scan pattern in Figure 2.3. We assume the same frequency measurement scheme discussed in Section 2.6. We simulate 200 measurements per SNR[3] according to the model in (4.2), and estimate the unknown parameters using the MLE described in (3.25). We compute the sample standard deviation across the Monte Carlo trials for each SNR for comparison with the analytic CRBs. We assume the target is a wire loop aligned with the z-axis and located at $\boldsymbol{l}_t = (0, 0, 7.5)$ cm with a relaxation frequency of 3.18 kHz. The basis tensor is defined as $\tilde{\boldsymbol{t}} = [0, 0, 1, 0, 0, 0]^T$. The FIM for this target is $\boldsymbol{I}(\boldsymbol{\theta}) \in \mathbb{R}^{10\times 10}$.

4.5.2 Simulation Results

We show the results for the Monte Carlo analysis along with the corresponding bounds for the tensor components in Figure 4.1, and the location coordinates and relaxation frequency in Figure 4.2. We observe excellent agreement between the analytic bounds and the Monte Carlo results, giving us confidence that the bounds have been derived correctly.

4.6 Comparison of SoT CRBs to SoD CRBs

In this section, we compare the CRBs under the SoD model to the CRBs under the SoT model for the same coaxial loops target in Section 2.4.3. We are ultimately interested in making two comparisons. The first is comparing the bounds for both models to better understand the relationship between them. The second is verifying that the relationship between the SoT model and SoD model is not impacted by the amplitude we choose to embed in the tensor as is discussed in Section 4.1. As such, we calculate the CRBs for the SoD model as outlined in Chapter 3. Then, we calculate the CRBs for the SoT model for

[3] SNR is defined in this section as $\text{SNR}_T = \|\boldsymbol{H}_s(\boldsymbol{l}_t)\tilde{\boldsymbol{t}} \otimes \boldsymbol{f}(\boldsymbol{\omega})\|_2^2/\sigma_n^2$.

two cases. We embed α_1 in the tensor in the first case, and then embed α_2 in the tensor in the second case.

4.6.1 Simulation Description

The model parameters under the SoT form of the target model for the co-axial loops target is $\alpha_1 = 3, \alpha_2 = 2, \tilde{\boldsymbol{t}} = [1, 0, 0, 0, 0, 0]^T, \zeta_1 = 20$ kHz, $\zeta_2 = 40$ kHz, $\boldsymbol{l}_t = (0, 0, 4)$ cm. In computing the CRBs for the SoT model in the first case where we embed α_1 in the tensor, the amplitudes and resulting tensor are $\alpha_1 = 1$, $\alpha_2 = 2/3$, and $\tilde{\boldsymbol{t}}_1 = [3, 0, 0, 0, 0, 0]^T$. In the second case where we embed α_2 in the tensor, the resulting amplitudes and tensor are $\alpha_1 = 3/2$, $\alpha_2 = 1$, and $\tilde{\boldsymbol{t}}_1 = [2, 0, 0, 0, 0, 0]^T$.

The tensors in the SoD form of the signal model are defined as $\boldsymbol{t}_1 = [3, 0, 0, 0, 0, 0]^T$, $\boldsymbol{t}_2 = [2, 0, 0, 0, 0, 0]^T$.

We compare the CRBs for the different models using the percentage change formula shown in (4.27), using the SoD bounds as the reference bounds for each case of the SoT bounds.

$$\text{Percent Change} = \frac{\text{CRB}_{\text{SoT}}(\cdot) - \text{CRB}_{\text{SoD}}(\cdot)}{\text{CRB}_{\text{SoD}}(\cdot)} \tag{4.27}$$

We compare the location coordinate bounds and relaxation frequency bounds directly, while we relate the tensor bounds for the SoT model to the SoD model using (4.23) for the embedded amplitude and (4.25) for the unknown amplitude.

4.6.2 Simulation Results

The results of the simulation are shown in Figure 4.3. The percent changes under the SoT model when α_1 is the embedded amplitude is shown as the blue circle markers, and are shown as red "x" markers when α_2 is the embedded amplitude. From this figure, we observe that the calculated percent change is the same regardless of whether we use α_1 or α_2 as the embedded amplitude, which we argue is true in Section 4.1. From Figure 4.3a and Figure 4.3d, we observe that the CRBs of the relaxation frequencies and location parame-

ters are essentially the same for the two models, indicated by the fact that percentage change is essentially zero. For the tensors shown in Figure 4.3b and Figure 4.3c, we observe some consistencies as well as some differences. In particular, the percent change corresponding to the non-zero tensor components $t_{1,xx}$ and $t_{2,xx}$ are essentially the same for the two model perspectives. However, for the non-zero components, we observe significant differences, up to 100% change in the value depending on which model is being considered.

For the components that are different, the SoT model bounds have smaller (i.e., better) CRBs compared to the SoD model bounds. We attribute this result to the fact that the SoT model represents the same target with fewer unknown parameters than the SoD model, yielding better CRBs.

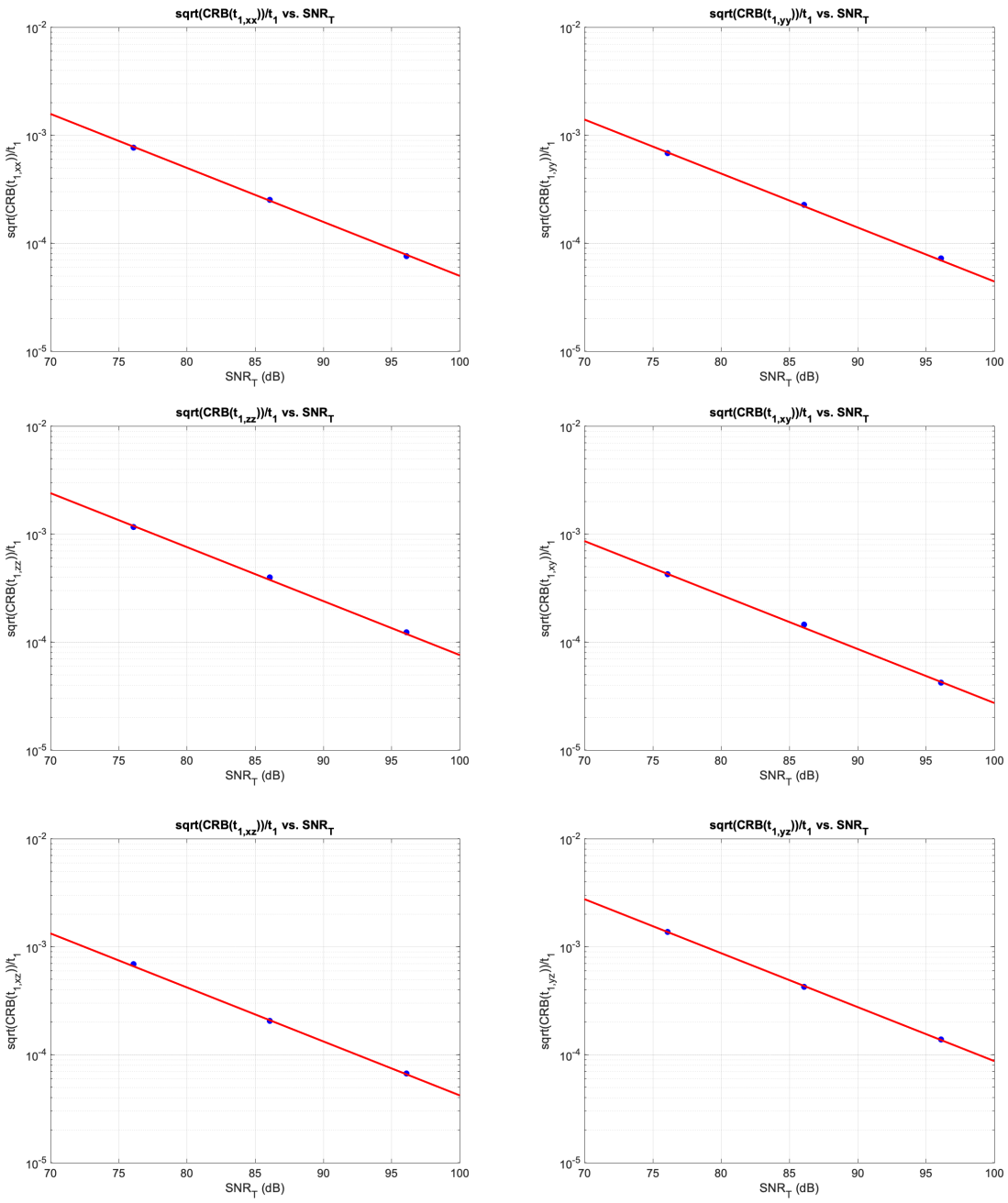

Figure 4.1: $\sqrt{\text{CRB}(\tilde{\boldsymbol{t}}_1)}$ for **Target 1: Rank-One Target with One Relaxation Frequency**: Comparison of Monte Carlo results (circle blue markers) to the analytic CRBs (solid red line) for the six tensor components in $\tilde{\boldsymbol{t}}_1$.

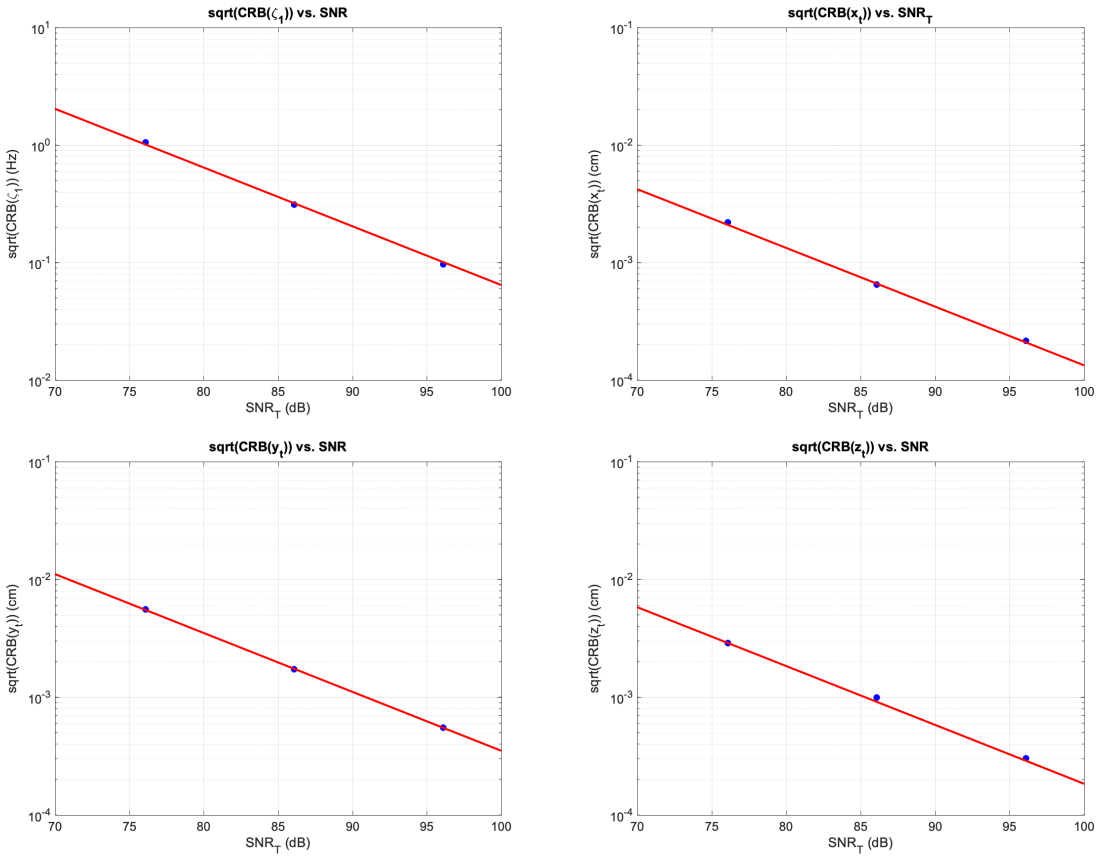

Figure 4.2: $\sqrt{\text{CRB}(\zeta)}$ and $\sqrt{\text{CRB}(\boldsymbol{l}_t)}$ for **Target 1: Rank-One Target with One Relaxation Frequency**: Comparison of Monte Carlo results (blue circle markers) to the analytic CRBs (solid red line). Note the y-axis extent for the unknown relaxation frequency (upper left) is different than the three location unknowns.

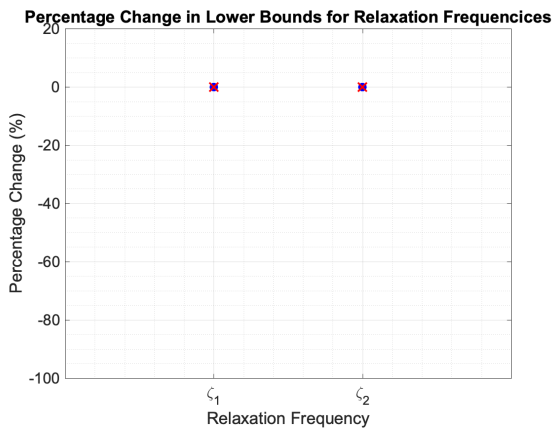

(a) Percentage change for the relaxation frequencies.

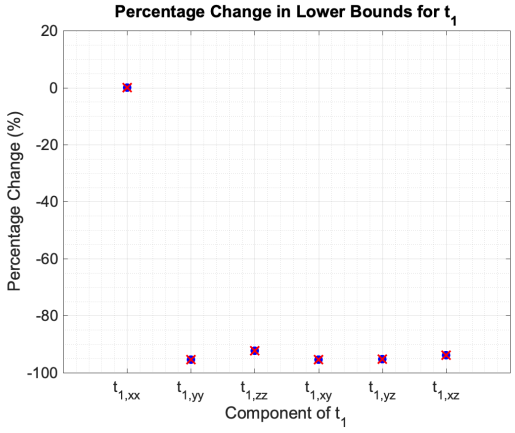

(b) Percentage change for $\boldsymbol{t}_1$.

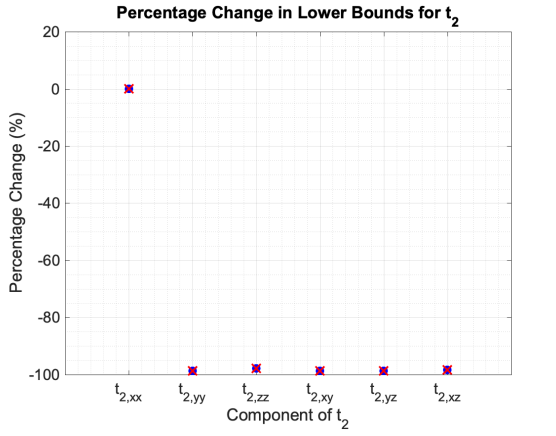

(c) Percentage change for $\boldsymbol{t}_2$.

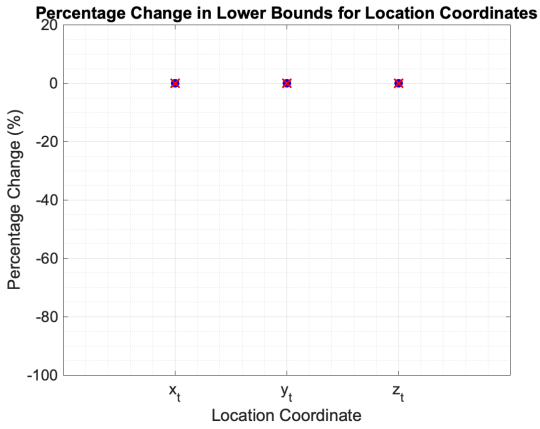

(d) Percentage change for $\boldsymbol{l}_t$.

Figure 4.3: Percentage change between the CRBs derived under the SoT model and the SoD model for a target consisting of two co-axial loops with two relaxation frequencies. Blue circle markers correspond to the SoT model when α_1 is the embedded amplitude, and red "x" markers correspond to SoT model when α_2 is the embedded amplitude. They are overlaid in all sub-figures.

CHAPTER 5
MAXIMUM LIKELIHOOD ESTIMATION AND SIGNAL PROCESSING FOR RANK-ONE TARGETS

In this chapter, we describe a recently published signal processing technique for EMI data that uses the singular value decomposition (SVD) to factor the signal model into separate frequency and spatial components [26]. While the approach presented in [26] does not restrict the number of target tensors, we focus on the application of this processing strategy to rank-one targets (i.e., targets with only a single basis tensor). The relaxation frequencies and a scaled version of their corresponding amplitudes are estimated from the factored frequency model, while the target location and a scaled version of the basis tensor are estimated from the factored spatial model. Splitting the tensor into a basis tensor component and an amplitude component directly reflects the perspective of the SoT form of the signal model and thus the CRBs derived for rank-one targets in Chapter 4.

5.1 Factored Models and Parameter Estimation

This section illustrates how to derive the factored frequency and spatial responses from the measurement matrix in (2.21) for a rank-one target.

5.1.1 Factored Models

The SVD is used to separate the frequency and spatial responses in order to make the parameter estimation problem more tractable. Starting with (2.21), the real and imaginary components of the signal matrix are stacked to form a matrix $\bar{\boldsymbol{R}} \in \mathbb{R}^{2M \times N}$.

$$\bar{\boldsymbol{R}} = \begin{bmatrix} \mathrm{Re}(\boldsymbol{R}) \\ \mathrm{Im}(\boldsymbol{R}) \end{bmatrix} \tag{5.1}$$

For the rank-one case, the measurement matrix (including noise) can be written as

$$\boldsymbol{M} = \bar{\boldsymbol{f}}(\boldsymbol{\omega}) \left[\boldsymbol{H}_s(\boldsymbol{l}_t)\tilde{\boldsymbol{t}}\right]^T + \mathcal{E} \tag{5.2}$$

where

$$\bar{\boldsymbol{f}}(\boldsymbol{\omega}) = \begin{bmatrix} \mathrm{Re}\left(\boldsymbol{f}(\boldsymbol{\omega})\right) \\ \mathrm{Im}\left(\boldsymbol{f}(\boldsymbol{\omega})\right) \end{bmatrix} \tag{5.3}$$

and $\mathcal{E}$ is a matrix of zero-mean i.i.d. Gaussian noise with variance $\sigma_n^2/2$. The SVD of the measurement matrix is the product of three matrices, which can also be written as a sum of outer products as

$$\boldsymbol{M} = \boldsymbol{U}\boldsymbol{\Sigma}\boldsymbol{V}^T = \sum_{i=1}^{2M} \sigma_i \boldsymbol{u}_i \boldsymbol{v}_i^T \tag{5.4}$$

where we assume $K < 2M < N$, where K is the number of independent tensors required to model the target and assumed to be one in this chapter. The outer product terms involve the singular values σ_i and the left and right singular vectors, $\boldsymbol{u}_i$ and $\boldsymbol{v}_i$, respectively. Each outer product is a rank-one matrix which is important when getting the best low-rank approximation to $\boldsymbol{M}$ by taking the terms with the largest singular values [33]. When the target is rank-one, only the first singular value and vectors are kept yielding

$$\boldsymbol{M} \approx \sigma \boldsymbol{u}_1 \boldsymbol{v}_1^T = \bar{\boldsymbol{f}}(\boldsymbol{\omega}) \left[\boldsymbol{H}_s(\boldsymbol{l}_t)\tilde{\boldsymbol{t}}\right]^T + E \tag{5.5}$$

where E is a noise term. By comparing the left and right sides of (5.5), we see that $\boldsymbol{u}_1$ contains the frequency information about the target, while $\boldsymbol{v}_1$ contains the spatial information. When the signal-to-noise ratio is high, implying that the signal singular value is well-separated from the first noise singular value [34], a good first-order approximation to $\sigma_1 \boldsymbol{u}_1$ is

$$\sigma_1 \boldsymbol{u}_1 = c\bar{\boldsymbol{f}}(\boldsymbol{\omega}) + \boldsymbol{n}_u \tag{5.6}$$

where $c \approx \|\boldsymbol{H}_s(\boldsymbol{l}_t)\boldsymbol{t}\|$ and the noise distribution is well described by $\boldsymbol{n}_u \sim N\left(\boldsymbol{0}, \frac{\sigma_n^2}{2}\boldsymbol{I}\right)$. Similarly, a good first-order approximation for $\sigma_1 \boldsymbol{v}_1$ is

$$\sigma_1 \boldsymbol{v}_1 = \boldsymbol{H}_s(\boldsymbol{l}_t)\boldsymbol{t}_f + \boldsymbol{n}_v \tag{5.7}$$

where $\boldsymbol{t}_f \approx \|\boldsymbol{f}(\boldsymbol{\omega})\|\tilde{\boldsymbol{t}}$ and $\boldsymbol{n}_v \sim N\left(\boldsymbol{0}, \frac{\sigma_n^2}{2}\boldsymbol{I}\right)$. The expressions in (5.6) and (5.7) are the factored frequency model and factored spatial model, respectively.

5.1.2 Parameter Estimation for Factored Frequency Model

We can recombine the real and imaginary parts of the left singular vector $\boldsymbol{u}_1$ to expand the model in (5.6) as

$$\begin{aligned} \boldsymbol{y} &= \sigma_1 \left[\boldsymbol{u}_1(1:M) + j\boldsymbol{u}_1(M+1:2M)\right] \\ &= a_0 - \sum_p a_p \frac{j\boldsymbol{\omega}/\zeta_p}{1 + j\boldsymbol{\omega}/\zeta_p} + \boldsymbol{n}_y \end{aligned} \tag{5.8}$$

where $\boldsymbol{y} \in \mathbb{C}^{M\times 1}$, $\boldsymbol{n}_y \sim CN\left(\boldsymbol{0}, \sigma_n^2\boldsymbol{I}\right)$, and $j = \sqrt{-1}$. The a_p parameters in (5.8) are related to the α_p terms in (2.18) through $a_p \approx c\alpha_p$. The approximation comes from the fact that the true value of c includes a bias term due to the noise perturbation of the first singular value. The expected value of the bias is approximately equal to zero when the SNR is sufficiently high [34].

While an unbiased estimator may not be feasible for this model because the number of relaxation frequencies is unknown and is difficult to estimate, we use this type of estimator to establish how close the variance of these estimates are to the CRBs derived in Chapter 3 and Chapter 4.

The maximum likelihood estimator (MLE) for the model in (5.6) is written mathemat-

ically as[1]

$$\min_{\boldsymbol{a},\boldsymbol{\zeta}} \|\boldsymbol{y} - \boldsymbol{f}(\boldsymbol{\zeta}, \boldsymbol{a})\|_2^2 \tag{5.9}$$

where $\boldsymbol{\zeta} = [\zeta_1, \zeta_2, \ldots, \zeta_p]^T$ and $\boldsymbol{a} = [a_0, a_1, \ldots, a_p]^T$. In solving this equation for the results shown in this chapter, we use the MATLAB built-in function fminsearch(·) which uses the Nelder-Mead simplex search method.[2] Additionally, we initialize the minimization function with the correct model parameters to avoid converging to a local minimum.

5.1.3 Parameter Estimation for Factored Spatial Model

The MLE for the factored spatial model in (5.7) is written as

$$\min_{\boldsymbol{l}_t,\boldsymbol{t}_f} \left\|\sigma_1 \boldsymbol{v}_1 - \boldsymbol{H}_s(\boldsymbol{l}_t)\boldsymbol{t}_f\right\|_2^2 \tag{5.10}$$

The minimization expression in (5.10) is a separable linear least-squares problem that can be solved in various ways [35]. For this thesis, we choose a gradient descent method where we estimate the linear parameters $\boldsymbol{t}_f$ first and then compute the gradient of the cost function with respect to $\boldsymbol{l}_t$. We then step in the negative gradient direction by an amount α and repeat the process until one of our stop conditions is met.[3] Details are shown in Algorithm 1. The MATLAB built-in function fminsearch(·) could also be used.

An alternative procedure for solving (5.10) is to evaluate the minimization function over a grid of potential solutions and choosing the grid point that minimizes the function as the solution. The grid search is computationally costly and therefore time consuming because a $\boldsymbol{H}_s(\boldsymbol{l}_t)$ matrix must be generated for each candidate location. This is exacerbated by the fact that the grid spacing must be very fine in order to eliminate estimator bias that can result from a grid that is discretized too coarsely. As such, in choosing the technique

[1] $\boldsymbol{f}(\boldsymbol{\zeta}, \boldsymbol{a})$ is equivalent to $c\boldsymbol{f}(\boldsymbol{\omega})$. The former is used here to make the dependence on $\boldsymbol{\zeta}$ and $\boldsymbol{a}$ explicit in the minimization expression.

[2] The default settings are used except for the following: MaxIter = 1e6, MaxFunEvals = 1e6, TolX = 1e-12, TolFun = 1e-12.

[3] For Monte Carlo results shown later in this thesis, our stop conditions are $g_{\min} \leq 10^{-5}$, $dl_{t,\min} \leq 10^{-4}$, $N_{\max} = 100$.

described by Algorithm 1, we mitigate the potential for convergence issues by initializing the algorithm with the true target location, which all but guarantees that the first minimum found will be the correct solution.

Algorithm 1 Location and Tensor Estimation Algorithm

Require: Target tensor and location estimation from measurement $\boldsymbol{m}$
Input: Functional dictionary $\boldsymbol{H_s(l_t)} \in \mathbb{R}^{N_{ls} \times 6}$, measurement vector $\boldsymbol{m} \in \mathbb{R}^{N_{ls} \times 1}$, step size α, and stopping conditions $g_{\min}$, $dl_{t,\min}$, $N_{\max}$
Output: Estimated target location $\boldsymbol{l}_t$ and tensor amplitudes $\boldsymbol{t}_f$
  Initialization $\boldsymbol{l_t} = \boldsymbol{l_t^{(0)}}$, $i = 1$
  while $i < N_{\max}$, $g \geq g_{\min}$, $dx \geq dx_{\min}$ **do**
    $\boldsymbol{H}_s = \boldsymbol{H}_s(\boldsymbol{l}_t)$
    $\boldsymbol{t}_f = \boldsymbol{H}_s^{\dagger} \boldsymbol{m}$
    $\boldsymbol{g} = \nabla \left\| \boldsymbol{y} - \boldsymbol{H}_s(\boldsymbol{l}_t)\boldsymbol{t}_f \right\|$
    $\boldsymbol{l}_{t,\text{new}} = \boldsymbol{l_t} - \alpha \boldsymbol{g}$
    $g = \|\boldsymbol{g}\|$
    $dl_t = \|\boldsymbol{l}_{t,\text{new}} - \boldsymbol{l_t}\|$
    $\boldsymbol{l_t} = \boldsymbol{l}_{t,\text{new}}$
    $i = i + 1$
  end while

5.1.4 Tensor Estimation

We can use the estimates of the a_p terms from the factored frequency model along with the estimate of $\boldsymbol{t}_f$ from the factored spatial model to form an estimate of the tensors $\boldsymbol{t}_p$. This can be done by noting that $\|\boldsymbol{H}_s(\boldsymbol{l}_t)\|\|\boldsymbol{f}(\boldsymbol{\omega})\|\boldsymbol{t}_p = a_p \boldsymbol{t}_f$, so that if we scale the quantity on the right-hand side like in (5.11), we can form an unbiased estimate of $\boldsymbol{t}_p$.

$$\hat{\boldsymbol{t}}_p = \frac{1}{\sigma_1} \hat{a}_p \hat{\boldsymbol{t}} \tag{5.11}$$

5.2 Factored Model MLE Performance vs. CRBs

In this section, we use Monte Carlo (MC) analysis to compare the variances of the MLEs in (5.9) to the CRBs in (4.21) for three different target models: a non-magnetic target with one relaxation frequency, a magnetic target with one relaxation frequency, and a magnetic

target with two relaxation frequencies. Through these target models, we not only see how close the MLE performance is to the CRBs, but also explore the behavior of the CRBs as a function of signal-to-noise ratio (SNR) and relaxation frequency.

5.2.1 Preliminaries

Frequency-Domain EMI System Description

For the Monte Carlo analysis, we simulate measurements using the Georgia Tech system and measurement parameters in Section 2.6.

Target Description

The assumed target for all of the simulations is a z-directed dipole target located in the center of measurement grid. The basis tensor for this target is $\tilde{\boldsymbol{t}} = [0, 0, 1, 0, 0, 0]^T$. The target is located at $\boldsymbol{l}_t = (0, 0, 7.5)$ cm.

Defining SNR

We show the CRBs for a particular relaxation frequency and amplitude as a function of the SNR of that particular relaxation frequency. We define the energy of a particular relaxation frequency as

$$E_{\zeta_p} = \|\boldsymbol{H}_s(\boldsymbol{l}_t)\tilde{\boldsymbol{t}}\|^2 \|\alpha_p \frac{j\boldsymbol{\omega}/\zeta_p}{1 + j\boldsymbol{\omega}/\zeta_p}\|^2 \tag{5.12}$$

and $\text{SNR}_{\zeta_p} = E_{\zeta_p}/\sigma_n^2$. Similarly, we can define SNR_{ζ_p} as it relates to the quantities in (5.8) as

$$\text{SNR}_{\zeta_p} = \|a_p \frac{j\boldsymbol{\omega}/\zeta_p}{1 + j\boldsymbol{\omega}/\zeta_p}\|^2/\sigma_n^2 \tag{5.13}$$

The near equivalence of (5.12) and (5.13) can be seen by substituting $a_p \approx \alpha_p \|\boldsymbol{H}_s \boldsymbol{t}\|$ into (5.13).

Description of Monte Carlo Trials

For the MC trials, 500 independent measurement realizations are generated according to (4.2) at each SNR or relaxation frequency, depending on the variable parameter in the example. For each MC trial, the measurement is factored using the SVD as previously described[4] and the MLE in (5.9) is used to estimate the unknown parameters in the assumed model. The sample standard deviations are calculated across all trials for all unknown parameters for a given relaxation frequency or SNR and plotted as markers on the corresponding figures.

5.2.2 Example 1: Target with a Single Relaxation Frequency

For this example, we consider a magnetic target where $\alpha_0 = 1$ and a non-magnetic target where $\alpha_0 = 0$, assuming each has a single relaxation frequency. For each target, we calculate $\text{CRB}(\zeta)$ as a function of ζ over a slightly larger range than the measurement frequency band $[\omega_1, \omega_{21}]$ indicated by the vertical black lines in Figure 5.1. As we sweep the relaxation frequency, both α_0 and α_1 remain fixed. $\sigma_n^2 = 10^{-2}$ also remains fixed. The intent is to compare targets of equal amplitude but varying relaxation frequency. With these quantities fixed, SNR_{ζ_p} as defined decreases from 52 dB to 41 dB across the measurement band as the relaxation frequency increases because $\|\boldsymbol{f}(\boldsymbol{\omega})\|$ decreases.

The CRB for the relaxation frequency for both target types is shown in the top half of Figure 5.1 along with the MC results. We observe excellent agreement between the MC results and the analytic bounds for both targets. This suggests that essentially no information is lost about the relaxation frequency by factoring the model using the SVD, suggesting that the SVD is a viable pre-processing step from an estimation perspective for the relaxation frequencies.

For both target models, the CRB increases as ζ increases due to the fact that the actual value of ζ is increasing and because the SNR is decreasing. The 1σ value across the

[4] Since $(-U)\Sigma(-V)^T = U\Sigma V^T$, we ensure the sign after the SVD is consistent across Monte Carlo trials.

measurement band varies between 3 rad and 1 krad, with best performance at the lower end of the measurement band.

Comparing the two target models, we observe that the presence of α_0 has a greater effect on the lower frequencies than the higher frequencies, which intuitively makes sense as a DC term would be more correlated with lower frequencies. However, the overall impact of the α_0 term in the model is not significant inside the measurement band.

An alternative representation for plotting this bound is to plot the CRB for $\log_{10}(\zeta)$, which is more akin to how the spectrum error is computed in [36]. Using the transformation of variables property [20], this bound is written as

$$\sqrt{\text{CRB}(\log_{10}(\zeta))} = \frac{1}{\ln(10)} \cdot \frac{\sqrt{\text{CRB}(\zeta)}}{\zeta} \approx \frac{\sqrt{\text{CRB}(\zeta)}}{2.3\zeta} \tag{5.14}$$

We show the bound in this form in the bottom half of Figure 5.1. As shown in (5.14), this transformation effectively normalizes the CRB by ζ. As a result, we observe a flatter response across the measurement band which suggests that the increasing value of ζ is primarily responsible for the CRB trends one can observe in the top part of Figure 5.1. It is also worth noting in the bottom half of Figure 5.1 that the 10 dB decrease in SNR as relaxation frequency increases *does not* manifest as an order of magnitude difference in the CRB between the lower and upper ends of the measurement band.

5.2.3 Example 2: Magnetic Target with Two Relaxation Frequencies

As another example, we consider a magnetic rank-one target with two relaxation frequencies, $\zeta_1 = 90$ krad and $\zeta_2 = 20$ krad. We set $\alpha_2 = 0.7559$ so that the energy in each relaxation frequency is the same (i.e. $E_{\zeta_1} = E_{\zeta_2}$). Additionally, we set $\alpha_0 = 0.5$. We show the CRBs for the relaxation frequencies along with the Monte Carlo results in Figure 5.2. We observe that the CRBs for the relaxation frequencies have excellent agreement with the Monte Carlo results. Additionally, we show the CRBs for α_0 and α_2 along with the Monte

Carlo results in Figure 5.3. To generate the Monte Carlo results for this figure, we estimate $\hat{\alpha}_p = \hat{a}_p/\hat{a}_1$ for each trial and calculate the sample standard deviation of $\hat{\alpha}_p$ across all trials for each SNR.[5] We also observe that the α_p terms are nearly normally distributed. This is due to the invariance property of the MLE [20].

5.2.4 Example 3: Co-Axial Loops Target with Two Relaxation Frequencies

The target model is the co-axial loops target in Section 2.4.3, where for the model parameters we assume $\alpha_1 = 1, \alpha_2 = 0.5, \tilde{\boldsymbol{t}} = [0, 0, 4, 0, 0, 0]^T, \zeta_1 = 20$ kHz, $\zeta_2 = 40$ kHz, $\boldsymbol{l}_t = (-1, 2, 6)$ cm. We simulate 200 measurements according to (4.2) at each of three different SNR[6] values, use the SVD to factor the measurement into the frequency and spatial responses for each measurement, and then estimate the unknown parameters in the factored models using the MLEs in (5.9) and (5.10). We compute the CRBs of the tensors using the SoD model as well as the SoT model, and compare the sample standard deviation from the Monte Carlo trials for these estimates to these bounds. We show the results for $\boldsymbol{t}_1$, $\boldsymbol{t}_2$, $\boldsymbol{l}_t$, and $\boldsymbol{\zeta}$ in Figure 5.4, Figure 5.5, Figure 5.6, and Figure 5.7.

From the figures, we observe the following interesting result: the Monte Carlo results match the CRBs derived under the SoT model for all of the unknown parameters. This result is interesting because it suggests that no information is lost about the unknown parameters by factoring the model into its spatial and frequency components, which bodes well for the model recovery method presented in [25].

[5] Recall that based on the model definition, $(a_1) \approx \|\boldsymbol{H}_s(\boldsymbol{l}_t)\tilde{\boldsymbol{t}}\|\alpha_1$.
[6] SNR is defined in this section as $\text{SNR}_T = \|\boldsymbol{H}_s(\boldsymbol{l}_t)\tilde{\boldsymbol{t}} \otimes \boldsymbol{f}(\boldsymbol{\omega})\|_2^2/\sigma_n^2$.

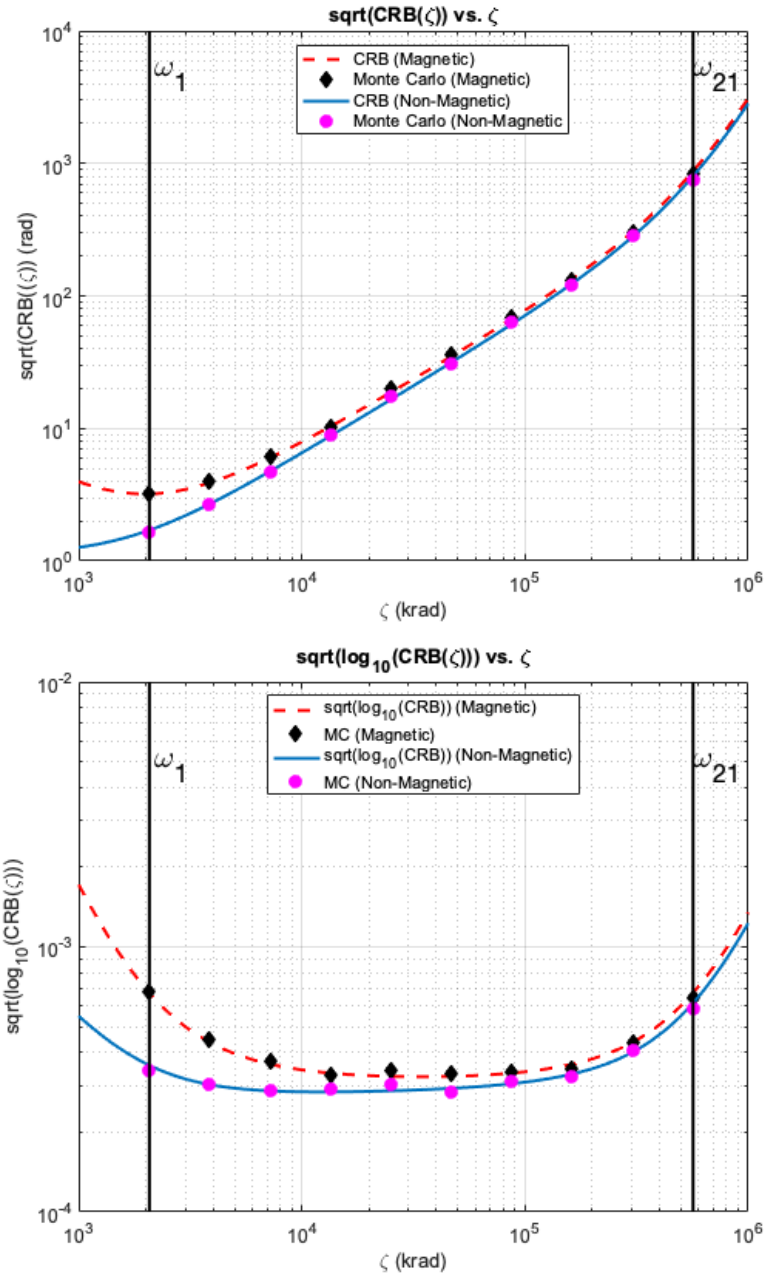

Figure 5.1: Analytic $\sqrt{\mathrm{CRB}(\zeta)}$ (top) and $\sqrt{\mathrm{CRB}(\log_{10}(\zeta))}$ (bottom) for a magnetic (dashed line) and non-magnetic (solid line) rank one target with a single relaxation frequency shown along with Monte Carlo results for the magnetic target (diamond marker) and the non-magnetic target (circle marker). Excellent agreement between the Monte Carlo results and the analytic curves is observed.

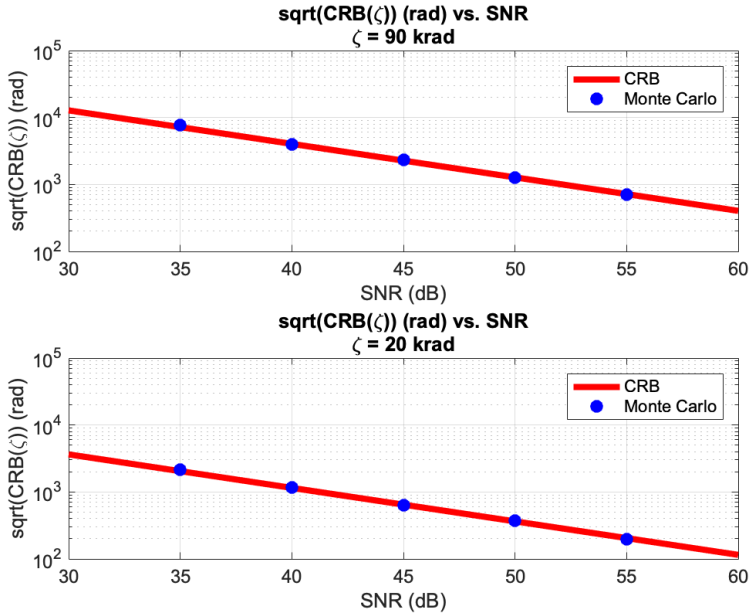

Figure 5.2: Analytic $\sqrt{\text{CRB}(\zeta)}$ in radians for a magnetic, rank-one target with two relaxation frequencies: $\zeta_1 = 90$ krad (top) and $\zeta_2 = 20$ krad (bottom). The solid line corresponds to the CRB, and the circle markers correspond to the standard deviations calculated from the Monte Carlo trials. Excellent agreement between the Monte Carlo analysis and the CRBs is observed.

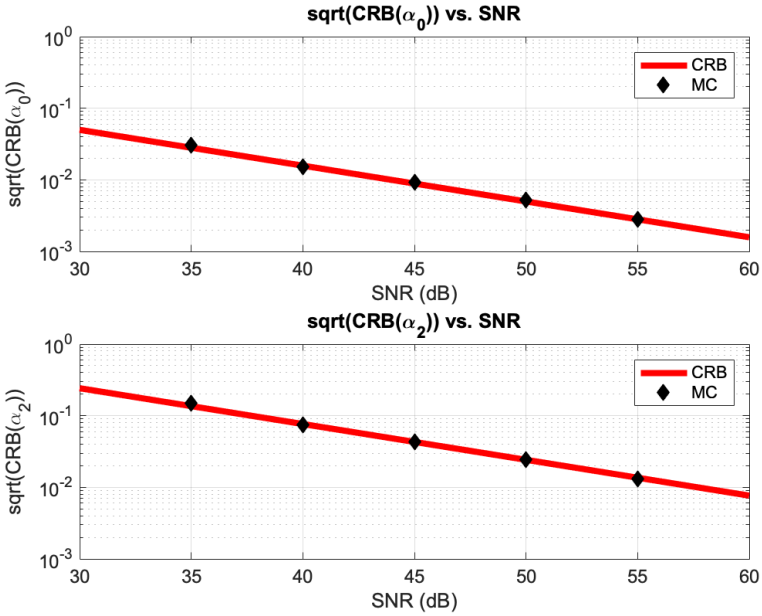

Figure 5.3: CRBs for the α_p parameters (solid line) as a function of SNR along with the sample standard deviations calculated from the Monte Carlo trials (circle markers). Excellent agreement between the Monte Carlo results and the CRBs is observed.

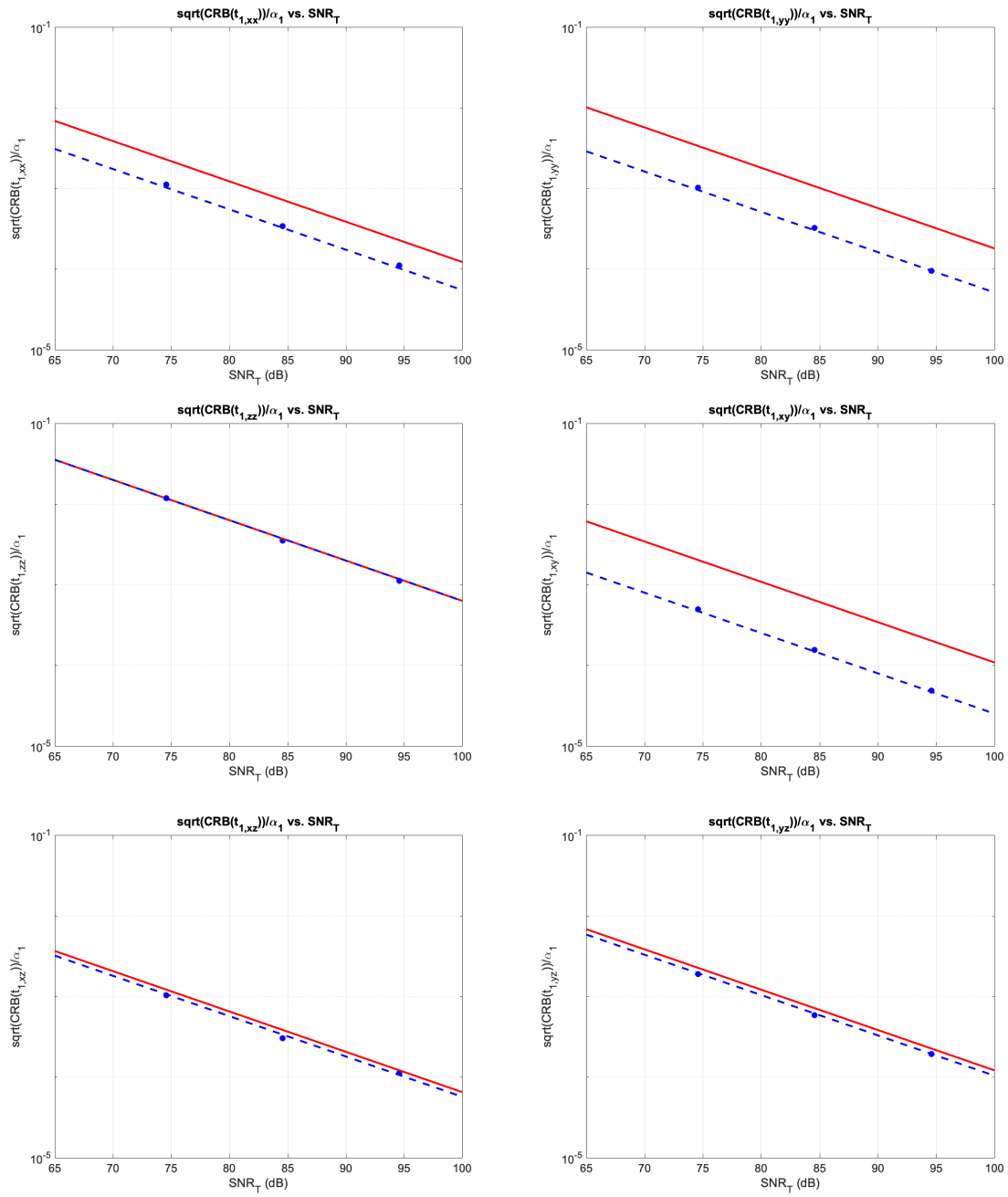

Figure 5.4: Comparison of normalized $\sqrt{\text{CRB}(\boldsymbol{t}_1)}$ for SoD model (red line), SoT model (dashed blue), and Monte Carlo results using MLE (blue circular markers).

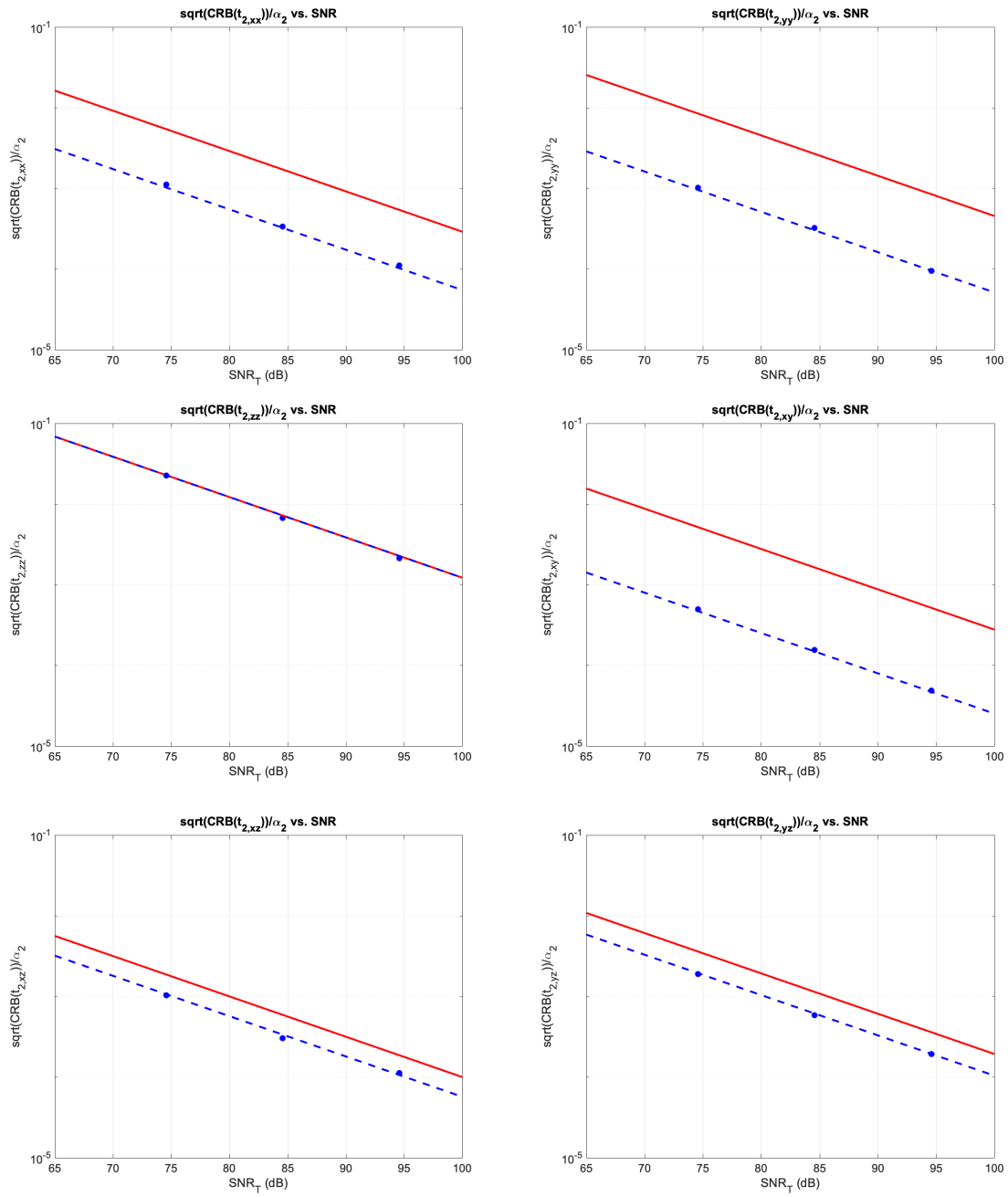

Figure 5.5: Comparison of normalized $\sqrt{\text{CRB}(\boldsymbol{t}_2)}$ for SoD model (red line), SoT model (dashed blue), and Monte Carlo results using MLE (blue circular markers).

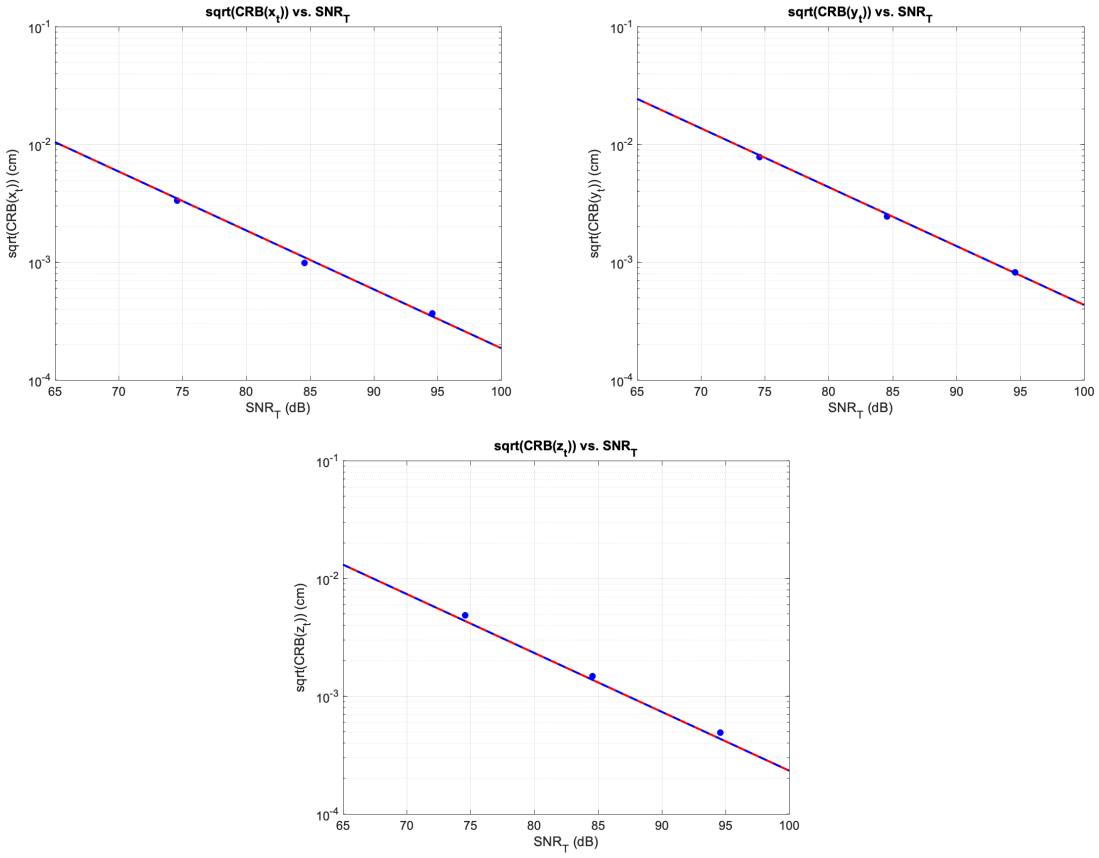

Figure 5.6: Comparison of $\sqrt{\text{CRB}(\boldsymbol{l}_t)}$ for SoD model (red line), SoT model (dashed blue), and Monte Carlo results using MLE (blue circular markers).

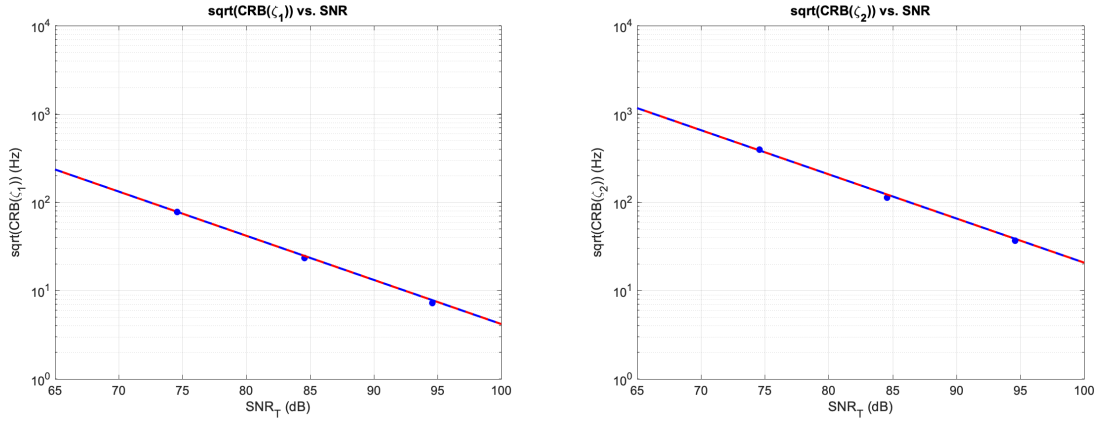

Figure 5.7: Comparison of $\sqrt{\text{CRB}(\boldsymbol{\zeta})}$ for SoD model (red line), SoT model (dashed blue), and Monte Carlo results using MLE (blue circular markers).

CHAPTER 6

APPROXIMATE CRAMER-RAO LOWER BOUNDS FOR RANK-ONE TARGETS

In Chapter 5, we show that the MLEs of the factored models achieve the CRBs based on the SoT model. This suggests that an expression for the variance of the MLEs will match the CRBs as well. As we mention in Section 2.2, the covariance matrix of the MLE asymptotically converges to the inverse of the FIM for the model being considered. Thus, calculating and inverting the FIMs of the unknown parameters based on the factored models allows us to derive approximate CRBs (ACRBs) that are essentially the same as the CRBs in the SoT model but will be a function of fewer parameters. Thus, the goal of this chapter is to derive these ACRB expressions and then compare them to the CRBs for a few example targets.

The ACRBs derived in this chapter for the target location and the relaxation frequencies directly correspond to the CRBs of these same parameters under the SoT and SoD models. However, as we discuss in Section 4.1, the CRBs for the α_p terms and the $\tilde{\boldsymbol{t}}$ term change depending on how these parameters are defined, but the CRBs of the products of these quantities $\boldsymbol{t} = \alpha_p \tilde{\boldsymbol{t}}$ do not. As such, when we derive the ACRBs for the a_p terms and $\boldsymbol{t}_f$ terms which correspond to the amplitudes and the tensor in the factored models respectively, they can be used separately for analysis, but to relate them back to the CRBs under the SoT model, they must be combined. The relationships between the parameters in the factored models and the parameters in the SoT model are discussed in Section 6.1.3 and Section 6.2.3.

6.1 Approximate CRB Expressions for Frequency Parameters

In this section, we derive the approximate CRB expressions for the relaxation frequencies ζ_p and a scaled version of their corresponding amplitudes, a_p.

6.1.1 Derivation

We start the derivation from the factored frequency model in (5.8) for a magnetic target, repeated below in (6.1).

$$\boldsymbol{y} = a_0 - \sum_p a_p \frac{j\boldsymbol{\omega}/\zeta_p}{1 + j\boldsymbol{\omega}/\zeta_p} + \boldsymbol{n}_y \tag{6.1}$$

where $\boldsymbol{n}_y \sim CN\left(\boldsymbol{0}, \sigma_n^2 \boldsymbol{I}\right)$, and the quantity $a_1 = c\alpha_1$ is unknown because c is unknown. The model in (6.1) has $P + 1$ amplitude unknowns, compared to the SoT model which has P amplitude unknowns for the same target. The derivatives with respect to ζ_p, a_p for $p \geq 1$ and a_0 are related to the derivative quantities in Chapter 4 through the following equations:

$$\frac{\partial \boldsymbol{y}}{\partial \zeta_p} = c\boldsymbol{f}'_{\zeta_p} \tag{6.2a}$$

$$\frac{\partial \boldsymbol{y}}{\partial a_p} = \boldsymbol{f}'_{\alpha_p} \tag{6.2b}$$

$$\frac{\partial \boldsymbol{y}}{\partial a_0} = \boldsymbol{f}'_{\alpha_0} \tag{6.2c}$$

The quantities $\boldsymbol{f}'_{\zeta_p}$, $\boldsymbol{f}'_{\alpha_p}$, and $\boldsymbol{f}'_{\alpha_0}$ are the same as in (4.6), (4.9), and (4.10), respectively. We define

$$\boldsymbol{F}'_{\alpha} = \begin{bmatrix} \boldsymbol{f}'_{\alpha_1} & \boldsymbol{F}'_{\alpha-1} \end{bmatrix} \tag{6.3}$$

where $\boldsymbol{F}'_{\alpha-1}$ is the same as from (4.11), so that the FIM is

$$\boldsymbol{I} = \frac{2}{\sigma_n^2} \mathrm{Re}\left\{ \begin{bmatrix} c^2 (\boldsymbol{F}'_{\zeta})^H \boldsymbol{F}'_{\zeta} & c(\boldsymbol{F}'_{\zeta})^H \boldsymbol{F}'_{\alpha} \\ c(\boldsymbol{F}'_{\alpha})^H \boldsymbol{F}'_{\zeta} & (\boldsymbol{F}'_{\alpha})^H \boldsymbol{F}'_{\alpha} \end{bmatrix} \right\} \tag{6.4}$$

where $\boldsymbol{F}'_\zeta$ is the same as in (4.7). Making the substitution for c and using the block matrix inverse on (6.4) yields

$$\begin{aligned}\boldsymbol{C}_{ACR}(\boldsymbol{\zeta}) =& \frac{\sigma_n^2}{2\|\boldsymbol{H}_s(\boldsymbol{l}_t)\tilde{\boldsymbol{t}}\|^2} \cdot \\ & \left(\mathrm{Re}\left\{(\boldsymbol{F}'_\zeta)^H \boldsymbol{F}'_\zeta\right\} - \mathrm{Re}\left\{(\boldsymbol{F}'_\zeta)^H \boldsymbol{F}'_\alpha\right\} \mathrm{Re}\left\{(\boldsymbol{F}'_\alpha)^H \boldsymbol{F}'_\alpha\right\}^{-1} \mathrm{Re}\left\{(\boldsymbol{F}'_\alpha)^H \boldsymbol{F}'_\zeta\right\}\right)^{-1}\end{aligned} \tag{6.5}$$

where $\boldsymbol{\zeta} = [\zeta_1, \zeta_2, \ \ldots, \zeta_p]^T$. The expression for $\boldsymbol{C}_{CR}(\boldsymbol{a})$ is

$$\boldsymbol{C}_{ACR}(\boldsymbol{a}) = \frac{\sigma_n^2}{2} \cdot \left(\mathrm{Re}\left\{(\boldsymbol{F}'_\alpha)^H \boldsymbol{F}'_\alpha\right\} - \mathrm{Re}\left\{(\boldsymbol{F}'_\alpha)^H \boldsymbol{F}'_\zeta\right\} \mathrm{Re}\left\{(\boldsymbol{F}'_\zeta)^H \boldsymbol{F}'_\zeta\right\}^{-1} \mathrm{Re}\left\{(\boldsymbol{F}'_\zeta)^H \boldsymbol{F}'_\alpha\right\}\right)^{-1} \tag{6.6}$$

where $\boldsymbol{a} = [a_1, a_0, a_2, \ \ldots, a_P]^T$. This ordering of $\boldsymbol{a}$ is a result of the ordering of (6.3).

6.1.2 Discussion of ACRB Expressions

The form of $\boldsymbol{C}_{ACR}(\boldsymbol{\zeta})$ is particularly elegant because the impact of the spatial terms, $\boldsymbol{H}_s(\boldsymbol{l}_t)$ and $\tilde{\boldsymbol{t}}$, collapses down to a simple scale factor of the relaxation frequency bounds. This single scale factor captures how the sensor geometry, measurement positions, target location, and target orientation impact the lower bound on the relaxation frequencies, which is a tremendous simplification over the expression in (4.21).

Another benefit of the ACRBs is that they allow for the independent analysis of the frequency and spatial unknowns and how each is impacted by the various *measurement* parameters (i.e., frequency scheme and spatial positions). For example, a parametric analysis of the CRB(ζ) of a non-magnetic target with a single relaxation frequency without the ACRB expression requires the joint consideration of 10 unknowns, whereas the approximate expression reduces that number to 2. We can also use these expressions to analyze the impact of the orientation of the basis tensor separately from the strength of each relaxation frequency. The impact of the orientation of the basis tensor on the ACRBs is captured through the term $\|\boldsymbol{H}_s(\boldsymbol{l}_t)\tilde{\boldsymbol{t}}\|^2$, where we observe that the orientation that maximizes this

quantity gives the best lower bounds. The impact of the strength of each relaxation frequency is captured through the a_p terms, allowing one, for example, to analyze how the relative strengths of the relaxation frequencies impact the respective ACRBs.[1]

$\boldsymbol{C}_{ACR}(\boldsymbol{a})$ is a useful expression for understanding the factors that impact the lower bounds on estimating the a_p terms. While not directly related to any of the unknown parameters in the SoT model, these parameters are important in their own right. As we showed in Chapter 5, combining the MLEs of the $\boldsymbol{a}$ terms with the MLE of the $\boldsymbol{t}_f$ term allowed us to achieve the CRBs under the SoT model for the example we considered. Thus, understanding what impacts the lower bounds on estimating these quantities is important.

Additionally, the a_p parameters are indirectly related to the α_p terms in the SoT model, as well as the $\boldsymbol{t}_p$ terms. We show how to compute $\boldsymbol{C}_{ACR}(\boldsymbol{\alpha})$ from $\boldsymbol{C}_{ACR}(\boldsymbol{a})$ in Section 6.1.3, and then show the relationship between $(a_p, \boldsymbol{t}_f)$ and $\boldsymbol{t}_p$ in Section 6.2.3.

6.1.3 Relating $\boldsymbol{C}_{ACR}(\boldsymbol{a})$ to $\boldsymbol{C}_{ACR}(\boldsymbol{\alpha})$

We can use the transformation property of the CRB to relate $\boldsymbol{C}_{ACR}(\boldsymbol{a})$ to $\boldsymbol{C}_{ACR}(\boldsymbol{\alpha})$. If the α_p terms are defined relative to α_1 as is discussed in Section 4.1, the a_p terms are related to the α_p terms through $\boldsymbol{\alpha} = \boldsymbol{g}(\boldsymbol{a}) = \boldsymbol{a}_n/a_1$ where $\boldsymbol{a}_n = [a_0, a_2, a_3, \ \dots\ , a_p]^T$. We can relate $\boldsymbol{C}_{ACR}(\boldsymbol{\alpha})$ to $\boldsymbol{C}_{ACR}(\boldsymbol{a})$ through

$$\boldsymbol{C}_{ACR}(\boldsymbol{\alpha}) = \left(\frac{\partial \boldsymbol{g}(\boldsymbol{a})}{\partial \boldsymbol{a}}\right) \boldsymbol{C}_{ACR}(\boldsymbol{a}) \left(\frac{\partial \boldsymbol{g}(\boldsymbol{a})}{\partial \boldsymbol{a}}\right)^T \tag{6.7}$$

For the magnetic target case which is being considered in this section, the matrix $\dfrac{\partial \boldsymbol{g}(\boldsymbol{a})}{\partial \boldsymbol{a}} \in \mathbb{R}^{P \times P+1}$ is expressed as

$$\frac{\partial \boldsymbol{g}(\boldsymbol{a})}{\partial \boldsymbol{a}} = \begin{bmatrix} \dfrac{-\boldsymbol{a}_n}{a_1^2} & \dfrac{1}{a_1}\boldsymbol{I}_{P\times P} \end{bmatrix} \tag{6.8}$$

where $\boldsymbol{I}_{P\times P}$ is the identity matrix.

The expression is similar for the non-magnetic case, except $\boldsymbol{a} = [a_1, a_2, \ \dots\ , a_p]^T$, and

[1] This analysis is conducted in Section 7.1.1.

$\boldsymbol{a}_n = [a_2, a_3, \ \ldots \ , a_p]^T$ to keep consistent with the expression in (6.8), and the dimensionality of the identity matrix in (6.8) is different.

6.2 Approximate CRB Expressions for Spatial Parameters

In this section, we derive the ACRB expressions for the tensor $\boldsymbol{t}_f$ in the factored model as well as the target location. We then show how to relate ACRB matrix of $\boldsymbol{t}_f$ to the ACRB matrix of the tensors $\boldsymbol{t}_p$ under the SoT model.

6.2.1 Derivation

We can derive the ACRBs for the spatial parameters in a similar fashion as the frequency parameters. For the derivation, we start with the model in (5.7).

$$\boldsymbol{s} = \sigma_1 \boldsymbol{v}_1 \approx H_s(\boldsymbol{l}_t)\boldsymbol{t}_f + \boldsymbol{n}_v \tag{6.9}$$

where $\boldsymbol{t}_f = q\tilde{\boldsymbol{t}}$, $q = \|\boldsymbol{f}(\boldsymbol{\omega})\|$, the f subscript represents the "factored" model tensor, and $\boldsymbol{n}_v \sim N\left(\boldsymbol{0}, \frac{\sigma_n^2}{2}\boldsymbol{I}\right)$. If we define the following quantities,

$$\boldsymbol{d}_{x_t} = \boldsymbol{H}'_{s,x}(\boldsymbol{l}_t)\tilde{\boldsymbol{t}} \tag{6.10a}$$

$$\boldsymbol{d}_{y_t} = \boldsymbol{H}'_{s,y}(\boldsymbol{l}_t)\tilde{\boldsymbol{t}} \tag{6.10b}$$

$$\boldsymbol{d}_{z_t} = \boldsymbol{H}'_{s,z}(\boldsymbol{l}_t)\tilde{\boldsymbol{t}}, \tag{6.10c}$$

we can write the derivatives of the signal model with respect to each of the location coordinates as

$$\frac{\partial \boldsymbol{s}}{\partial x_t} = q\boldsymbol{d}_{x_t} \tag{6.11a}$$

$$\frac{\partial \boldsymbol{s}}{\partial y_t} = q\boldsymbol{d}_{y_t} \tag{6.11b}$$

$$\frac{\partial \boldsymbol{s}}{\partial z_t} = q\boldsymbol{d}_{z_t} \tag{6.11c}$$

If we define $\boldsymbol{D}_{\boldsymbol{l}_t} = [\boldsymbol{d}_{x_t}, \boldsymbol{d}_{y_t}, \boldsymbol{d}_{z_t}]$, then

$$\begin{bmatrix} \frac{\partial \boldsymbol{s}}{\partial x_t} & \frac{\partial \boldsymbol{s}}{\partial y_t} & \frac{\partial \boldsymbol{s}}{\partial z_t} \end{bmatrix} = q\boldsymbol{D}_{\boldsymbol{l}_t}. \tag{6.12}$$

The derivative of the signal model with respect to $\boldsymbol{t}_f$ is

$$\begin{aligned} \boldsymbol{D}_{\boldsymbol{t}_f} = \frac{\partial \boldsymbol{s}}{\partial \boldsymbol{t}_f} &= \left[\frac{\partial \boldsymbol{s}}{\partial t_{xx}}, \frac{\partial \boldsymbol{s}}{\partial t_{yy}}, \frac{\partial \boldsymbol{s}}{\partial t_{zz}}, \frac{\partial \boldsymbol{s}}{\partial t_{xy}}, \frac{\partial \boldsymbol{s}}{\partial t_{xz}}, \frac{\partial \boldsymbol{s}}{\partial t_{yz}} \right] \\ &= \boldsymbol{H}_s(\boldsymbol{l}_t), \end{aligned} \tag{6.13}$$

We can define a matrix $\boldsymbol{J}(\boldsymbol{\theta})$ as

$$\boldsymbol{J}(\boldsymbol{\theta}) = \begin{bmatrix} \boldsymbol{D}_{\boldsymbol{t}} & q\boldsymbol{D}_{\boldsymbol{l}_t} \end{bmatrix} \tag{6.14}$$

so that the FIM for this model is

$$\boldsymbol{I}(\boldsymbol{\theta}) = \frac{2}{\sigma_n^2}\boldsymbol{J}^T(\boldsymbol{\theta})\boldsymbol{J}(\boldsymbol{\theta}) = \frac{2}{\sigma_n^2}\begin{bmatrix} \boldsymbol{D}_{\boldsymbol{t}}^T\boldsymbol{D}_{\boldsymbol{t}} & q\boldsymbol{D}_{\boldsymbol{t}}^T\boldsymbol{D}_{\boldsymbol{l}_t} \\ q\boldsymbol{D}_{\boldsymbol{l}_t}^T\boldsymbol{D}_{\boldsymbol{t}} & q^2\boldsymbol{D}_{\boldsymbol{l}_t}^T\boldsymbol{D}_{\boldsymbol{l}_t} \end{bmatrix} \tag{6.15}$$

The ACRB matrix for the spatial parameters is then

$$\boldsymbol{C}_{ACR}(\boldsymbol{t}_f, \boldsymbol{l}_t) = \boldsymbol{I}^{-1}(\boldsymbol{\theta}) = \begin{bmatrix} \boldsymbol{C}_{ACR}(\boldsymbol{t}_f) & \boldsymbol{C}_{ACR}(\boldsymbol{t}_f, \boldsymbol{l}_t) \\ \boldsymbol{C}_{ACR}(\boldsymbol{l}_t, \boldsymbol{t}_f) & \boldsymbol{C}_{ACR}(\boldsymbol{l}_t) \end{bmatrix} \tag{6.16}$$

where the diagonal matrices contain the ACRBs for $\boldsymbol{t}_f$ and $\boldsymbol{l}_t$. Block matrix inversion can be used to generate explicit expressions for the ACRB matrices along the diagonal:

$$\boldsymbol{C}_{ACR}(\boldsymbol{t}_f) = \frac{\sigma_n^2}{2}\left(\boldsymbol{H}_s^T\boldsymbol{H}_s - \boldsymbol{H}_s^T\boldsymbol{D}_{l_t}\left(\boldsymbol{D}_{l_t}^T\boldsymbol{D}_{l_t}\right)^{-1}\boldsymbol{D}_{l_t}^T\boldsymbol{H}_s\right)^{-1} \tag{6.17a}$$

$$\boldsymbol{C}_{ACR}(\boldsymbol{l}_t) = \frac{\sigma_n^2}{2\|\boldsymbol{f}(\boldsymbol{\omega})\|^2}\left(\boldsymbol{D}_{l_t}^T\boldsymbol{D}_{l_t} - \boldsymbol{D}_{l_t}^T\boldsymbol{H}_s\left(\boldsymbol{H}_s^T\boldsymbol{H}_s\right)^{-1}\boldsymbol{H}_s^T\boldsymbol{D}_{l_t}\right)^{-1} \tag{6.17b}$$

In (6.17a) and (6.17b), we drop the argument of $\boldsymbol{H}_s(\boldsymbol{l}_t)$ to simplify the notation and just use $\boldsymbol{H}_s$ to represent the same quantity.

6.2.2 Discussion of ACRB Expressions

The form of $\boldsymbol{C}_{ACR}(\boldsymbol{l}_t)$ is particularly elegant because the impact of the target's relaxation frequency response on the ACRB of the target position is captured by a single scale factor $\|\boldsymbol{f}(\boldsymbol{\omega})\|^2$. This is a useful simplification over the expression in (4.21) because it allows for the analysis of the ACRBs of the location parameters independent of the frequency parameters. The expression also allows for a more intuitive understanding of the factors that impact the ACRBs of the location coordinates.

The expression for $\boldsymbol{C}_{ACR}(\boldsymbol{t}_f)$ is useful for understanding the factors that influence the lower bounds on estimating the $\boldsymbol{t}_f$ term. While not directly related to any of the unknown parameters in the SoT parameters, this term is an important component of the target tensors. As we showed in Chapter 5, combining the MLE of $\boldsymbol{t}_f$ with the MLE of the $\boldsymbol{a}$ terms allowed us to achieve the CRBs under the SoT model for the example we considered. Therefore, understanding how well one can estimate this term and the factors that influence these bounds is critical.[2]

[2] Analysis of the spatial parameters in the factored model can be found in Section 7.2.

6.2.3 Relationship to SoT Model Parameters

We can relate the ACRB expressions for $\boldsymbol{a}$ and $\boldsymbol{t}_f$ to ACRB($\boldsymbol{t}_p$) following the same procedure as in Section 4.4. We first define the relationship between these quantities as

$$\boldsymbol{t}_p = \boldsymbol{g}(a_p, \boldsymbol{t}) = \frac{1}{\|\boldsymbol{f}(\boldsymbol{\omega})\|\|\boldsymbol{H}_s(\boldsymbol{l}_t)\tilde{\boldsymbol{t}}\|} a_p \boldsymbol{t}_f \tag{6.18}$$

The ACRB matrix for $\boldsymbol{t}_p$ is then related to the ACRBs of a_p and $\boldsymbol{t}_f$ as

$$\boldsymbol{C}_{ACR,\text{SoT}}(\boldsymbol{t}_p) = \left(\frac{\partial \boldsymbol{g}(\boldsymbol{\theta})}{\partial \boldsymbol{\theta}}\right) \boldsymbol{C}_{ACR}(a_p;\ \boldsymbol{t}_f) \left(\frac{\partial \boldsymbol{g}(\boldsymbol{\theta})}{\partial \boldsymbol{\theta}}\right)^T \tag{6.19}$$

where

$$\boldsymbol{C}_{ACR}(a_p;\ \boldsymbol{t}_f) = \begin{bmatrix} \boldsymbol{C}_{ACR}(a_p) & \boldsymbol{0}_{1\times 6} \\ \boldsymbol{0}_{6\times 1} & \boldsymbol{C}_{ACR}(\boldsymbol{t}_f) \end{bmatrix} \tag{6.20}$$

and

$$\frac{\partial \boldsymbol{g}(\boldsymbol{\theta})}{\partial \boldsymbol{\theta}} = \begin{bmatrix} \frac{\partial \boldsymbol{g}(\boldsymbol{\theta})}{\partial a_p} & \frac{\partial \boldsymbol{g}(\boldsymbol{\theta})}{\partial \boldsymbol{t}_f} \end{bmatrix} = \frac{1}{\|\boldsymbol{f}(\boldsymbol{\omega})\|\|\boldsymbol{H}_s(\boldsymbol{l}_t)\tilde{\boldsymbol{t}}\|} \begin{bmatrix} \tilde{\boldsymbol{t}} & a_p \boldsymbol{I}_{6\times 6} \end{bmatrix} \tag{6.21}$$

The off-diagonal vectors of zeros in (6.20), $\boldsymbol{0}_{[\cdot]}$, result from the fact that the covariance of those parameters is zero because they are estimated separately and thus have no interdependence.

6.3 Examples

In this section, we consider two example targets. The first example is a rank-one magnetic target with two relaxation frequencies. The analysis corresponding to this target explores how well the ACRB expressions match the CRBs from the SoT model for the relaxation frequencies and their corresponding amplitudes. The second example is a rank-one target with two relaxation frequencies. The analysis corresponding to this target explores how well the ACRB expressions match the CRBs from the SoT model for the tensors and the target location. Between the two examples, we cover all of the unknown parameters in the

EMI model.

6.3.1 Example 1: Magnetic Target with Two Relaxation Frequencies

In this section, we consider the exact same magnetic target with two relaxation frequencies from Section 5.2.3; however, we fix the SNR_{ζ_p} to be 50 dB for each relaxation frequency and perform Monte Carlo analysis. For the Monte Carlo analysis, we simulate $10,000$ measurements directly using the model in (6.1) and estimate the unknown parameters for each trial using the MLE in (5.9). We are interested in the distributions of the estimation errors for ζ_1 and ζ_2, and verifying that they both are nearly normally distributed and that the parameters of the distribution match what is expected from the CRB and ACRB.

To do this, we generate a scatter plot of the relaxation frequency errors and overlay the expected error ellipses generated from the CRB matrix in (4.21) and the ACRB matrix in (6.5). We also derive the data-driven error ellipse from the estimated covariance matrix. This graphic is shown in the top part of Figure 6.1. The error ellipses generated using the CRB matrix, ACRB matrix, and the data-driven error ellipse all overlay each other, suggesting the ACRB matrix well describes the covariance of the MLE of the relaxation frequencies, and is a good approximation for the lower bound on the covariance of the relaxation frequencies based on the SoT model.

We also show histograms of the estimation errors for each relaxation frequency in the bottom of Figure 6.1. Overlaid on each histogram is a fitted normal distribution based on the underlying data. We observe reasonable agreement between the underlying data and a normal distribution at this SNR, which gives us confidence that the MLE is normally distributed. Additionally, the standard deviations of the fitted normal distributions match the CRBs and ACRBs, which is also observable in Figure 5.2.

The equivalent plots for the α_p terms are shown in the top and bottom halves of Figure 6.2. The amplitudes are estimated for each trial using $\hat{\alpha}_p = \hat{a}_p/\hat{a}_1$.

We calculate the ACRB error ellipse based on the ACRB matrix for $\boldsymbol{\alpha}$ from (6.7). We

calculate the error ellipse based on the CRB matrix based on (4.21). We also calculate the data-driven error ellispse from the estimated covariance matrix from the Monte Carlo trials.

In the top half of the figure, we observe good agreement between the error ellipse generated from the CRB matrix, the ACRB matrix transformation, and the one derived from the data, suggesting that the transformed ACRB matrix reasonably describes the data and is a good approximation to the CRB matrix for the α parameters as well.

Histograms of the amplitude errors are shown in the bottom half of the figure, again with a fitted normal distribution overlaid on each. The variance of the errors matches the CRB, and the distribution is reasonably approximated by the normal distribution, which is the expected result based on the invariance property of the MLE.

6.3.2 Example 2: Target with a Single Basis Tensor and Two Relaxation Frequencies

In this section, we compare the ACRBs derived in this section to the CRBs from the SoT model for a target with a single basis tensor and two relaxation frequencies as a means of validating the ACRB expressions.

We assume the single tensor is defined as $\tilde{\boldsymbol{t}}_1 = [4, 0, 4, 0, 0, 0]^T$, and $\alpha_2 = .5$. The target has two relaxation frequencies, $\zeta_1 = 20$ kHz, and $\zeta_2 = 80$ kHz. The target SNR is approximately $\text{SNR}_\text{T} = 100$ dB. We assume the target is measured over the scan pattern in Figure 2.3 using the sensor in Figure 2.2. Additionally, we assume the target is measured using the log-spaced frequency scheme in Section 2.6. Lastly, we assume the target is located at $\boldsymbol{l}_t = (0, 0, 4)$ cm.

For the Monte Carlo analysis, we simulate 1000 measurements according to the model in (4.2). We use the SVD to factor the model into its spatial and frequency components like in Chapter 5, and estimate the tensor and location using the MLE in (5.10), and the a_p terms and ζ_p terms from (5.9). For each trial, we estimate $\boldsymbol{t}_1$ and $\boldsymbol{t}_2$ using (5.11) which combines the a_p estimate with the $\boldsymbol{t}_f$ estimate.

In Figure 6.3, we compare the estimated error ellipses from the Monte Carlo trials to

the error ellipses derived from the ACRB matrices and the CRB matrices. We show the error distributions of three pairs of parameters: $(t_{1,xx}, t_{1,zz})$, $(t_{2,xx}, t_{2,zz})$, and (x_t, z_t). For the $(t_{1,xx}, t_{1,zz})$ and $(t_{2,xx}, t_{2,zz})$ error distributions shown in Figure 6.3a and Figure 6.3b respectively, the dashed red line corresponds to the error ellipse based on the transformed CRB matrix in (4.25). The dot-dashed black line corresponds to the error ellipse based on the transformed ACRB matrix in (6.19). The dotted magenta line corresponds to the error ellipse based on the covariance matrix estimated from the data (i.e., the data-driven error ellipse). We observe for both figures that the three error ellipses are essentially overlayed, which allows us to draw the following conclusions: the ACRB matrix is a good approximation to the CRB matrix for the parameters considered for this example, and that the ACRB expression in (6.17a) was derived correctly because the data-driven error ellipse matches the one based on the ACRB matrix.

We make similar observations for the location parameters considered in Figure 6.3c. The ACRB error ellipse (dot-dashed black line) based on (6.17b) matches the CRB error ellipse (dashed red line) based on the entries in (4.21). Both of these error ellipses match the data-driven error ellipse (dotted magenta line), which validates the ACRB expression in (6.17b).

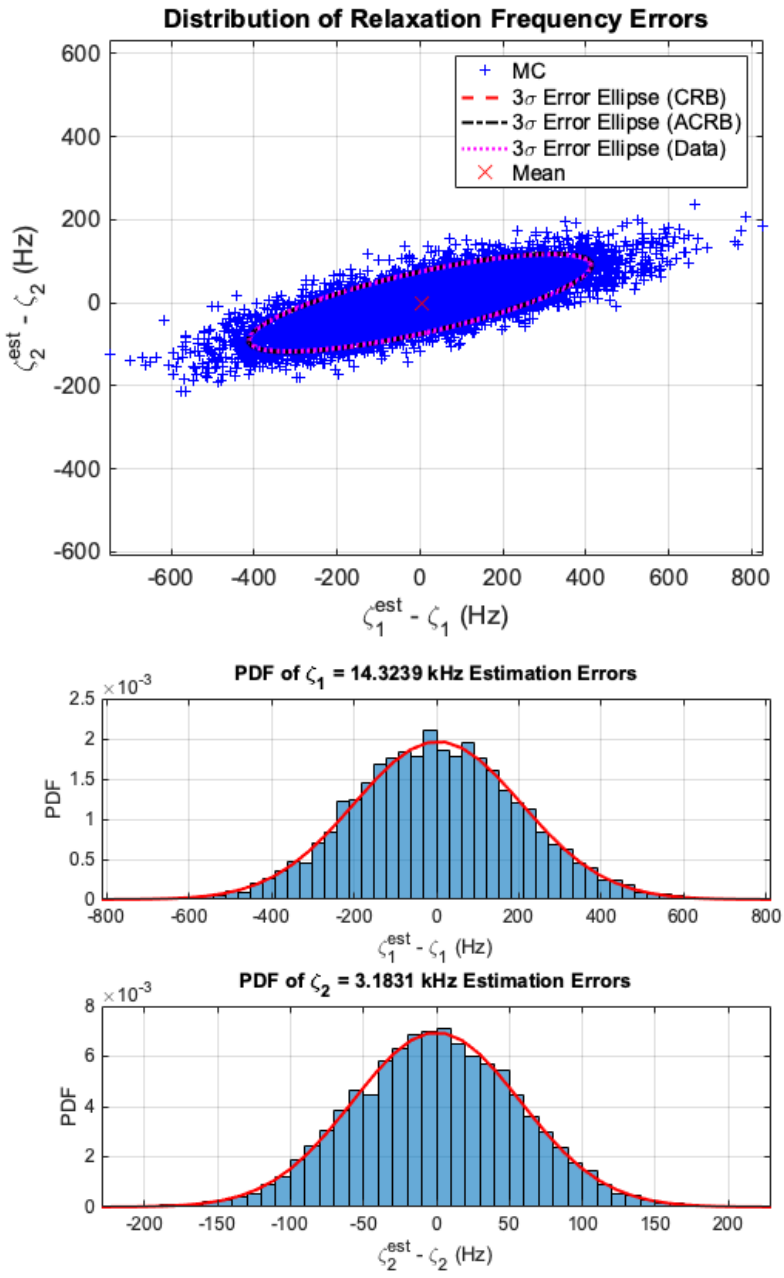

Figure 6.1: (Top) Scatter plot of the estimation errors for ζ_1 and ζ_2 for 10,000 Monte Carlo trials at 50 dB SNR. The 3σ error ellipses generated using the CRB matrix and ACRB matrix are overlaid, along with the ellipse derived from the underlying Monte Carlo data. (Bottom) Histograms of the estimation errors for both relaxation frequencies. A fitted normal distribution is overlaid (solid) for each. The parameters of the normal distributions match the expected distributions based on the CRB.

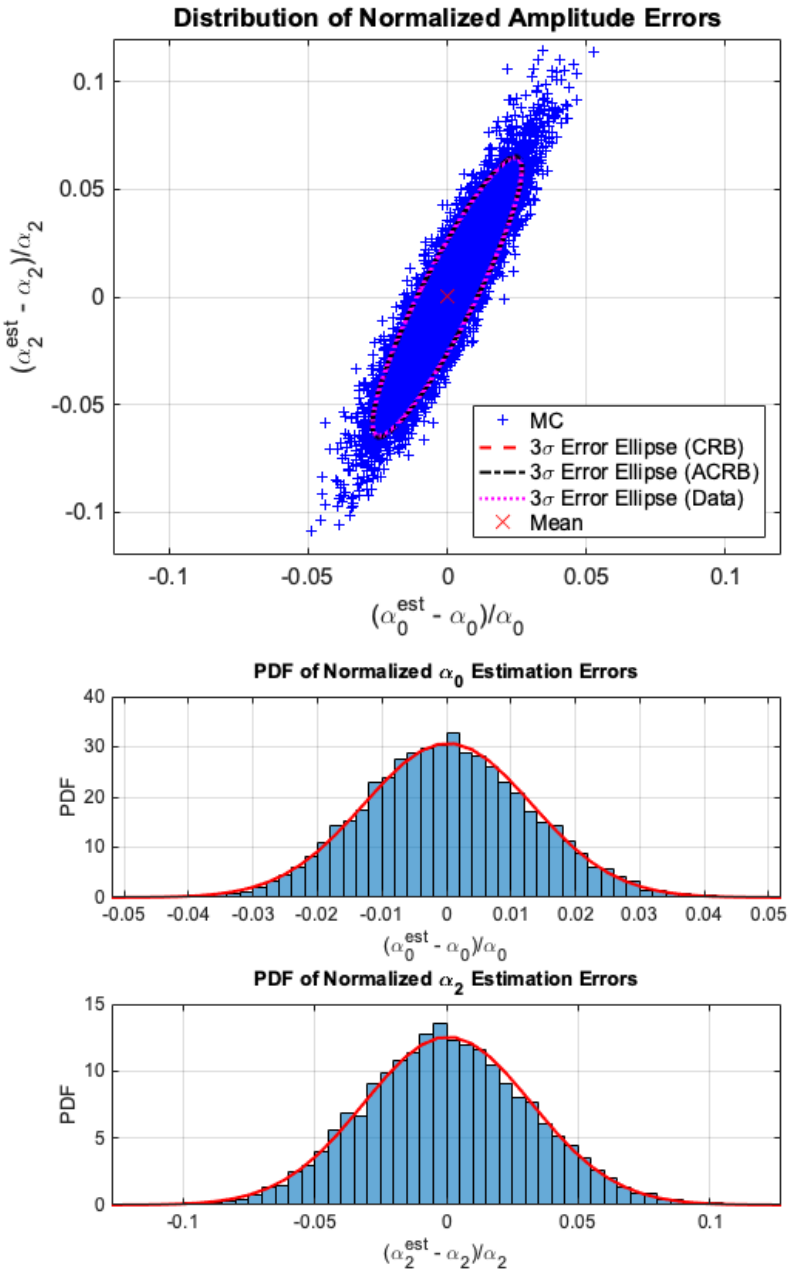

Figure 6.2: (Top) Scatter plot of the estimation errors for α_0 and α_2 for 10,000 Monte Carlo trials at 50 dB SNR. A 3σ error ellipse generated using the CRB matrix, ACRB matrix, and an error ellipse derived from the underlying Monte Carlo data are overlaid. (Bottom) Histograms of the estimation errors for estimated amplitudes. A fitted normal distribution is overlaid (solid line) for each.

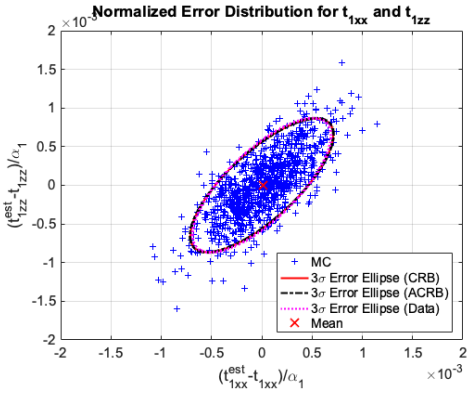

(a) Scatter plot of $(t_{1,xx}, t_{1,zz})$ estimation errors with various error ellipses overlayed.

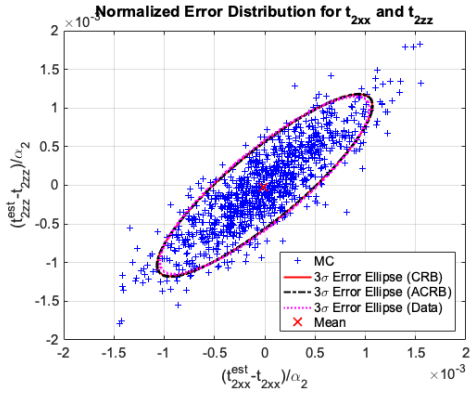

(b) Scatter plot of $(t_{2,xx}, t_{2,zz})$ estimation errors with various error ellipses overlayed.

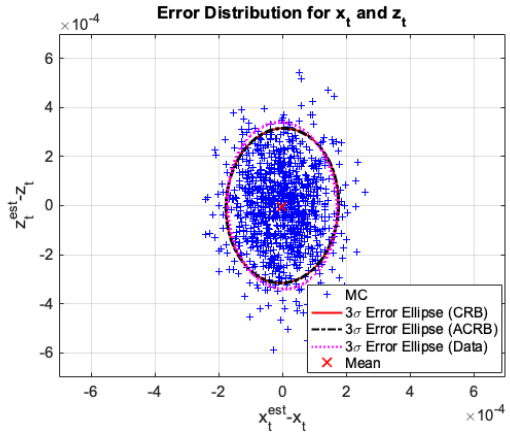

(c) Scatter plot of (x_t, z_t) estimation errors with various error ellipses overlayed.

Figure 6.3: Comparison of data-driven error ellipses of various parameters to error ellipses derived from the SoT CRB matrix and the ACRB matrix.

CHAPTER 7
RANK-ONE TARGET ANALYSIS

In this chapter, we use the ACRB expressions derived for rank-one targets to carry out different types of analyses for the frequency and spatial unknowns. For the analyses, we assume the system parameters of the Georgia Tech frequency-domain EMI system in Section 2.6, though some of conclusions drawn are applicable to other EMI systems. Through these analyses, we develop a better understanding of how the lower bounds on the unknown parameters change for different measurement scenarios and for different target models. Additionally, we show how the Fisher information matrix can be used to diagnose system deficiencies as they relate to estimating the unknown parameters.

Section 7.1 contains three sub-sections with each dedicated to a different type of analysis related to the frequency unknowns. Section 7.2 contains four sub-sections with each dedicated to analyses of the spatial unknowns in the factored spatial model.

7.1 Frequency Parameter Analysis

This section contains three sub-sections with each dedicated to a different type of analysis related to the frequency unknowns. In Section 7.1.1, we derive an alternate expression for the ACRB of the relaxation frequencies for the two relaxation case. The alternate expression shows that the ACRB for each relaxation is inversely proportional to the square of the corresponding amplitude, and is independent of the strength of the other relaxation's amplitude. We then validate the expressions through simulation. In Section 7.1.2, we explore the increase in the CRB of a relaxation due to the presence of a secondary relaxation for a variety of different relaxation frequency spacings. We show that the closer the spacing between the relaxation frequencies, the greater the increase in the CRB due to the presence of the secondary relaxation. In fact, the two relaxations need to be spaced at least a decade

apart to keep the increase in the CRB to a factor of 3 or less. In Section 7.1.3, we derive an expression for the minimum-mean-square error of an unbiased estimator of the relaxation frequencies. We explore this expression as a function of the number of modeled relaxation frequencies and show that this quantity increases as the number of relaxations increases, primarily because the spacing between the relaxation frequencies decreases.

7.1.1 Relaxation Frequency ACRBs vs. Relative Amplitudes

In this section, we derive an alternate expression for the ACRB of the relaxation frequencies, derived in Chapter 4, for the two relaxation frequency case.

We begin with the original expression for the ACRB from (6.5):

$$\begin{aligned} \boldsymbol{C}_{ACR}(\boldsymbol{\zeta}) &= \frac{\sigma_n^2}{2\|\boldsymbol{H}_s(\boldsymbol{l}_t)\tilde{\boldsymbol{t}}\|^2} \cdot \\ &\left(\mathrm{Re}\left\{(\boldsymbol{F}'_\zeta)^H \boldsymbol{F}'_\zeta\right\} - \mathrm{Re}\left\{(\boldsymbol{F}'_\zeta)^H \boldsymbol{F}'_\alpha\right\} \mathrm{Re}\left\{(\boldsymbol{F}'_\alpha)^H \boldsymbol{F}'_\alpha\right\}^{-1} \mathrm{Re}\left\{(\boldsymbol{F}'_\alpha)^H \boldsymbol{F}'_\zeta\right\}\right)^{-1} \end{aligned} \tag{7.1}$$

The objective is to isolate a term that depends only on the amplitudes from the four-term expression in parentheses in (7.1). Since the derivative $\boldsymbol{F}'_\alpha$ does not depend on the amplitudes, we concentrate on the terms involving $\boldsymbol{F}'_\zeta$. We can factor the amplitudes out of any $\boldsymbol{F}'_\zeta$ term by expressing (4.7) for the two relaxation frequency case as

$$\boldsymbol{F}'_\zeta = \left[\check{\boldsymbol{f}}'_{\zeta_1}, \check{\boldsymbol{f}}'_{\zeta_2}\right] \underbrace{\begin{bmatrix} \alpha_1 & 0 \\ 0 & \alpha_2 \end{bmatrix}}_{\boldsymbol{A}} \tag{7.2}$$

where α_1 and α_2 are real, the matrix $\boldsymbol{A} \in \mathbb{R}^{2\times 2}$, and we define $\check{\boldsymbol{F}}'_\zeta = \left[\check{\boldsymbol{f}}'_{\zeta_1}, \check{\boldsymbol{f}}'_{\zeta_2}\right] \in \mathbb{R}^{M\times 2}$, with columns

$$\check{\boldsymbol{f}}'_{\zeta_p} = \frac{j\boldsymbol{\omega}}{(j\boldsymbol{\omega} + \zeta_p)^2} \tag{7.3}$$

The first term in parentheses, $\mathrm{Re}\left\{(\boldsymbol{F}'_\zeta)^H \boldsymbol{F}'_\zeta\right\}$, can be simplified as

$$\mathrm{Re}\left\{(\boldsymbol{F}'_\zeta)^H \boldsymbol{F}'_\zeta\right\} = \mathrm{Re}\left\{\boldsymbol{A}^H (\check{\boldsymbol{F}}'_\zeta)^H \check{\boldsymbol{F}}'_\zeta \, \boldsymbol{A}\right\} = \boldsymbol{A}\, \mathrm{Re}\left\{(\check{\boldsymbol{F}}'_\zeta)^H \check{\boldsymbol{F}}'_\zeta\right\} \boldsymbol{A} \tag{7.4}$$

Since $\boldsymbol{A}$ is real, we have $\boldsymbol{A}^H = \boldsymbol{A}$, which also allows us to factor $\boldsymbol{A}$ out of the $\mathrm{Re}\{\cdot\}$ operation. Next, we simplify the second and fourth terms, $(\boldsymbol{F}'_\zeta)^H \boldsymbol{F}'_\alpha$ and $(\boldsymbol{F}'_\alpha)^H \boldsymbol{F}'_\zeta$, in the same way

$$\mathrm{Re}\left\{(\boldsymbol{F}'_\zeta)^H \boldsymbol{F}'_\alpha\right\} = \mathrm{Re}\left\{\boldsymbol{A} (\check{\boldsymbol{F}}'_\zeta)^H \check{\boldsymbol{F}}'_a\right\} = \boldsymbol{A}\, \mathrm{Re}\left\{(\check{\boldsymbol{F}}'_\zeta)^H \check{\boldsymbol{F}}'_a\right\} \tag{7.5a}$$

$$\mathrm{Re}\left\{(\boldsymbol{F}'_\alpha)^H \boldsymbol{F}'_\zeta\right\} = \mathrm{Re}\left\{(\check{\boldsymbol{F}}'_a)^H \check{\boldsymbol{F}}'_\zeta \, \boldsymbol{A}\right\} = \mathrm{Re}\left\{(\check{\boldsymbol{F}}'_a)^H \check{\boldsymbol{F}}'_\zeta\right\} \boldsymbol{A} \tag{7.5b}$$

Now, the product of the second through fourth terms in (7.1) becomes

$$\mathrm{Re}\left\{(\boldsymbol{F}'_\zeta)^H \boldsymbol{F}'_\alpha\right\} \mathrm{Re}\left\{(\boldsymbol{F}'_\alpha)^H \boldsymbol{F}'_\alpha\right\}^{-1} \mathrm{Re}\left\{(\boldsymbol{F}'_\alpha)^H \boldsymbol{F}'_\zeta\right\} \tag{7.6a}$$

$$= \boldsymbol{A} \left(\mathrm{Re}\left\{(\check{\boldsymbol{F}}'_\zeta)^H \check{\boldsymbol{F}}'_a\right\} \mathrm{Re}\left\{(\boldsymbol{F}'_\alpha)^H \boldsymbol{F}'_\alpha\right\}^{-1} \mathrm{Re}\left\{(\check{\boldsymbol{F}}'_a)^H \check{\boldsymbol{F}}'_\zeta\right\}\right) \boldsymbol{A} \tag{7.6b}$$

Since the inverse of a matrix product is the product of the inverses (in reverse order), substituting the expressions (7.4) and (7.6b) back into (7.1) and factoring out $\boldsymbol{A}^{-1}$ yields

$$\boldsymbol{C}_{ACR}(\boldsymbol{\zeta}) = \frac{\sigma_n^2}{2\|\boldsymbol{H}_s(\boldsymbol{l}_t)\tilde{\boldsymbol{t}}\|^2} \cdot \left(\boldsymbol{A}^{-1} \left(\mathrm{Re}\left\{(\check{\boldsymbol{F}}'_\zeta)^H \check{\boldsymbol{F}}'_\zeta\right\} - \mathrm{Re}\left\{(\check{\boldsymbol{F}}'_a)^H \check{\boldsymbol{F}}'_\zeta\right\} \mathrm{Re}\left\{(\check{\boldsymbol{F}}'_a)^H \check{\boldsymbol{F}}'_a\right\}^{-1} \mathrm{Re}\left\{(\check{\boldsymbol{F}}'_\zeta)^H \check{\boldsymbol{F}}'_a\right\}\right)^{-1} \boldsymbol{A}^{-1}\right) \tag{7.7}$$

We define the following 2×2 matrix to hold the expression for the inverse in the inner parentheses in (7.7).

$$\begin{bmatrix} a & b \\ c & d \end{bmatrix} = \left(\mathrm{Re}\left\{(\check{\boldsymbol{F}}'_\zeta)^H \check{\boldsymbol{F}}'_\zeta\right\} - \mathrm{Re}\left\{(\check{\boldsymbol{F}}'_\zeta)^H \check{\boldsymbol{F}}'_a\right\} \mathrm{Re}\left\{(\check{\boldsymbol{F}}'_a)^H \check{\boldsymbol{F}}'_a\right\}^{-1} \mathrm{Re}\left\{(\check{\boldsymbol{F}}'_a)^H \check{\boldsymbol{F}}'_\zeta\right\}\right)^{-1} \tag{7.8}$$

where a, b, c and d are functions of the relaxations $\boldsymbol{\zeta}$, but not the amplitudes $\boldsymbol{\alpha}$. To be

explicit, we could alternatively write $a(\boldsymbol{\zeta})$, $b(\boldsymbol{\zeta})$, $c(\boldsymbol{\zeta})$ and $d(\boldsymbol{\zeta})$. Finally, we simplify (7.7) to obtain

$$\boldsymbol{C}_{ACR}(\boldsymbol{\zeta}) = \frac{\sigma_n^2}{2\|\boldsymbol{H}_s(\boldsymbol{l}_t)\tilde{\boldsymbol{t}}\|^2} \begin{bmatrix} 1/\alpha_1 & 0 \\ 0 & 1/\alpha_2 \end{bmatrix} \begin{bmatrix} a(\boldsymbol{\zeta}) & b(\boldsymbol{\zeta}) \\ b(\boldsymbol{\zeta}) & d(\boldsymbol{\zeta}) \end{bmatrix} \begin{bmatrix} 1/\alpha_1 & 0 \\ 0 & 1/\alpha_2 \end{bmatrix} \tag{7.9a}$$

$$= \frac{\sigma_n^2}{2\|\boldsymbol{H}_s(\boldsymbol{l}_t)\tilde{\boldsymbol{t}}\|^2} \begin{bmatrix} a(\boldsymbol{\zeta})/\alpha_1^2 & b(\boldsymbol{\zeta})/\alpha_1\alpha_2 \\ b(\boldsymbol{\zeta})/\alpha_1\alpha_2 & d(\boldsymbol{\zeta})/\alpha_2^2 \end{bmatrix} \tag{7.9b}$$

By observing the diagonal terms, we note the following interesting result:

$$\text{ACRB}(\zeta_1) = \frac{\sigma_n^2}{2\alpha_1^2\|\boldsymbol{H}_s(\boldsymbol{l}_t)\tilde{\boldsymbol{t}}\|^2} \cdot a(\zeta_1, \zeta_2) \tag{7.10a}$$

$$\text{ACRB}(\zeta_2) = \frac{\sigma_n^2}{2\alpha_2^2\|\boldsymbol{H}_s(\boldsymbol{l}_t)\tilde{\boldsymbol{t}}\|^2} \cdot d(\zeta_1, \zeta_2) \tag{7.10b}$$

where $a(\boldsymbol{\zeta})$ and $d(\boldsymbol{\zeta})$ are different functions of $\boldsymbol{\zeta} = [\zeta_1, \zeta_2]$ obtained from the inverse in (7.8). In words, the ACRB for each relaxation frequency is a function of the two relaxation frequencies, but they are independent of the other relaxation frequency's amplitude. In fact, The ACRB of each relaxation is inversely proportional to the square of its own amplitude.[1]

To verify the above claims, we generate the ACRBs of the relaxation frequencies for the case of a non-magnetic z-directed dipole target located at $\boldsymbol{l}_t = (0, 0, 7.5)$ cm with two relaxation frequencies, $\zeta_1 = 3.2$ kHz and $\zeta_2 = 14.3$ kHz, as a function of α_2 for a fixed noise variance of $\sigma_n^2 = 10^{-6}$ and a fixed value of $\alpha_1 = 1$. We also perform Monte Carlo analysis to validate the bounds by generating 500 measurement realizations and estimating the relaxation frequencies and amplitudes for each measurement realization. We use the Georgia Tech handheld EMI sensor to generate the measurements. We repeat this process for multiple values of α_2. We calculate the sample standard deviation of the relaxation

[1]The "independence" conclusion and the foregoing derivation can be extended to more than two relaxations by augmenting the $\boldsymbol{A}$ matrix to include additional amplitude terms and augmenting the matrix in (7.8) to account for the additional unknowns in the model.

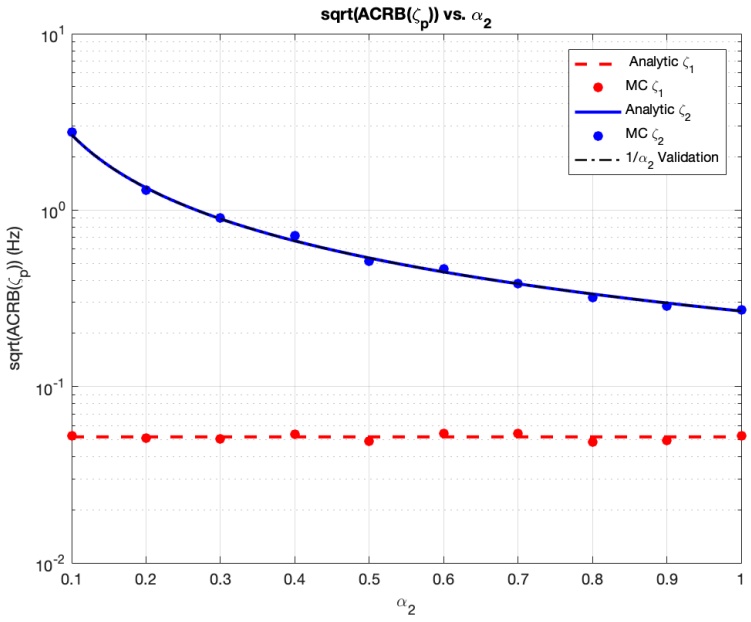

Figure 7.1: $\sqrt{\text{ACRB}}$ for two relaxation frequencies as a function of α_2. The solid line corresponds to ζ_2 and the dashed line corresponds to ζ_1. The dot-dash line corresponds to $1/\alpha_2\sqrt{\text{ACRB}(\zeta_2, \alpha_2 = 1)}$. The Monte Carlo results are shown as circular markers. The dot-dashed line agrees with $\sqrt{\text{ACRB}(\zeta_2)}$ which validates the proportionality expression in (7.10b). We also observe that $\sqrt{\text{ACRB}(\zeta_1)}$ does not change as a function of α_2 which confirms that they are independent. Lastly, the Monte Carlo results match the analytic bounds, giving us confidence that the derived quantities are correct.

frequencies at each value of α_2 and compare these values to the analytic bounds.

The analytic bounds from (7.1) are shown along with the Monte Carlo results in Figure 7.1 for each relaxation frequency. Additionally, to validate the $\text{ACRB}(\zeta_2) \propto 1/\alpha_2^2$ relationship, or equivalently $\sqrt{\text{ACRB}(\zeta_2)} \propto 1/\alpha_2$, we plot a third quantity that corresponds to $\sqrt{\frac{1}{\alpha_2^2}\text{ACRB}(\zeta_2)_{\alpha_2=1}}$. Since α_2 is the only variable changing for this simulation, the curve should match the analytic bound as well as the Monte Carlo results.

We observe from Figure 7.1 that $\text{ACRB}(\zeta_1)$ is independent of α_2, and that $\text{ACRB}(\zeta_2)$ is proportional to $1/\alpha_2^2$, indicated by the fact that the dot-dash curve overlays the analytic curve for $\text{ACRB}(\zeta_2)$. We also observe that the Monte Carlo results for both relaxation frequencies match the analytic bounds, giving us confidence that the derived relationships are correct.

7.1.2 CRBs for Two Relaxation Frequencies vs. Frequency Spacing

In Section 7.1.1, we show that for a rank-one target with two relaxation frequencies, the ACRBs of the relaxation frequencies are independent of the other relaxation's amplitude. In this section, we explore the increase in the ACRB for the relaxation frequency ζ_1 due to the presence of another relaxation frequency ζ_2. We define the increase in the CRB as the ratio of the CRB of ζ_1 when ζ_2 is present ($\text{CRB}(\zeta_1, \zeta_2)$) to the CRB of ζ_1 when ζ_2 is not present ($\text{CRB}(\zeta_1)$. This ratio, denoted as Δ_{CRB}, is shown in (7.11).

$$\Delta_{\text{CRB}} = \frac{\text{CRB}(\zeta_1, \zeta_2)}{\text{CRB}(\zeta_1)} \tag{7.11}$$

We compute this ratio for multiple different fixed values of ζ_1 while ζ_2 is swept within the measurement bandwidth of the Georgia-Tech EMI system. The ratio as a function of the log-spacing between ζ_1 and ζ_2 is shown in Figure 7.2 for the different ζ_1 values.

We observe from Figure 7.2 that Δ_{CRB} is inversely proportional to the spacing between the two frequencies. As the spacing between the two relaxations decreases, Δ_{CRB} increases. This makes intuitive sense because the correlation of the two relaxations increases as they move closer together in frequency, making them more difficult to distinguish from an estimation perspective. Interestingly, the curves are quite similar for the different values of ζ_1, even though they're in different parts of the measurement band. Additionally, based on the figure, two relaxation frequencies need to be spaced approximately one decade apart for Δ_{CRB} to be three or less. When the relaxation frequencies are spaced less than half a decade apart, the increase in the CRB due to the presence of ζ_2 is more than a factor of 10 larger than when it is not present.

7.1.3 Minimum Root-Mean-Square Error in Log-Space vs. Number of Relaxation Frequencies

In this section, we explore the minimum-mean-square error (MSE) of an unbiased estimator of the relaxation frequencies in log-space as a function of the number of relaxations for a

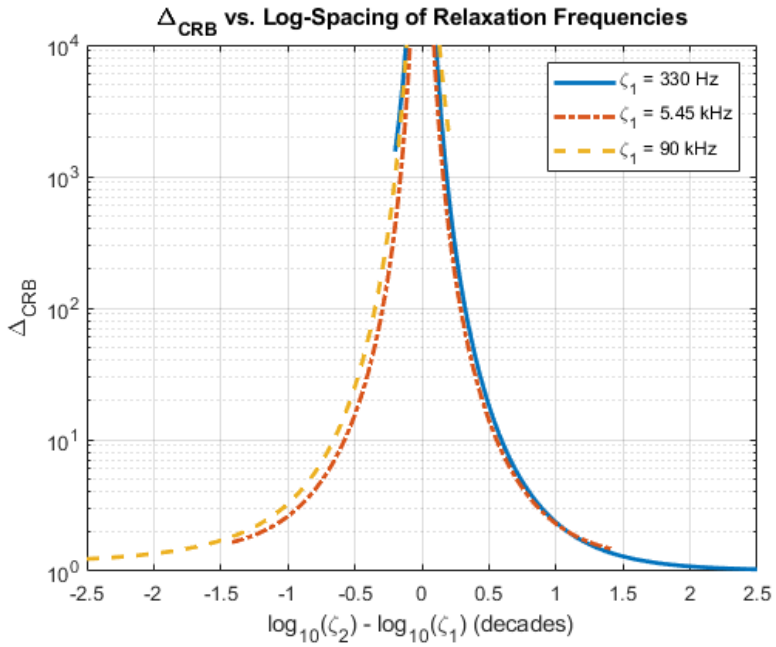

Figure 7.2: The factor increase, Δ_{CRB}, in $\mathrm{CRB}(\zeta_1)$ due to the presence of a second relaxation frequency ζ_2 as a function of the spacing between the relaxation frequencies for different, fixed values of ζ_1.

given rank-one target. The MSE of this estimator in log-space, $\mathrm{MSE}_{\hat{\boldsymbol{\zeta}}}$, is defined as

$$\begin{aligned}\mathrm{MSE}_{\hat{\boldsymbol{\zeta}}} &= E\left\{\left\|\log_{10}(\hat{\boldsymbol{\zeta}}) - \log_{10}(\boldsymbol{\zeta})\right\|_2^2\right\} = \sum_p E\left(\log_{10}(\hat{\zeta}_p) - \log_{10}(\zeta_p)\right)^2 \\ &= \sum_p \mathrm{Var}(\log_{10}(\hat{\zeta}_p))\end{aligned} \tag{7.12}$$

where $E(\cdot)$ is the expectation operator. The lower bound on the MSE of an unbiased estimator in log-space is given by

$$\mathrm{MSE}_{\hat{\boldsymbol{\zeta}},\min} = \sum_p \mathrm{CRB}(\log_{10}(\zeta_p)) = \mathrm{Tr}\{\boldsymbol{C}_{CR}(\log_{10}(\boldsymbol{\zeta}))\} \tag{7.13}$$

where $\mathrm{Tr}(\cdot)$ is the trace operator. The expression in (7.13) results from the fact that $E\{(\hat{\zeta}_p - \zeta_p)^2\} = \mathrm{Var}(\hat{\zeta}_p)$ for unbiased estimators of $\boldsymbol{\zeta}$, and by definition $\mathrm{Var}_{\min}(\hat{\zeta}_p) = \mathrm{CRB}(\zeta_p)$.

Instead of calculating $\boldsymbol{C}_{CR}(\log_{10}(\boldsymbol{\zeta}))$ directly, it is easier to calculate $\boldsymbol{C}_{CR}(\boldsymbol{\zeta})$ and use the transformation property of the CRB to compute $\boldsymbol{C}_{CR}(\log_{10}(\boldsymbol{\zeta}))$. The entries in $\boldsymbol{C}_{CR}(\log_{10}(\boldsymbol{\zeta}))$

are related to $\boldsymbol{C}_{CR}(\boldsymbol{\zeta})$ through

$$\boldsymbol{C}_{CR}(\log_{10}(\boldsymbol{\zeta})) = \left(\frac{\partial \boldsymbol{g}(\boldsymbol{\zeta})}{\partial \boldsymbol{\zeta}}\right) \boldsymbol{C}_{CR}(\boldsymbol{\zeta}) \left(\frac{\partial \boldsymbol{g}(\boldsymbol{\zeta})}{\partial \boldsymbol{\zeta}}\right)^T \tag{7.14}$$

where $\boldsymbol{g}(\boldsymbol{\zeta}) = [\log_{10}(\zeta_1), \log_{10}(\zeta_2), ..., \log_{10}(\zeta_P)]^T$. $\frac{\partial \boldsymbol{g}(\boldsymbol{\zeta})}{\partial \boldsymbol{\zeta}} \in \mathbb{R}^{P \times P}$ is diagonal matrix, where the ij-th entry is the derivative of the i-th entry of $\boldsymbol{g}$ with respect to ζ_j. The derivatives will only be nonzero when $i = j$, which is why it is diagonal. The ii-th entry is expressed as

$$\left[\frac{\partial \boldsymbol{g}(\boldsymbol{\zeta})}{\partial \boldsymbol{\zeta}}\right]_{ii} = \frac{1}{\zeta_i \ln 10} \tag{7.15}$$

This relation is the same as what is shown in (5.14). Substituting (7.14) into (7.13) yields

$$\text{MSE}_{\hat{\boldsymbol{\zeta}},\text{min}} = \text{Tr}\left\{\left(\frac{\partial \boldsymbol{g}(\boldsymbol{\zeta})}{\partial \boldsymbol{\zeta}}\right) \boldsymbol{C}_{CR}(\boldsymbol{\zeta}) \left(\frac{\partial \boldsymbol{g}(\boldsymbol{\zeta})}{\partial \boldsymbol{\zeta}}\right)^T\right\} \tag{7.16}$$

We note that an excellent approximation to $\text{MSE}_{\hat{\boldsymbol{\zeta}},\text{min}}$ could also be calculated by using $\boldsymbol{C}_{ACR}(\boldsymbol{\zeta})$ instead of $\boldsymbol{C}_{CR}(\boldsymbol{\zeta})$ in (7.16), which is what we use for the subsequent Monte Carlo analysis.

To validate the expression in (7.16), we perform Monte Carlo analysis. We simulate rank-one targets with a varying number of relaxation frequencies between 2 and 7. We force the relaxations for each frequency model to be evenly separated in log-space with the maximum spacing between them. We also require that all the relaxations lie within the system bandwidth, which is 2.4359 decades wide. For example, when two relaxation frequencies are modeled, the two modeled relaxations are $\zeta_1 = 330$ Hz, and $\zeta_2 = 90030$ Hz, corresponding to the edges of the system bandwidth. When three relaxation frequencies are modeled, the relaxations are $\zeta_1 = 330$ Hz, $\zeta_2 = 5450$ Hz, and $\zeta_3 = 90030$ Hz. In log-space, these frequencies have the same $2.4359/2 = 1.2179$ decade spacing between them. Additionally, we ensure each relaxation has the same SNR as defined in (5.13).

For each frequency model, we simulate 1000 measurements at 60 dB SNR_{ζ_p} for each

relaxation frequency according to the factored frequency model in (5.8) and estimate the frequencies and amplitudes for each measurement using the MLE in (5.9). For each trial, we convert the relaxation estimates to log-space and compute the sample variance across the trials. We then sum the sample variances to arrive at $\text{MSE}_{\hat{\boldsymbol{\zeta}}}$ for a given frequency model and then divide by the number of relaxation frequencies in the model. This process is repeated for each of the different frequency models. We show the root-mean-square error (RMSE) per relaxation for each frequency model. We note that we use $\boldsymbol{C}_{ACR}(\boldsymbol{\zeta})$ for the analytic calculations shown in Figure 7.3. We also show the results for multiple values of SNR_{ζ_p}.

We observe excellent agreement between the Monte Carlo results and the analytic bound corresponding to 60 dB SNR_{ζ_p} in Figure 7.3, which gives us confidence that the expression in (7.16) is correct. Additionally, we observe minimal increase in the minimum RMSE per relaxation frequency when the number of relaxation frequencies is increased from two to three. When three relaxations are present, the spacing between them in log-space is approximately 1.2 decades. We show in Section 7.1.2 that there is only a small impact on the ACRBs of the relaxation frequencies when two relaxations are spaced greater than a decade apart, which seems consistent with the three relaxation case as well. Beyond three relaxation frequencies, we observe approximately one order of magnitude increase in the RMSE per relaxation frequency for each additional two relaxation frequencies. This increase is predominantly due to the decreasing separation between relaxation frequencies as the number of modeled frequencies increases.

This curve can be extended to an arbitrary SNR, so long as the SNR for each relaxation is the same. Changing the SNR shifts the curve up or down by a proportional amount, as can be seen by comparing the three analytic curves. For example, we observe that decreasing the SNR by 20 dB, or a factor of 100, causes the curve to shift up by a factor of $\sqrt{100}$.

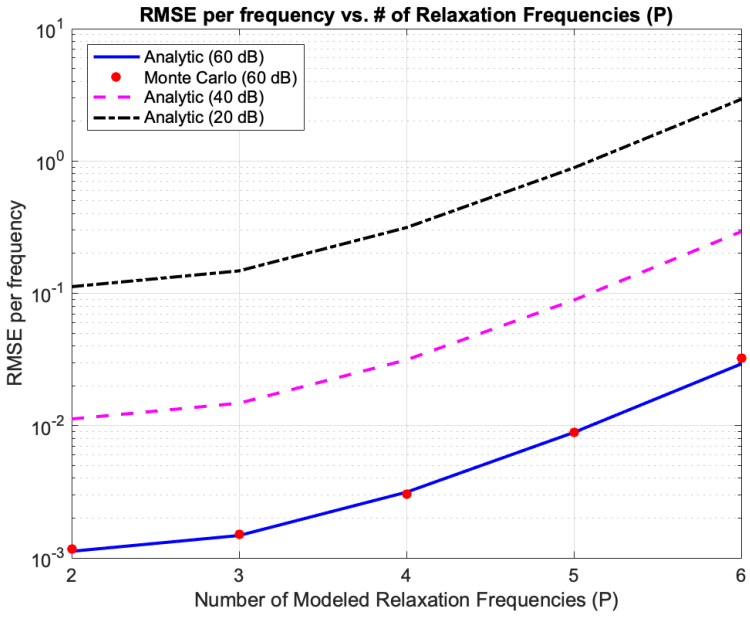

Figure 7.3: Comparison of RMSE per relaxation frequency calculated from (7.16) (solid blue line) to Monte Carlo analysis (red circle markers) for the $\text{SNR}_{\zeta_p} = 60$ dB case. Analytic bounds for $\text{SNR}_{\zeta_p} = 20$ dB (dot-dash line) and $\text{SNR}_{\zeta_p} = 40$ dB (dashed line) are also shown.

7.2 Spatial Parameter Analysis

This section contains four sub-sections where each sub-section discusses a different type of analysis related to the spatial unknowns. In Section 7.2.1, we explore the ACRBs of the factored tensor and target position as a function of the target depth. As such, when we refer to the tensor in this section, we are referring to $\boldsymbol{t}_f$ in the factored spatial model. We show that a loss in SNR as the target depth increases is the primary driver of worsening performance in the ACRB sense. In Section 7.2.2, we explore the ACRB of the target depth for a dipole target as a function of the dipole's orientation. We show that the change in the spatial response as the target rotates as well as the change in SNR both impact the lower bound for estimating depth. In Section 7.2.3, we explore the ACRBs of the spatial parameters for different model assumptions. We show that estimating target depth is difficult because changes in the target depth look similar to changes in the tensor strength. We also demonstrate for a notional example of a z-directed dipole that knowledge of the

target's location, which could be provided by a ground penetrating radar (GPR) in a fused GPR-EMI system, improves the lower bound on the t_{zz} component of the tensor by an order of magnitude in the standard deviation sense. Lastly, in Section 7.2.4, we demonstrate how the ACRBs can be calculated for a time-domain system for detecting and identifying buried objects called TEMTADS.

For this section, SNR is defined as SNR = $\|\boldsymbol{H}_s(\boldsymbol{l}_t)\boldsymbol{t}_f\|_2^2/\sigma_n^2$.

7.2.1 ACRBs vs. Depth

In this section, we are interested in studying how the ACRBs change as a function of depth. As an example, we compute the ACRBs of a z-directed dipole target for a fixed SNR of 40 dB and for a fixed noise variance as a function of depth. The SNR at the initial depth for the fixed noise variance case is 40 dB and decreases as depth increases. The bounds are shown in Figure 7.4.

The main observation from Figure 7.4 is that decreasing SNR is the primary driver of the ACRBs as depth increases. This can be seen by comparing the fixed SNR case (left column of Figure 7.4) to the fixed noise variance case (right column of Figure 7.4). When noise variance is fixed, we observe that for all parameters the $\sqrt{\text{ACRB}}$ increases by at least 2 orders of magnitude in the best case, and 3 orders of magnitude in the worst case. In the fixed SNR case, the $\sqrt{\text{ACRB}}$ for all parameters changes by less than half an order of magnitude, suggesting that the spatial response of the target across the sensor measurements is relatively constant for the range of depths considered, compared to the loss in SNR. In fact, the signal power falls off at a rate of approximately R^6, where R is the distance between the sensor and the target. This result is one of the reasons why maximizing sensitivity is important to sensor designers, as it allows for better performance against deeper targets.

The fixed SNR graphs in Figure 7.4 can also be used to quantify the lower bound on the performance of unbiased estimators. For example, if an SNR of 40 dB can be achieved,

the target location can be estimated within 1 cm of the true value in each dimension most of the time, and within 0.1 of the true value for each tensor component for depths greater than 15 cm.

These results can be extended to an arbitrary SNR using (7.17).

$$\sqrt{\text{ACRB}_{\text{new}}(\theta_i)} = 10^{\frac{40-\text{SNR}_{\text{dB}}}{20}} \sqrt{\text{ACRB}_{40}(\theta_i)} \tag{7.17}$$

where the term $\sqrt{\text{ACRB}_{40}(\theta_i)}$ corresponds to a point on the fixed SNR curves in Figure 7.4 for parameter θ_i. As an example, to convert the bound for y_t at 25 cm to an SNR of 20 dB, we compute the scale factor of 10 multiplied by the value of 1 cm from the curve in Figure 7.4c to arrive at a new bound of 10 cm.

7.2.2 ACRBs vs. Target Rotation

In this section, we explore $\text{ACRB}(z_t)$ as a function of the target's orientation for an x-directed dipole target. The expression for the rotated tensor in matrix form, $\tilde{\boldsymbol{T}}_{rot}$, as a function of the initial tensor $\tilde{\boldsymbol{t}} = [1, 0, 0, 0, 0, 0]^T$ is shown in (7.18).

$$\tilde{\boldsymbol{T}}_{rot} = \boldsymbol{R}^T(\alpha, \beta, \gamma) \begin{bmatrix} 1 & 0 & 0 \\ 0 & 0 & 0 \\ 0 & 0 & 0 \end{bmatrix} \boldsymbol{R}(\alpha, \beta, \gamma) \tag{7.18}$$

In (7.18), α, β, and γ are the yaw, pitch, and roll rotation angles, respectively, which are the same definitions as in (2.35). The rotation axes are shown in Figure 2.1. In performing the rotations, the yaw rotation is performed first, followed by pitch, and then roll.

By expressing the tensor components as a function of angle, the ACRB of the target depth for a single dipole target can be visualized as a function of two rotation angles, rather than the six explicit values of the tensor.

We demonstrate this by considering the unrotated target to be an x-directed dipole at a

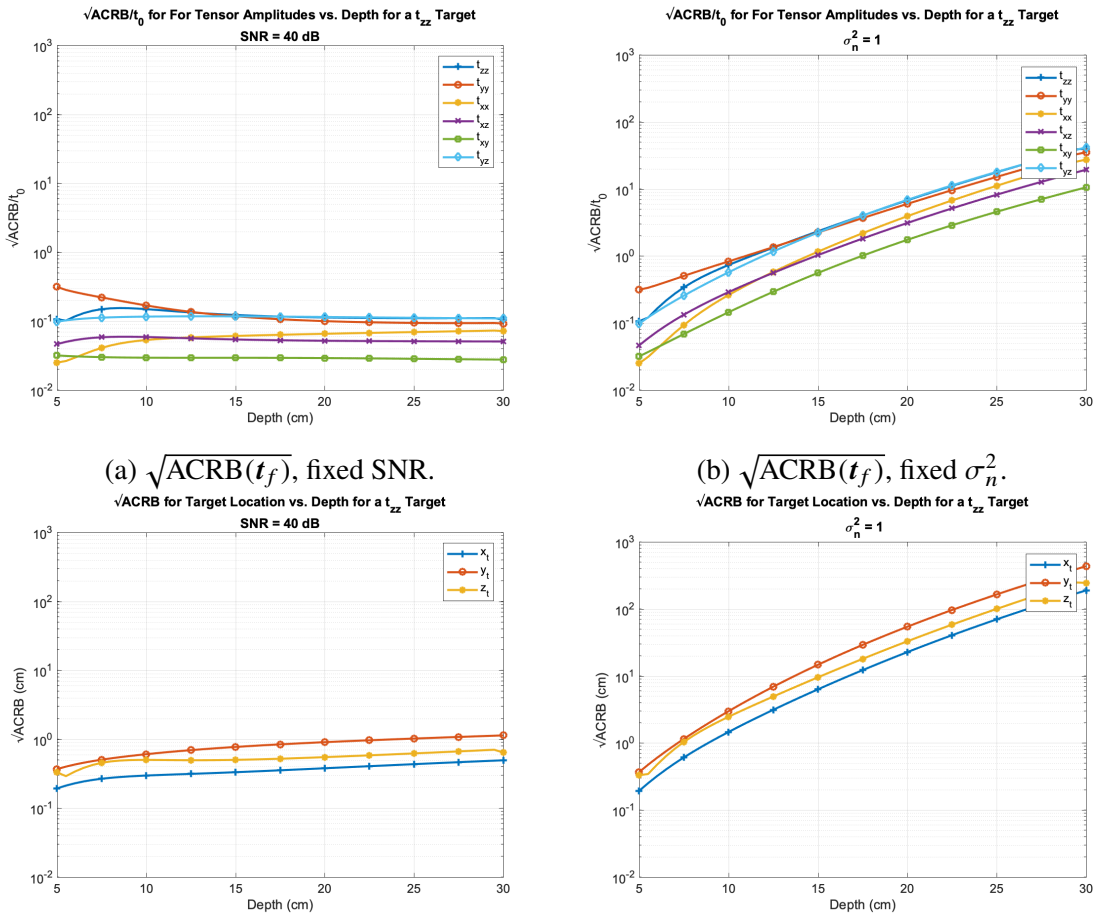

(a) $\sqrt{\text{ACRB}(\boldsymbol{t}_f)}$, fixed SNR.

(b) $\sqrt{\text{ACRB}(\boldsymbol{t}_f)}$, fixed σ_n^2.

(c) $\sqrt{\text{ACRB}(\boldsymbol{l}_t)}$, fixed SNR.

(d) $\sqrt{\text{ACRB}(\boldsymbol{l}_t)}$, fixed σ_n^2.

Figure 7.4: $\sqrt{\text{ACRB}}$ for location and tensor components for a fixed SNR (left column) and a fixed noise variance (right column).

depth of 7 cm with an initial SNR of 32 dB. Because of the symmetry of this target, the rotation space is completely described by the yaw and pitch rotation angles between 0° and 90°. The $\sqrt{\text{ACRB}}$ of the target depth and the corresponding SNR at each rotation angle are shown as contours in Figure 7.5a and Figure 7.5b, respectively. In these figures, the lower right corner rotation corresponds to a z-directed dipole and the entire upper x-axis rotation corresponds to a y-directed dipole.

In examining Figure 7.5a, we observe two trends: the SNR increases as the target pitch angle increases, and decreases as the yaw angle increases. This might lead one to suspect that the ACRB should degrade as the target rotates in yaw and improve as the target rotates

in pitch. However, this is only partially true. From Figure 7.5b, we observe that the ACRB certainly worsens as the yaw angle increases. Rotating the target in yaw increases the t_{yy} component of the target, which the GT sensor is blind to, resulting in a significant decrease in SNR. However, we observe the ACRB is minimally changed as the pitch angle increases, despite the fact that the SNR increases. We attribute this to the fact that the coupling between the t_{zz} and z_t components is stronger than the t_{xx} and z_t components, which increases the corresponding off-diagonal entry of the FIM. As the target rotates in pitch, the t_{zz} component increases and so does the coupling, which appears to nullify the benefit of a higher SNR.

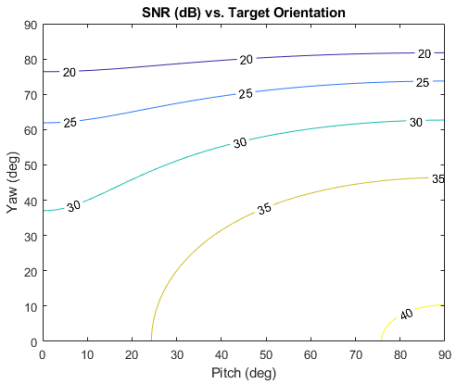

(a) SNR of an x-directed dipole target at various yaw and pitch rotations.

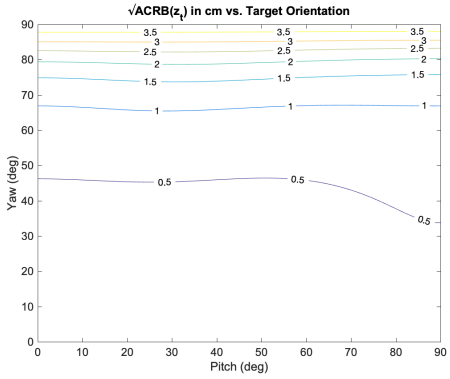

(b) $\sqrt{\text{ACRB}}$ of z_t parameter for an x-directed dipole target at various yaw and pitch rotations.

7.2.3 ACRBs vs. SNR for Different Model Assumptions

In this section, we explore how the FIM and ACRB change with different levels of a priori information about a target. We consider four scenarios, each corresponding to a different model assumption: *Scenario 1*: the target location is known, but the tensor is unknown; *Scenario 2*: the tensor is known, but the location is unknown; *Scenario 3*: the target type is known, but the amplitude of the target and location are unknown; *Scenario 4*: the case where all parameters are unknown.

We begin this section by discussing the form of the FIM for each scenario. We consider

two targets, an x-directed dipole and a z-directed dipole, to understand the relationship between the target parameters and how they affect the FIMs. In generating the FIMs (and later the ACRBs), we use the system and measurement parameters of the GT frequency-domain EMI system in Section 2.6.

After the discussion of the FIMs, the ACRBs for the unknown parameters are shown for the different scenarios, along with Monte Carlo results. For the Monte Carlo (MC) trials, 200 realizations are generated at each SNR, and estimates of the unknown target parameters are computed using the maximum likelihood estimator in (5.10). When certain parameters are known, they are dropped from the minimization statement and replaced with the true value. We perform the MC analysis for only three of the scenarios: *Scenario 1*: the target location is known, but the tensor is unknown; *Scenario 2:* the tensor is known, but the location is unknown; *Scenario 4:* all parameters unknown.

Scenario 1 FIM Analysis: Known Location, Unknown Tensor

When the target location is known and the target tensor is unknown, the FIM takes the form

$$\boldsymbol{I}(\boldsymbol{t}) = \frac{2}{\sigma_n^2}\boldsymbol{H}_s^T\boldsymbol{H}_s \tag{7.19}$$

where $\boldsymbol{H}_s$ is the magnetic scene due to a target at the known location. For a given target location, the ACRB depends only on the measurement scan and the sensor implicitly through $\boldsymbol{H}_s$; it is not a function of the target type or the tensor.

The sensitivity of EMI measurements to the unknown parameters can be explored through an image visualization of the 6×6 FIM. A grayscale image of the FIM for a target located at a depth of 7 cm is shown in Figure 7.6. Darker entries indicate larger values, with numerical values given for the actual values of each entry in the FIM. From the figure, we observe that the Georgia Tech sensor is most sensitive to the t_{zz} and t_{xx} tensor components. However, this sensitivity is only partially indicative of our ability to estimate those parameters. As we show in *Scenario 4*, when all the parameters unknown, coupling between the

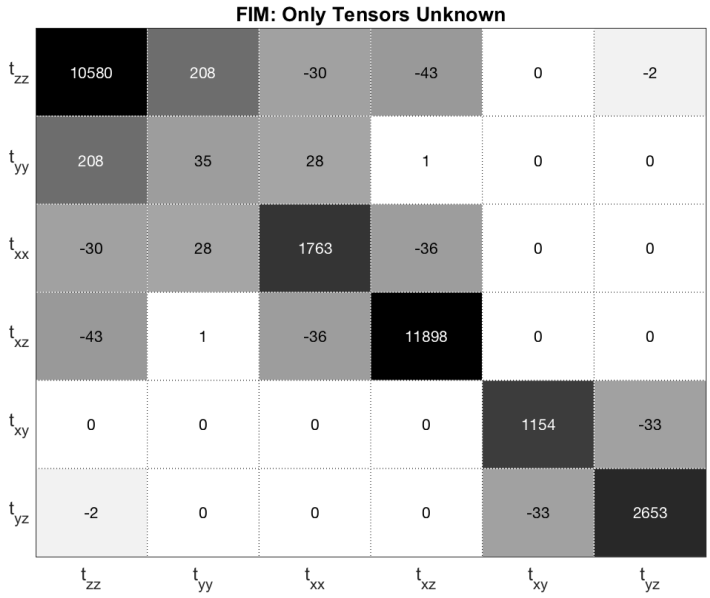

Figure 7.6: FIM when target location is known. The number in each box is the actual value of the corresponding entry in the FIM. Darker boxes have larger values.

unknown parameters causes large off-diagonal terms in the FIM which negatively impact the lower bound on estimation performance. We also observe that the structure of the FIM in Figure 7.6 is nearly ideal in that it has large diagonal entries and relatively small cross-term entries. The sensor is notably insensitive to the t_{yy} tensor component, which is the (2,2) entry. This is attributable to the orientation of the receive coil, which cannot sense the y-component of the magnetic field very well. If the sensor were rotated 90 degrees, it would be blind to the x-component of the magnetic field and consequently the t_{xx} tensor component of the FIM would be small. One way to mitigate these blind magnetic field components without changing the sensor design is to rotate the sensor while it is scanned – a natural motion when scanning a handheld sensor back and forth. This would allow all components of the magnetic field to be captured in a given scan.

Scenario 2: Known Tensor, Unknown Location

In this case, we assume the target tensor is known and the target location is unknown, so the FIM is

$$\boldsymbol{I}(\boldsymbol{l}_t) = \frac{2}{\sigma_n^2}\boldsymbol{D}_{\boldsymbol{l}_t}^T\boldsymbol{D}_{\boldsymbol{l}_t} \tag{7.20}$$

Image plots of the FIM for a $t_{xx} = 1$ and $t_{zz} = 1$ target at a depth of 7 cm are shown in Figure 7.7a and Figure 7.7b, respectively. Both figures show the strongest sensitivity to depth, followed by the x-position and y-position of the target, respectively. This suggests that the depth estimate is better than the x- and y-components, which is true for the problem as defined. The reason for this is that the amplitude of the target is known which when combined with the depth sensitivity of the sensor gives a very good depth estimate. Unfortunately, the amplitude of the target is not usually known in practical applications. The effects of an unknown amplitude are addressed in *Scenario 3*. Lastly, it is worth noting that the structures of the FIMs are ideal in that the only nonzero terms are on the diagonal.

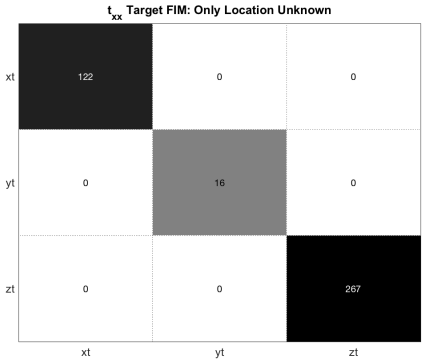

(a) FIM for x-directed dipole target.

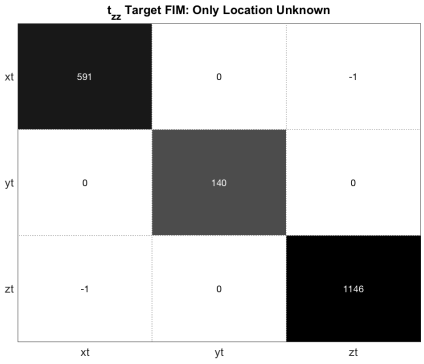

(b) FIM for z-directed dipole target.

Figure 7.7: 3×3 FIMs when only location is unknown. The (3,3) entry is the largest.

Scenario 3: Known Target Type, Unknown Amplitude and Location

In this scenario, we analyze the FIMs for the case where we know the target type but not its amplitude or location. In other words, we know that the target is either a t_{xx} or a t_{zz}

target, but we do not know how strong the target is. This a priori condition allows us to demonstrate the coupling between tensor component and target depth while maintaining a tractable number of unknown parameters. For the two target types considered, there are four unknown parameters – either t_{xx} or t_{zz}, and the target location (x_t, y_t, z_t). The 4×4 FIM under these conditions is shown in (7.21), where t_i is either t_{xx} or t_{zz}.

$$\boldsymbol{I}(\boldsymbol{l}_t, t_i) = \frac{2}{\sigma_n^2} \begin{bmatrix} \boldsymbol{d}_{t_i}^T \boldsymbol{d}_{t_i} & \boldsymbol{d}_{t_i}^T \boldsymbol{D}_{\boldsymbol{l}_t} \\ \\ \boldsymbol{D}_{\boldsymbol{l}_t}^T \boldsymbol{d}_{t_i} & \boldsymbol{D}_{\boldsymbol{l}_t}^T \boldsymbol{D}_{\boldsymbol{l}_t} \end{bmatrix} \tag{7.21}$$

Image plots of the FIMs for the t_{xx} and t_{zz} targets at a depth of 7 cm are shown in Figure 7.8a and Figure 7.8b, respectively. We see from these images that the FIM is no longer

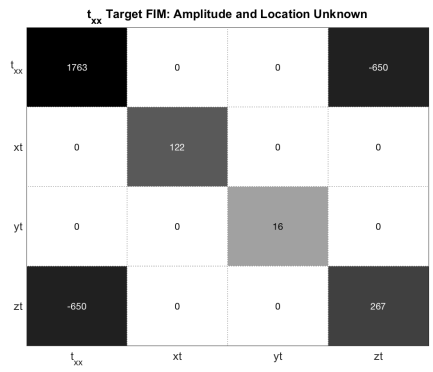

(a) FIM for x-directed dipole target.

(b) FIM for z-directed dipole target.

Figure 7.8: FIMs for x-directed and z-directed dipole targets when the location and amplitude are assumed unknown.

diagonal. There are large off-diagonal terms in the lower left and upper right corner of the FIMs, indicating a strong coupling between the tensor component and depth. This large off-diagonal term indicates that changes in depth and the tensor component cause similar changes in the measurement response. The coupling between these two parameters explains why it is difficult to differentiate a shallow, weak target from a strong, deep target.

Scenario 4: All Parameters Unknown

When all parameters are unknown, the FIM takes the form in (6.15). Since there are 9 unknowns, the FIM is 9×9. A visualization of the FIM for a $t_{xx} = 1$ target and a $t_{zz} = 1$ target is shown in Figure 7.9a and Figure 7.9b, respectively. When the additional parameters are included in the FIM for a t_{zz} target, we observe that there is a large t_{xz} - x_t and t_{zz} - z_t cross-term which degrades our ability to estimate their respective terms. The t_{xx} target has significant cross-terms for t_{zz} - z_t, t_{xx} - z_t, and t_{xz} - x_t. However, these cross-terms are smaller because the GT EMI sensor is more sensitive to t_{zz} targets than to t_{xx} targets.

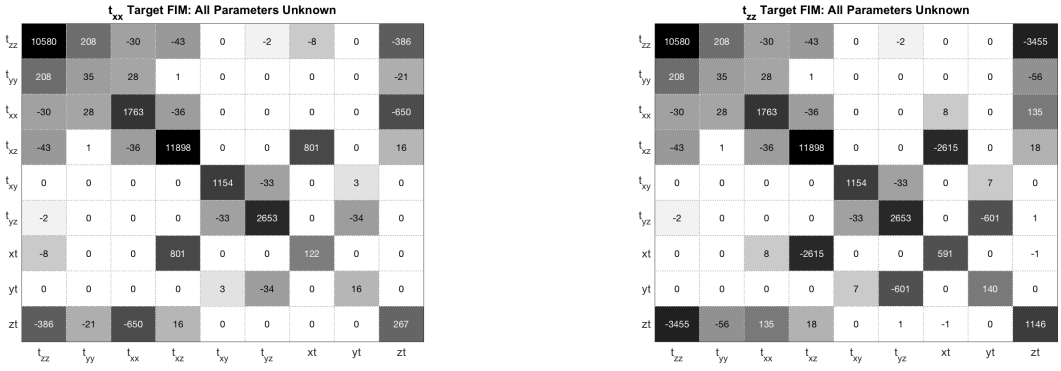

(a) FIM for x-directed dipole target.

(b) FIM for z-directed dipole target.

Figure 7.9: 9×9 FIMs for (a) x-directed dipole and (b) z-directed dipole when all parameters are unknown.

ACRBs vs. SNR for Location Parameters

In the previous four scenarios, we explored the different measurement models from the perspective of the FIM. Now, we compute the ACRBs for the location parameters for the different scenarios to understand how they change due to the different model assumptions. We consider the measurement of a z-directed dipole target located at $\boldsymbol{l}_t = (0, 0, 7)$ cm using the previously described GT sensor and measurement scan. We show the ACRBs for the different model assumptions (excluding Scenario 2 where location is known) along with the corresponding Monte Carlo results for the x_t, y_t, and z_t parameters vs. SNR in Figure

7.10a, Figure 7.10b, and Figure 7.10c, respectively.

The bounds for the amplitude and location unknown case match the location unknown case for the x_t and y_t, which suggests they are not impacted by not knowing the target strength. This is because there is no cross-term between the t_{zz} component of the tensor and the x_t and y_t parameters which is shown in Figure 7.8. This implies that changes in x_t and y_t position of the target are uniquely identifiable from changes in the target amplitude. However, the $\sqrt{\text{ACRB}}$ for target depth worsens by almost an order of magnitude when the amplitude of the target is not known due to the coupling between depth and the tensor component as is discussed in Section 7.2.3. When the entire target tensor is unknown, the $\sqrt{\text{ACRB}}$ worsens by approximately half an order of magnitude for the x_t and y_t positions, and less than half an order of magnitude for depth. Again, this is due to coupling between the tensor components and each of the location parameters. Lastly, we observe that the Monte Carlo results show good agreement with the derived ACRBs.

ACRBs vs. SNR for Nonzero Tensor Component

Like the previous section, we consider the measurement of a z-directed dipole target located at $\boldsymbol{l}_t = (0, 0, 7)$ cm using the previously described GT sensor and measurement scan. In this section, however, we focus on the change in the ACRB of the nonzero tensor component under the different model scenarios. We show the ACRB and the corresponding Monte Carlo results for the t_{zz} component of the tensor in Figure 7.11 for the different model scenarios. We only show this tensor component to limit the number of figures and because it exemplifies how the ACRBs for the tensor components change with different levels of a priori information.

We observe that knowledge of the target location improves the $\sqrt{\text{ACRB}}$ by approximately one order of magnitude for the t_{zz} tensor component. This improvement in the ACRB when the location is known bodes well for the fusion of ground penetrating radar (GPR) and EMI systems, as GPR is good at estimating target location but does not lend

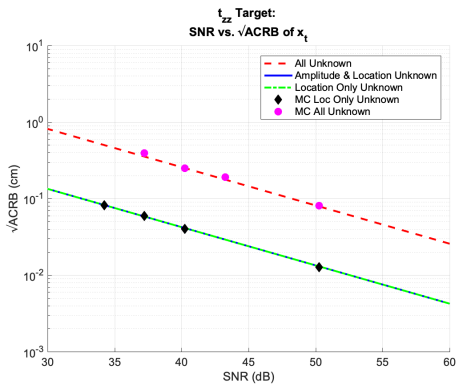

(a) $\sqrt{\text{ACRB}}$ vs. SNR for x_t coordinate.

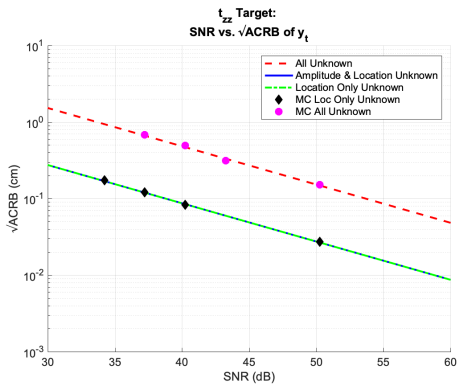

(b) $\sqrt{\text{ACRB}}$ vs. SNR for y_t coordinate.

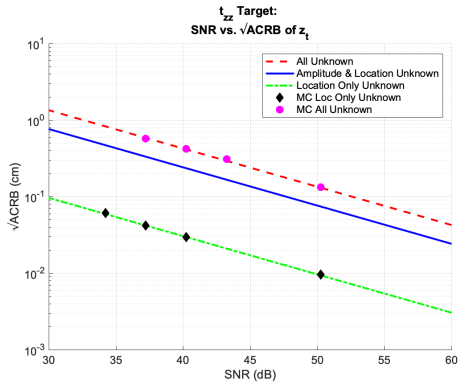

(c) $\sqrt{\text{ACRB}}$ vs. SNR for z_t coordinate.

Figure 7.10: $\sqrt{\text{ACRB}}$ for location parameters (x_t, y_t, z_t) for a z-directed dipole target compared to Monte Carlo simulations. In 7.10a and 7.10b, the location only unknown line (dashed green) and the amplitude and location unknown line (solid blue) are overlayed.

itself well to classification. We also see that when all of the parameters are unknown, there is a further increase in the ACRB as more of the unknown parameters couple with the t_{zz} component of the tensor components as shown in Figure 7.9.

7.2.4 Application to Time-Domain EMI System

In this section, we compute the ACRBs of the unknown target parameters as a function of depth for the TEMTADS array [15]. The TEMTADS array differs significantly from the GT sensor in that it is a fixed array of sensors that operates in a multi-static configuration in the time domain. It is designed to detect both shallow targets ($\leq$ 30 cm) and deeply buried UXOs ($>$ 30 cm), while the handheld GT sensor is designed to only detect shallow targets

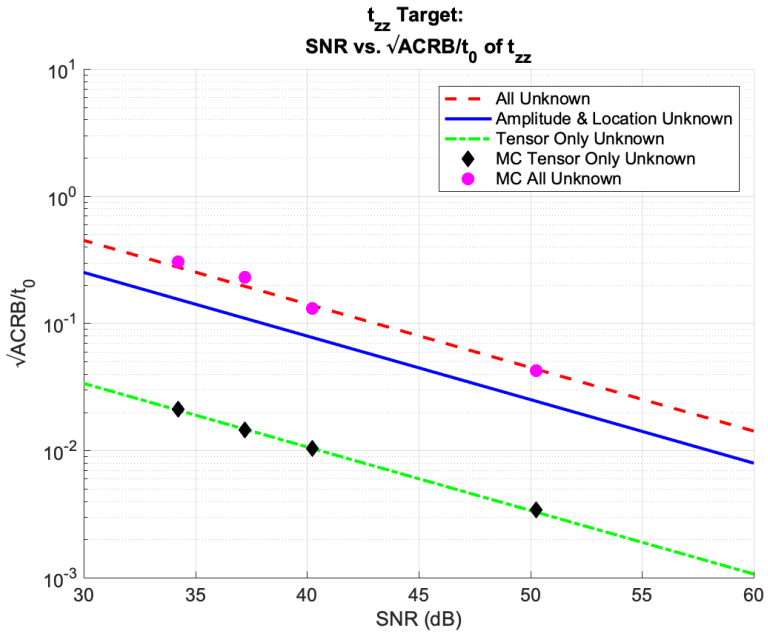

Figure 7.11: $\sqrt{\text{ACRB}}/t_0$ for t_{zz} component of tensor for a z-directed dipole target.

($\leq$ 30 cm).

The TEMTADS array consists of 25 co-located transmit and receive pairs arranged in a fixed 5×5 grid configuration [15]. The 25 transmitters transmit one at a time in a sequence. The received signal is measured on all 25 receive sensors for each transmission resulting in 625 measurements. Each measurement has 123 time gates, and thus the measurement matrix is $\boldsymbol{M} \in \mathbb{C}^{123\times625}$. When this array is used in practice, the operator attempts to center the array on the initial detection. As such, we assume for this analysis that the target is centered under the array.

We plot the ACRBs as a function of depth for a *fixed* SNR[2] for the tensor and the target location in Figure 7.12 for a z-directed dipole target. For both the tensor components and the location parameters, the ACRB improves with depth up to depths of 50 cm, where the trend reverses and the ACRBs begin to worsen as depths increase past 50 cm.

The relatively poor performance at shallow depths when SNR is fixed is due to the fact that when the target is close to the array, the magnetic field is spatially concentrated under

[2]A variation of these figures appears in [37], where we define SNR in that paper as SNR $= 1/\sigma_n^2 \cdot \max\left(|\boldsymbol{H}_s(\boldsymbol{l}_t)t|\right)^2$.

the receive sensor directly above the target, with very little magnetic energy reaching the other receive sensors. As depth increases, the magnetic field spreads out over the entire array which provides spatial diversity in the measurement and thus an improved ACRB. If these ACRBs were plotted for a fixed noise variance as a function of depth, it is expected that the estimation performance at shallower depths would be better due to higher SNR, as is pointed out for the GT sensor in Figure 7.4. For this particular TEMTADS scenario, we see from Figure 7.12b that at 40 dB SNR, the target must be at least 25 centimeters deep to be able to estimate all the target location parameters within 2 cm the majority of the time. The expression in (7.17) can also be used for this array to convert the results to an arbitrary SNR.

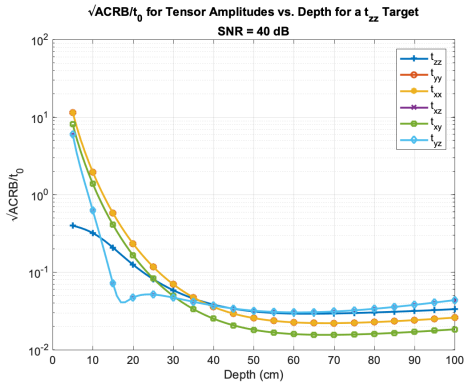

(a) $\sqrt{\text{ACRB}}$ for tensor components vs. depth. Due to the symmetry of the sensor and array configuration, the t_{xx} and t_{yy} curves overlap, as do the t_{xz} and t_{yz} curves.

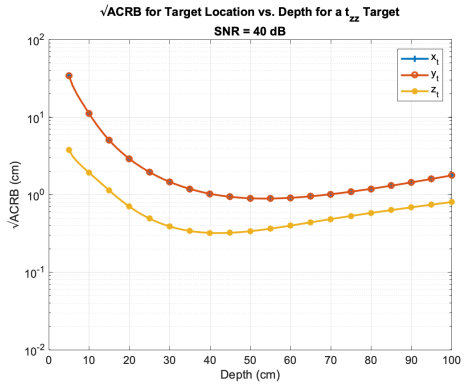

(b) $\sqrt{\text{ACRB}}$ for target location vs. depth. x_t and y_t curves overlap due to the symmetry of the sensor and array configuration.

Figure 7.12: $\sqrt{\text{ACRB}}$ of (a) six tensor components (scaled by t_0) and (b) the x-y-z location for TEMTADs array measurement of a z-directed dipole.

CHAPTER 8

CRAMER-RAO LOWER BOUNDS FOR TARGETS OF ARBITRARY RANK FOR THE SUM OF TENSORS MODEL

In this chapter, we derive the CRBs of the unknown parameters associated with measurements of an arbitrary target in the presence of complex white Gaussian noise using the SoT form of the signal model. We begin the chapter by discussing a few model preliminaries necessary before deriving the CRBs. Subsequently, we work through the derivation of the CRBs for the target tensors, relaxation frequencies, their corresponding amplitudes, as well as the target location. We then validate the bounds for two example targets. This chapter is an extension of the bounds derived in Chapter 4.

8.1 Preliminaries

As mentioned previously, the choice of basis in (2.15) is arbitrary when representing a target. However, it cannot be arbitrary in the context of the CRB because all of the unknown parameters in the model must be identifiable; otherwise, the FIM is singular. This consideration can be illustrated for the signal model of the wire loop target. By examining the relaxation frequency response together with the tensor in (2.22), one can see that a new parameter $\tilde{\boldsymbol{t}}_{new} = \alpha_1 \cdot \tilde{\boldsymbol{t}}_1$ could equivalently be defined in the SoT model to reduce the number of unknowns by 1.

This motivates the need for a basis that can express $\boldsymbol{T}_p$ using the fewest number of model unknowns possible. The basis we choose for this chapter that meets this requirement is defined such that the largest α_{pk} term for each k is embedded in the corresponding $\tilde{\boldsymbol{T}}_k$. Under this definition, the magnitude of the α_{pk} terms are all less than or equal to 1, and the embedded amplitude is dropped from $\boldsymbol{f}_k(\boldsymbol{\omega})$. If the amplitudes are defined in this manner, then each basis tensor $\tilde{\boldsymbol{T}}_k$ represents both an orientation and an amplitude. Under this basis

definition, the basis tensors $\tilde{\boldsymbol{T}}_k$ are equivalent to the tensor amplitudes in [24].

A few examples are necessary to make this basis definition more clear. The tensor for the copper loop target is $\tilde{\boldsymbol{t}}_1 = [0, 0, \alpha_1, 0, 0, 0]^T$, and the α_1 term is dropped from the relaxation frequency response. Subsequently, there are 10 unknown parameters in this model: 3 for the target location, 6 for the tensor, and 1 for the relaxation frequency. For a target consisting of co-located orthogonal copper loops with different relaxation frequencies, the tensors are $\tilde{\boldsymbol{t}}_1 = [\alpha_1, 0, 0, 0, 0, 0]^T$ and $\tilde{\boldsymbol{t}}_1 = [0, 0, \alpha_2, 0, 0, 0]^T$. There are no α terms in the relaxation frequency responses. In this model, there are 17 unknown parameters: 3 for the target location, 12 for the tensors (6 for each), and 2 relaxation frequencies. As a final example, we consider the co-axial loops target. Under this basis definition, the tensor is $\tilde{\boldsymbol{t}}_1 = [\alpha_1, 0, 0, 0, 0, 0]^T$, and the frequency response is $\boldsymbol{f}_1(\boldsymbol{\omega}) = -\dfrac{j\boldsymbol{\omega}/\zeta_1}{1 + j\boldsymbol{\omega}/\zeta_1} - \alpha_2 \dfrac{j\boldsymbol{\omega}/\zeta_2}{1 + j\boldsymbol{\omega}/\zeta_2}$. There are a total of 12 unknowns in this model: 3 for target location, 2 for relaxation frequency, 1 for the amplitude, and 6 for the tensor.

The choice of which amplitude is embedded will change the CRBs of the basis tensors and the amplitudes. However, the parameters that we are really interested in which are the products of these quantities, are unchanged by this choice.

8.2 Derivation

The measurement model for an arbitrary magnetic target is

$$\boldsymbol{m}(\boldsymbol{\omega}, \boldsymbol{l}_{TR}) = \underbrace{\sum_k \boldsymbol{H}_s(\boldsymbol{l}_t)\tilde{\boldsymbol{t}}_k \otimes \boldsymbol{f}_k(\boldsymbol{\omega})}_{\boldsymbol{r}(\boldsymbol{\theta})} + \boldsymbol{n} \tag{8.1}$$

where it is assumed that $\boldsymbol{n} \sim CN(\boldsymbol{0}, \sigma_n^2 \boldsymbol{I})$, and $\boldsymbol{r}(\boldsymbol{\theta})$ is a compact form of the signal model parameterized by the unknowns in $\boldsymbol{\theta} = \left[\tilde{\boldsymbol{t}}_1, \tilde{\boldsymbol{t}}_2, \ \ldots, \tilde{\boldsymbol{t}}_K, \boldsymbol{l}_t, \boldsymbol{\zeta}, \boldsymbol{\alpha}\right]$ rather than the measurement parameters $\boldsymbol{l}_{TR}$ and $\boldsymbol{\omega}$.

The parameters in $\boldsymbol{\theta}$ include K tensors, each of which is $\tilde{\boldsymbol{t}}_k \in \mathbb{R}^{6\times 1}$, the target location

$\boldsymbol{l}_t \in \mathbb{R}^{3\times 1}$, a vector of the relaxation frequencies $\boldsymbol{\zeta} = [\zeta_1, \zeta_2, \ \ldots, \zeta_p]^T \in \mathbb{R}^{P\times 1}$, and $\boldsymbol{\alpha} \in \mathbb{R}^{Q\times 1}$ is a real vector of the Q unknown, nonzero α_{pk} terms.[1]

The likelihood function of the data is

$$p(\boldsymbol{m};\boldsymbol{\theta}) = \frac{1}{(\pi\sigma_n^2)^{MN}} \cdot \exp\left\{ \frac{1}{\sigma_n^2} [\boldsymbol{m} - \boldsymbol{r}(\boldsymbol{\theta})]^H [\boldsymbol{m} - \boldsymbol{r}(\boldsymbol{\theta})] \right\} \tag{8.2}$$

When the likelihood function is of the form in (8.2), the entries for the Fisher information matrix (FIM) are well understood to be [20]

$$[\boldsymbol{I}(\boldsymbol{\theta})]_{ij} = \frac{2}{\sigma_n^2} \mathrm{Re}\left\{ \left(\frac{\partial \boldsymbol{r}(\boldsymbol{\theta})}{\partial \theta_i} \right)^H \left(\frac{\partial \boldsymbol{r}(\boldsymbol{\theta})}{\partial \theta_j} \right) \right\} \tag{8.3}$$

As can be seen from (8.3), determining the entries of the FIM amounts to calculating partial derivatives of the signal model with respect to the unknown parameters in $\boldsymbol{\theta}$. The partial of the model with respect to ζ_p is

$$\boldsymbol{d}_{\zeta_p} = \frac{\partial \boldsymbol{r}}{\partial \zeta_p} = \sum_k \boldsymbol{H}_s(\boldsymbol{l}_t)\tilde{\boldsymbol{t}}_k \otimes \boldsymbol{f}'_{k,\,\zeta_p} \tag{8.4}$$

where

$$\boldsymbol{f}'_{k,\,\zeta_p} = \frac{\partial \boldsymbol{f}_k(\boldsymbol{\omega})}{\partial \zeta_p} = \frac{j\boldsymbol{\omega}}{(j\boldsymbol{\omega} + \zeta_p)^2} \alpha_{pk} \tag{8.5}$$

The partial of the model with respect to α_{pk} for $p \geq 1$ is

$$\boldsymbol{d}_{\alpha_{pk}} = \frac{\partial \boldsymbol{r}}{\partial \alpha_{pk}} = \boldsymbol{H}_s(\boldsymbol{l}_t)\tilde{\boldsymbol{t}}_k \otimes \boldsymbol{f}'_{\alpha_{pk}} \tag{8.6}$$

[1] A general expression for the dimensionality of the $\boldsymbol{\alpha}$ vector as a function of P and K is not possible to obtain because it is specific to the form of the relaxation frequency responses. If all of the K relaxation frequency responses have unique relaxation frequencies (no repeated frequencies), then $Q = P - K$. If multiple tensors share a common relaxation frequency, there will be more than $Q > P - K$ amplitudes; however, in this thesis, we typically analyze targets with unique relaxation frequencies for each tensor, so the $Q = P - K$ dimensionality is generally appropriate.

where

$$\boldsymbol{f}'_{\alpha_{pk}} = -\frac{j\boldsymbol{\omega}/\zeta_p}{1 + j\boldsymbol{\omega}/\zeta_p} \tag{8.7}$$

The partial of the model with respect to α_{0k} is

$$\boldsymbol{d}_{\alpha_{0k}} = \frac{\partial \boldsymbol{r}}{\partial \alpha_{0k}} = \boldsymbol{H}_s(\boldsymbol{l}_t)\tilde{\boldsymbol{t}}_k \otimes \boldsymbol{f}'_{\alpha_{0k}} \tag{8.8}$$

where

$$\boldsymbol{f}'_{\alpha_{0k}} = \mathbf{1}_{M\times 1} \tag{8.9}$$

The partial of the model with respect to target's $x-$position is

$$\boldsymbol{d}_{x_t} = \frac{\partial \boldsymbol{r}}{\partial x_t} = \sum_k \boldsymbol{H}'_{s,x}(\boldsymbol{l}_t)\tilde{\boldsymbol{t}}_k \otimes \boldsymbol{f}_k(\boldsymbol{\omega}) \tag{8.10}$$

where $\boldsymbol{H}'_{s,x} \in \mathbb{R}^{N\times 6}$ is the derivative of the magnetic scene matrix with respect to the x-coordinate of the target location. The partials of the model with respect to the target's $y-$position and $z-$position are similar in form:

$$\boldsymbol{d}_{y_t} = \frac{\partial \boldsymbol{r}}{\partial y_t} = \sum_k \boldsymbol{H}'_{s,y}(\boldsymbol{l}_t)\tilde{\boldsymbol{t}}_k \otimes \boldsymbol{f}_k(\boldsymbol{\omega}) \tag{8.11a}$$

$$\boldsymbol{d}_{z_t} = \frac{\partial \boldsymbol{r}}{\partial z_t} = \sum_k \boldsymbol{H}'_{s,z}(\boldsymbol{l}_t)\tilde{\boldsymbol{t}}_k \otimes \boldsymbol{f}_k(\boldsymbol{\omega}). \tag{8.11b}$$

The partial of the model with respect to $\tilde{\boldsymbol{t}}_k$ is

$$\begin{aligned} \boldsymbol{D}_{\tilde{\boldsymbol{t}}_k} = \frac{\partial \boldsymbol{r}}{\partial \tilde{\boldsymbol{t}}_k} &= \left[\frac{\partial \boldsymbol{r}}{\partial \tilde{t}_{xx,k}}, \frac{\partial \boldsymbol{r}}{\partial \tilde{t}_{yy,k}}, \frac{\partial \boldsymbol{r}}{\partial \tilde{t}_{zz,k}}, \frac{\partial \boldsymbol{r}}{\partial \tilde{t}_{xy,k}}, \frac{\partial \boldsymbol{r}}{\partial \tilde{t}_{xz,k}}, \frac{\partial \boldsymbol{r}}{\partial \tilde{t}_{yz,k}}\right] \\ &= \boldsymbol{H}_s(\boldsymbol{l}_t) \otimes \boldsymbol{f}_k(\boldsymbol{\omega}) \end{aligned} \tag{8.12}$$

where the columns of $\boldsymbol{D}_{\tilde{\boldsymbol{t}}_k} \in \mathbb{C}^{MN\times 6}$ are the partial derivatives with respect to the 6 components of the k-th tensor. Each column of $\boldsymbol{D}_{\tilde{\boldsymbol{t}}_k}$ is thus $\boldsymbol{d}_{\tilde{t}_{ij,k}} \in \mathbb{C}^{MN\times 1}$. We can group the other model derivatives in a similar fashion according to their associated parameter set.

Continuing the notation $\boldsymbol{D}_{[\cdot]}$ to indicate a matrix of partial derivatives of the model with respect to a parameter, we define $\boldsymbol{D}_{\zeta} \in \mathbb{C}^{MN \times P}$ to be

$$\boldsymbol{D}_{\zeta} = \left[\boldsymbol{d}_{\zeta_1}, \boldsymbol{d}_{\zeta_2}, \ \ldots, \boldsymbol{d}_{\zeta_p}\right] \tag{8.13}$$

Similarly, we define $\boldsymbol{D}_{\alpha} \in \mathbb{C}^{MN \times Q}$, $\boldsymbol{D}_{l_t} \in \mathbb{C}^{MN \times 3}$, and $\boldsymbol{D}_{\boldsymbol{t}} \in \mathbb{C}^{MN \times 6K}$ to be

$$\boldsymbol{D}_{\alpha} = \left[\boldsymbol{d}_{\alpha_{01}}, \boldsymbol{d}_{\alpha_{11}}, \ \ldots, \boldsymbol{d}_{\alpha_{02}}, \boldsymbol{d}_{\alpha_{12}}, \ \ldots, \boldsymbol{d}_{\alpha_{PK}}\right] \tag{8.14}$$

$$\boldsymbol{D}_{l_t} = \left[\boldsymbol{d}_{x_t}, \boldsymbol{d}_{y_t}, \boldsymbol{d}_{z_t}\right] \tag{8.15}$$

$$\boldsymbol{D}_{\boldsymbol{t}} = \left[\boldsymbol{D}_{\tilde{t}_1}, \boldsymbol{D}_{\tilde{t}_2}, \ \ldots, \boldsymbol{D}_{\tilde{t}_K}\right] \tag{8.16}$$

We define $\boldsymbol{J}(\boldsymbol{\theta})$ as

$$\boldsymbol{J}(\boldsymbol{\theta}) = \left[\boldsymbol{D}_{\boldsymbol{\zeta}} \quad \boldsymbol{D}_{\boldsymbol{\alpha}} \quad \boldsymbol{D}_{\boldsymbol{t}} \quad \boldsymbol{D}_{l_t}\right] \tag{8.17}$$

then the FIM can be written as

$$\boldsymbol{I}(\boldsymbol{\theta}) = \frac{2}{\sigma_n^2} \mathrm{Re}\left\{\boldsymbol{J}^H(\boldsymbol{\theta})\boldsymbol{J}(\boldsymbol{\theta})\right\} \tag{8.18}$$

In partitioned form, this matrix can be expressed as

$$\boldsymbol{I}(\boldsymbol{\theta}) = \frac{2}{\sigma_n^2} \mathrm{Re}\left\{\begin{bmatrix} \boldsymbol{D}_{\zeta}^H\boldsymbol{D}_{\zeta} & \boldsymbol{D}_{\zeta}^H\boldsymbol{D}_{\alpha} & \boldsymbol{D}_{\zeta}^H\boldsymbol{D}_{\boldsymbol{t}} & \boldsymbol{D}_{\zeta}^H\boldsymbol{D}_{l_t} \\ \boldsymbol{D}_{\alpha}^H\boldsymbol{D}_{\zeta} & \boldsymbol{D}_{\alpha}^H\boldsymbol{D}_{\alpha} & \boldsymbol{D}_{\alpha}^H\boldsymbol{D}_{\boldsymbol{t}} & \boldsymbol{D}_{\alpha}^H\boldsymbol{D}_{l_t} \\ \boldsymbol{D}_{\boldsymbol{t}}^H\boldsymbol{D}_{\zeta} & \boldsymbol{D}_{\boldsymbol{t}}^H\boldsymbol{D}_{\alpha} & \boldsymbol{D}_{\boldsymbol{t}}^H\boldsymbol{D}_{\boldsymbol{t}} & \boldsymbol{D}_{\boldsymbol{t}}^H\boldsymbol{D}_{l_t} \\ \boldsymbol{D}_{l_t}^H\boldsymbol{D}_{\zeta} & \boldsymbol{D}_{l_t}^H\boldsymbol{D}_{\alpha} & \boldsymbol{D}_{l_t}^H\boldsymbol{D}_{\boldsymbol{t}} & \boldsymbol{D}_{l_t}^H\boldsymbol{D}_{l_t} \end{bmatrix}\right\} \tag{8.19}$$

The CRB matrix $\boldsymbol{C}_{CR}(\boldsymbol{\theta})$, which is a lower bound on the covariance of any unbiased esti-

mator of these parameters, is written as

$$\boldsymbol{C}_{CR}(\boldsymbol{\theta}) = \boldsymbol{I}^{-1}(\boldsymbol{\theta}) = \begin{bmatrix} \boldsymbol{C}_{CR}(\boldsymbol{\zeta}) & \boldsymbol{C}_{CR}(\boldsymbol{\zeta},\boldsymbol{\alpha}) & \boldsymbol{C}_{CR}(\boldsymbol{\zeta},\boldsymbol{t}) & \boldsymbol{C}_{CR}(\boldsymbol{\zeta},\boldsymbol{l}_t) \\ \boldsymbol{C}_{CR}(\boldsymbol{\alpha},\boldsymbol{\zeta}) & \boldsymbol{C}_{CR}(\boldsymbol{\alpha}) & \boldsymbol{C}_{CR}(\boldsymbol{\alpha},\boldsymbol{t}) & \boldsymbol{C}_{CR}(\boldsymbol{\alpha},\boldsymbol{l}_t) \\ \boldsymbol{C}_{CR}(\boldsymbol{t},\boldsymbol{\zeta}) & \boldsymbol{C}_{CR}(\boldsymbol{t},\boldsymbol{\alpha}) & \boldsymbol{C}_{CR}(\boldsymbol{t}) & \boldsymbol{C}_{CR}(\boldsymbol{t},\boldsymbol{l}_t) \\ \boldsymbol{C}_{CR}(\boldsymbol{l}_t,\boldsymbol{\zeta}) & \boldsymbol{C}_{CR}(\boldsymbol{l}_t,\boldsymbol{\alpha}) & \boldsymbol{C}_{CR}(\boldsymbol{l}_t,\boldsymbol{t}) & \boldsymbol{C}_{CR}(\boldsymbol{l}_t) \end{bmatrix} \tag{8.20}$$

where the noise variance fraction has been included in the matrix entries. Each $\boldsymbol{C}_{CR}(\cdot)$ matrix is the lower bound on the covariance of any unbiased estimator of the parameter(s) in parentheses. For example, $\boldsymbol{C}_{CR}(\boldsymbol{\zeta})$ is the lower bound on the covariance of any unbiased estimator of the $\boldsymbol{\zeta}$ terms. Similarly, $\boldsymbol{C}_{CR}(\boldsymbol{\alpha},\boldsymbol{\zeta})$ is the lower bound on the covariance of any unbiased estimator of $\boldsymbol{\alpha}$ and $\boldsymbol{\zeta}$.

The matrices along the diagonal in (8.20), $\boldsymbol{C}_{CR}(\boldsymbol{\zeta})$, $\boldsymbol{C}_{CR}(\boldsymbol{\alpha})$, $\boldsymbol{C}_{CR}(\boldsymbol{t})$, and $\boldsymbol{C}_{CR}(\boldsymbol{l}_t)$, are of interest because their diagonal entries are the CRBs of the unknown parameters. In other words, $[\boldsymbol{C}_{CR}(\boldsymbol{\theta})]_{ii} = \text{CRB}(\theta_{ii})$. These quantities are referred to as the SoT CRBs.

8.3 Validation of Rank-K CRB Derivation

In this section, we validate the CRBs derived in Section 8.2. To validate the CRBs, we perform Monte Carlo analysis for two rank-two targets. We show excellent agreement between the bounds and the Monte Carlo results for both targets, giving us confidence that the analytic bounds are correct.

8.3.1 Monte Carlo Description

This section describes the different aspects of the Monte Carlo analysis used to validate the rank-K CRB derivation including the measurement system parameters and the details of the Monte Carlo trials.

We consider measurements using the sensor in Figure 2.4 and the scan pattern in Figure 2.3. The measurement frequency scheme is the same as in Section 2.6.

For each target model, 200 measurement realizations are generated at three different target SNRs, denoted SNR_T, and the unknown parameters are estimated using a maximum likelihood estimator for each trial. The sample standard deviation is calculated across all trials for each parameter at each SNR_T. The sample standard deviations are shown as blue circular markers on the subsequent figures in this section. We define SNR_T as

$$\text{SNR}_T = \frac{\left\| \sum_{k=1}^{K} \boldsymbol{H}_s(\boldsymbol{l}_t)\tilde{\boldsymbol{t}}_k \otimes \boldsymbol{f}_k(\boldsymbol{\omega}) \right\|_2^2}{\sigma_n^2} \tag{8.21}$$

The MLE used for the Monte Carlo analysis takes the form shown in (8.22), where $\boldsymbol{r}(\boldsymbol{\theta})$ is the same as in (8.1).

$$\min_{\boldsymbol{\theta}} \|\boldsymbol{m} - \boldsymbol{r}(\boldsymbol{\theta})\|_2^2 \tag{8.22}$$

In solving (8.22), we use the MATLAB built-in function *fminsearch*$(\cdot)$ with the default parameters, except for the following: TolFun = $3e{-}3$, TolX = $1e{-}9$, MaxIter = $50e3$, MaxFunEvals = $50e3$.

8.3.2 Target Descriptions

Target 1: Rank-Two Target with Two Relaxation Frequencies

The first target we consider is the two orthogonal loops target with different relaxation frequencies from Section 2.4.2. The signal model for this target is

$$\boldsymbol{r}(\boldsymbol{\omega}, \boldsymbol{l}_{TR}) = \sum_{k=1}^{2} \boldsymbol{H}_s(\boldsymbol{l}_t)\tilde{\boldsymbol{t}}_k \otimes \boldsymbol{f}_k(\boldsymbol{\omega}) \tag{8.23}$$

The tensors for this target are $\tilde{\boldsymbol{t}}_1 = [t_1, 0, 0, 0, 0, 0]^T$ and $\tilde{\boldsymbol{t}}_2 = [0, 0, t_2, 0, 0, 0]^T$ where $t_1 = 1$ and $t_2 = 1$. The target is located at $\boldsymbol{l}_t = (0, 0, 7.5)$ cm. The relaxation frequency response

corresponding to each tensor is

$$\boldsymbol{f}_1(\boldsymbol{\omega}) = -\frac{j\boldsymbol{\omega}/\zeta_1}{1 + j\boldsymbol{\omega}/\zeta_1} \tag{8.24a}$$

$$\boldsymbol{f}_2(\boldsymbol{\omega}) = -\frac{j\boldsymbol{\omega}/\zeta_2}{1 + j\boldsymbol{\omega}/\zeta_2} \tag{8.24b}$$

where $\zeta_1 = 3.2$ kHz , $\zeta_2 = 14.3$ kHz. The FIM takes the following form

$$\boldsymbol{I}(\boldsymbol{\theta}) = \frac{2}{\sigma_n^2} \mathrm{Re}\left\{ \begin{bmatrix} \boldsymbol{D}_\zeta^H \boldsymbol{D}_\zeta & \boldsymbol{D}_\zeta^H \boldsymbol{D}_t & \boldsymbol{D}_\zeta^H \boldsymbol{D}_{l_t} \\ \boldsymbol{D}_t^H \boldsymbol{D}_\zeta & \boldsymbol{D}_t^H \boldsymbol{D}_t & \boldsymbol{D}_t^H \boldsymbol{D}_{l_t} \\ \boldsymbol{D}_{l_t}^H \boldsymbol{D}_\zeta & \boldsymbol{D}_{l_t}^H \boldsymbol{D}_t & \boldsymbol{D}_{l_t}^H \boldsymbol{D}_{l_t} \end{bmatrix} \right\} \tag{8.25}$$

In this model, there are 17 unknown parameters: $6 * 2$ tensor unknowns, 3 location unknowns, and 2 relaxation frequencies. Thus, the FIM is $\boldsymbol{I}(\boldsymbol{\theta}) \in \mathbb{R}^{17\times 17}$.

Target 2: Rank-Two Target with Three Relaxation Frequencies

For the second target, we consider a rank-two target with three relaxation frequencies, where the tensors are not aligned with the coordinate axes. The signal model for this target is

$$\boldsymbol{r}(\boldsymbol{\omega}, \boldsymbol{l}_{TR}) = \sum_{k=1}^{2} \boldsymbol{H}_s(\boldsymbol{l}_t)\tilde{\boldsymbol{t}}_k \otimes \boldsymbol{f}_k(\boldsymbol{\omega}) \tag{8.26}$$

To generate the tensors for this target, we begin with $\tilde{\boldsymbol{t}}_1 = [t_1, 0, 0, 0, 0, 0]^T$ and $\tilde{\boldsymbol{t}}_2 = [0, 0, t_2, 0, 0, 0]^T$, where $t_1 = t_2 = 1$. We rotate each tensor by $\alpha = 30$ degrees, $\beta = 60$ degrees, and $\gamma = 0$ degrees. The rotation matrix is

$$\boldsymbol{R}(\alpha = 30^\circ, \beta = 60^\circ, \gamma = 0^\circ) = \begin{bmatrix} 0.433 & -0.500 & 0.750 \\ 0.250 & 0.866 & 0.433 \\ -0.866 & 0 & 0.500 \end{bmatrix} \tag{8.27}$$

We convert the tensors to their matrix forms using the relationship in (2.11), apply the rotation using (2.37), and convert back to the linear form using the relationship in (2.11) again. The resulting tensors for this target are $\tilde{\boldsymbol{t}}_1 = [0.1875, 0.2500, 0.5625, -0.2165, -0.3750, 0.3248]^T$ and $\tilde{\boldsymbol{t}}_2 = [0.7500, 0, 0.2500, 0, 0, -0.4330]^T$. The target is located at $\boldsymbol{l}_t = (0, 0, 7.5)$ cm. The relaxation frequency response corresponding to each tensor is

$$\boldsymbol{f}_1(\boldsymbol{\omega}) = -\frac{j\boldsymbol{\omega}/\zeta_1}{1 + j\boldsymbol{\omega}/\zeta_1} - \alpha_{21}\frac{j\boldsymbol{\omega}/\zeta_2}{1 + j\boldsymbol{\omega}/\zeta_2} \tag{8.28a}$$

$$\boldsymbol{f}_2(\boldsymbol{\omega}) = -\frac{j\boldsymbol{\omega}/\zeta_3}{1 + j\boldsymbol{\omega}/\zeta_3} \tag{8.28b}$$

where $\zeta_1 = 330$ Hz , $\zeta_2 = 90$ kHz, $\zeta_3 = 5.4$ kHz, and $\alpha_{21} = 1$. There are 19 unknowns in this model: $2 * 6$ tensor unknowns, 3 relaxation frequencies, 1 amplitude unknown, and 3 location unknowns. The FIM takes the form shown below.

$$\boldsymbol{I}(\boldsymbol{\theta}) = \frac{2}{\sigma_n^2}\mathrm{Re}\left\{\begin{bmatrix} \boldsymbol{D}_\zeta^H\boldsymbol{D}_\zeta & \boldsymbol{D}_\zeta^H\boldsymbol{D}_\alpha & \boldsymbol{D}_\zeta^H\boldsymbol{D}_t & \boldsymbol{D}_\zeta^H\boldsymbol{D}_{l_t} \\ \boldsymbol{D}_\alpha^H\boldsymbol{D}_\zeta & \boldsymbol{D}_\alpha^H\boldsymbol{D}_\alpha & \boldsymbol{D}_\alpha^H\boldsymbol{D}_t & \boldsymbol{D}_\alpha^H\boldsymbol{D}_{l_t} \\ \boldsymbol{D}_t^H\boldsymbol{D}_\zeta & \boldsymbol{D}_t^H\boldsymbol{D}_\alpha & \boldsymbol{D}_t^H\boldsymbol{D}_t & \boldsymbol{D}_t^H\boldsymbol{D}_{l_t} \\ \boldsymbol{D}_{l_t}^H\boldsymbol{D}_\zeta & \boldsymbol{D}_{l_t}^H\boldsymbol{D}_\alpha & \boldsymbol{D}_{l_t}^H\boldsymbol{D}_t & \boldsymbol{D}_{l_t}^H\boldsymbol{D}_{l_t} \end{bmatrix}\right\} \tag{8.29}$$

8.3.3 Comparison of Monte Carlo Analysis to Analytic CRBs

This section contains the comparisons of the Monte Carlo results with the analytic CRBs for the two targets.

Target 1: Rank-Two Target with Two Relaxation Frequencies

The comparisons of the Monte Carlo results with the analytic CRBs computed for **Target 1: Rank-Two Target with Two Relaxation Frequencies** are shown in Figure 8.1 for $\tilde{\boldsymbol{t}}_1$, Figure 8.2 for $\tilde{\boldsymbol{t}}_2$, Figure 8.3 for $\boldsymbol{l}_t$, and Figure 8.4 for $\boldsymbol{\zeta}$. Excellent agreement is observed between the Monte Carlo results and the analytic CRBs for all of the parameters.

Target 2: Rank-Two Target with Three Relaxation Frequencies

The comparisons of the Monte Carlo results to the analytic CRBs computed for **Target 2: Rank-Two Target with Three Relaxation Frequencies** are shown in Figure 8.5 for $\tilde{\boldsymbol{t}}_1$, Figure 8.6 for $\tilde{\boldsymbol{t}}_2$, Figure 8.7 for $\boldsymbol{l}_t$, and Figure 8.8 for $\boldsymbol{\zeta}$ and α_{21}. Excellent agreement is observed between the Monte Carlo results and the analytic CRBs for all of the parameters.

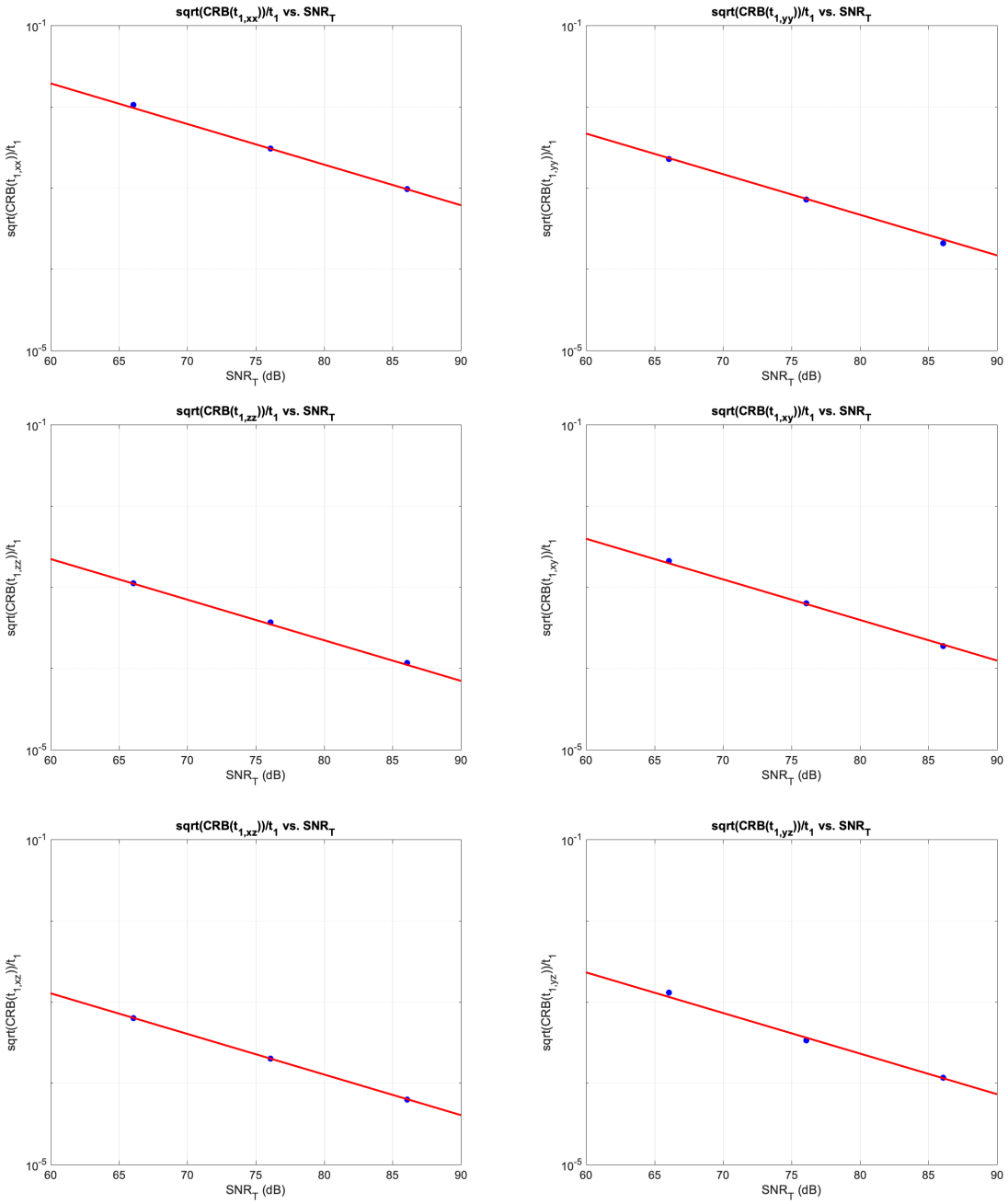

Figure 8.1: CRB($\tilde{\boldsymbol{t}}_1$) for **Target 1: Rank-Two Target with Two Relaxation Frequencies**: Comparison of Monte Carlo results (circle blue markers) to the analytic CRBs (solid red line) for the six tensor components in $\tilde{\boldsymbol{t}}_1$. Excellent agreement is observed between the Monte Carlo results and the analytic CRBs.

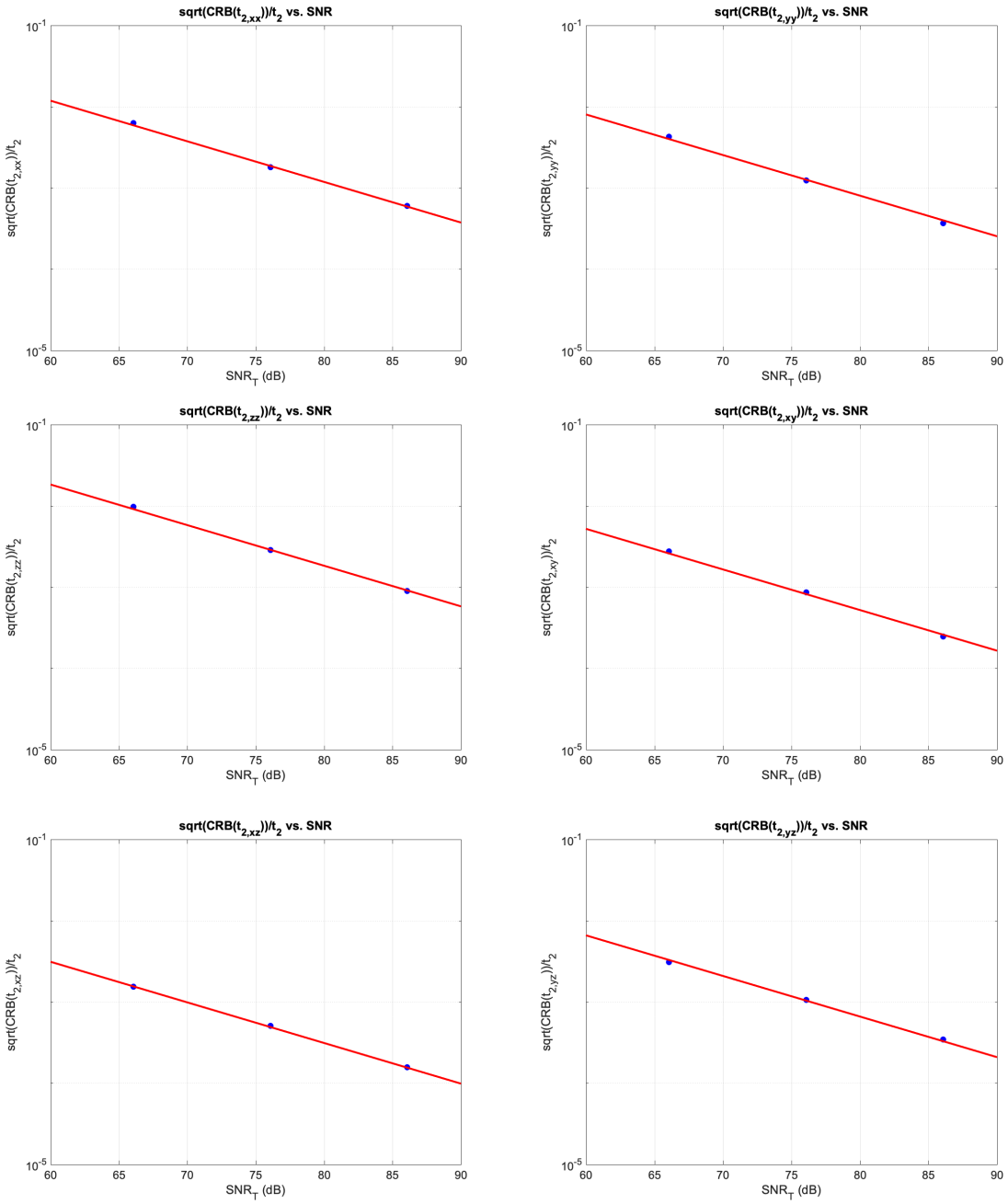

Figure 8.2: CRB($\tilde{\boldsymbol{t}}_2$) for **Target 1: Rank-Two Target with Two Relaxation Frequencies**: Comparison of Monte Carlo results (circle blue markers) to the analytic CRBs (solid red line) for the six tensor components in $\tilde{\boldsymbol{t}}_2$. Excellent agreement is observed between the Monte Carlo results and the analytic CRBs.

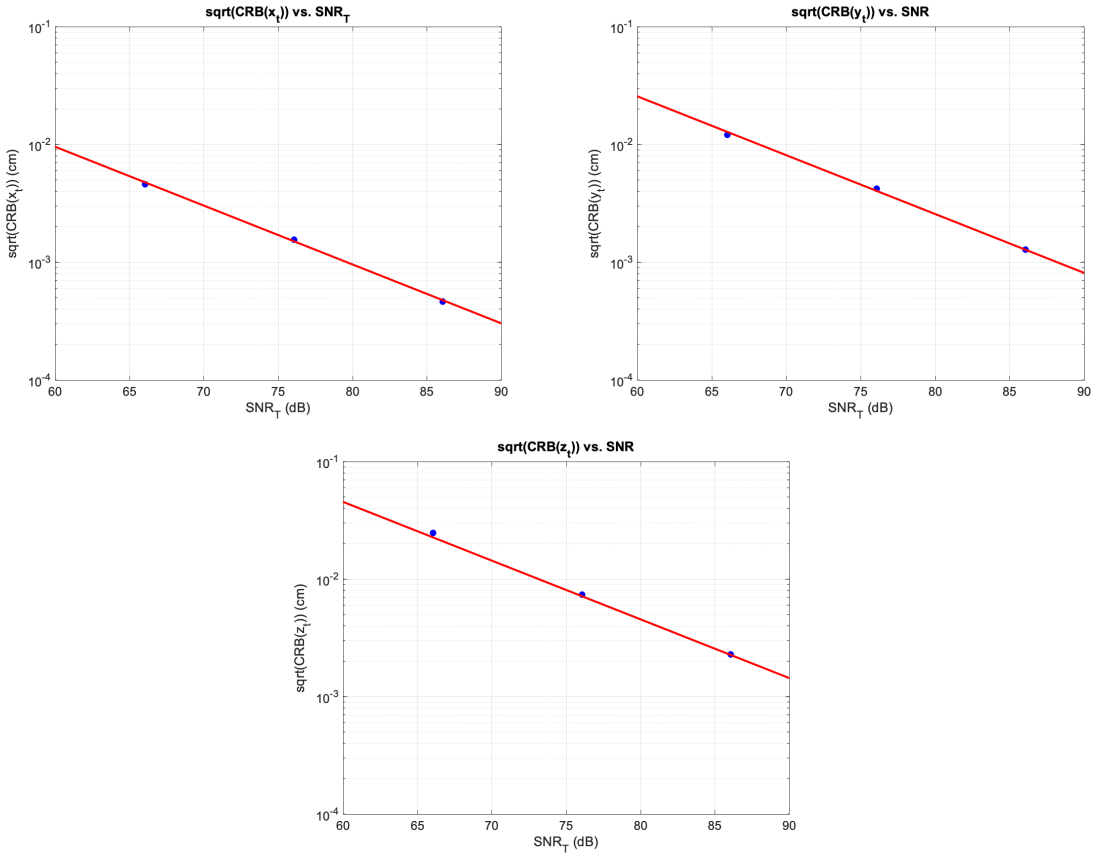

Figure 8.3: CRB($\boldsymbol{l}_t$) for **Target 1: Rank-Two Target with Two Relaxation Frequencies**: Comparison of Monte Carlo results (circle blue markers) to the analytic CRBs (solid red line) for the three location components in $\boldsymbol{l}_t$. Results are shown in centimeters (cm). Excellent agreement is observed between the Monte Carlo results and the analytic CRBs.

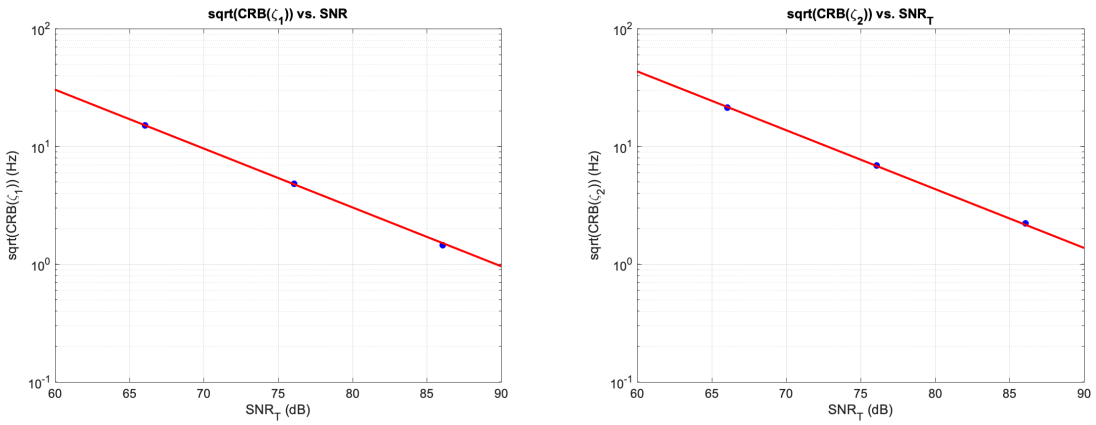

Figure 8.4: CRB($\boldsymbol{\zeta}$) for **Target 1: Rank-Two Target with Two Relaxation Frequencies**: Comparison of Monte Carlo results (circle blue markers) to the analytic CRBs (solid red line) for the two relaxation frequencies. Results are shown in Hertz (Hz). Excellent agreement is observed between the Monte Carlo results and the analytic CRBs.

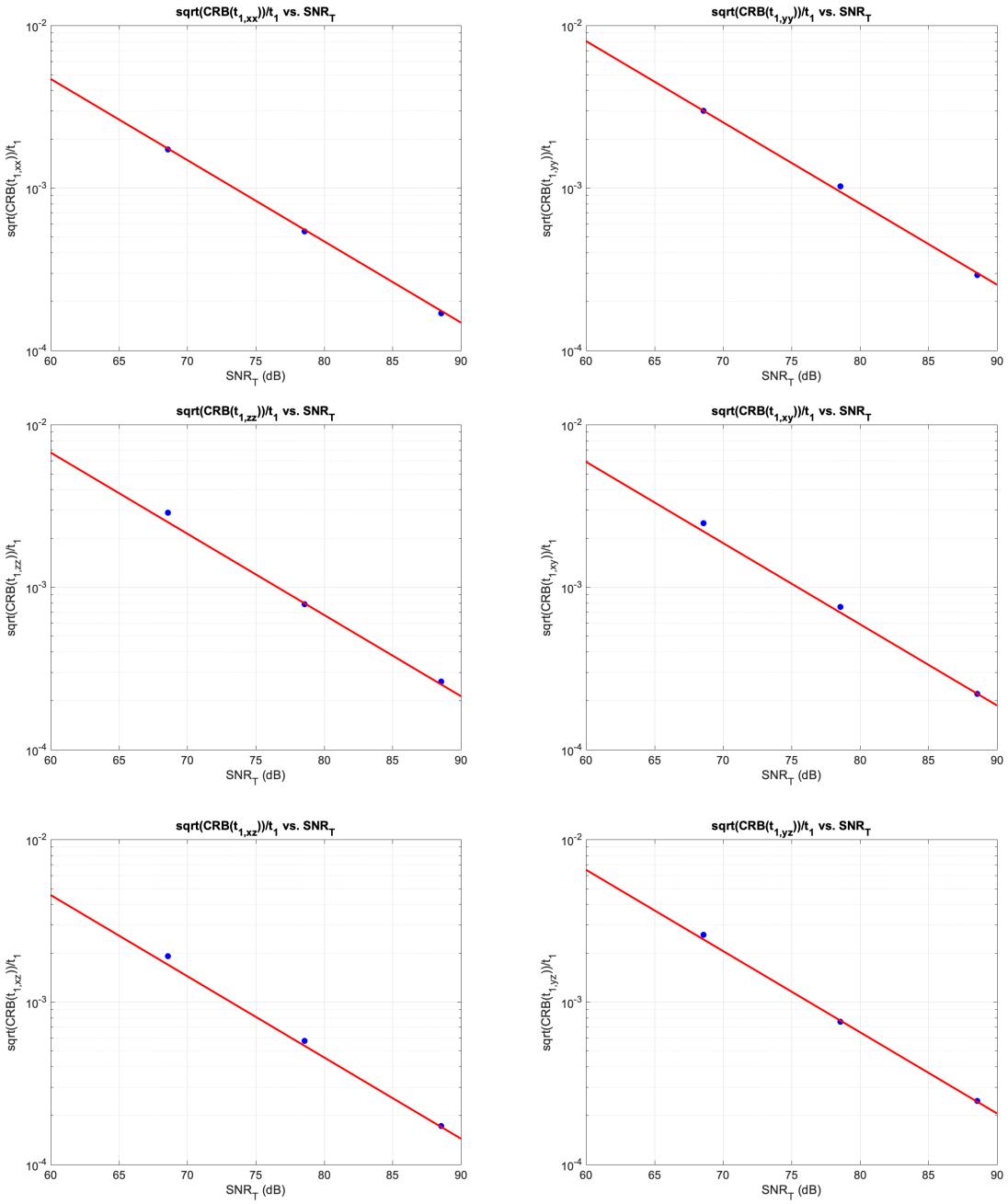

Figure 8.5: CRB($\tilde{t}_1$) for **Target 2: Rank-Two Target with Three Relaxation Frequencies**: Comparison of Monte Carlo results (circle blue markers) to the analytic CRBs (solid red line) for the six tensor components in $\tilde{t}_1$. Excellent agreement is observed between the Monte Carlo results and the analytic CRBs.

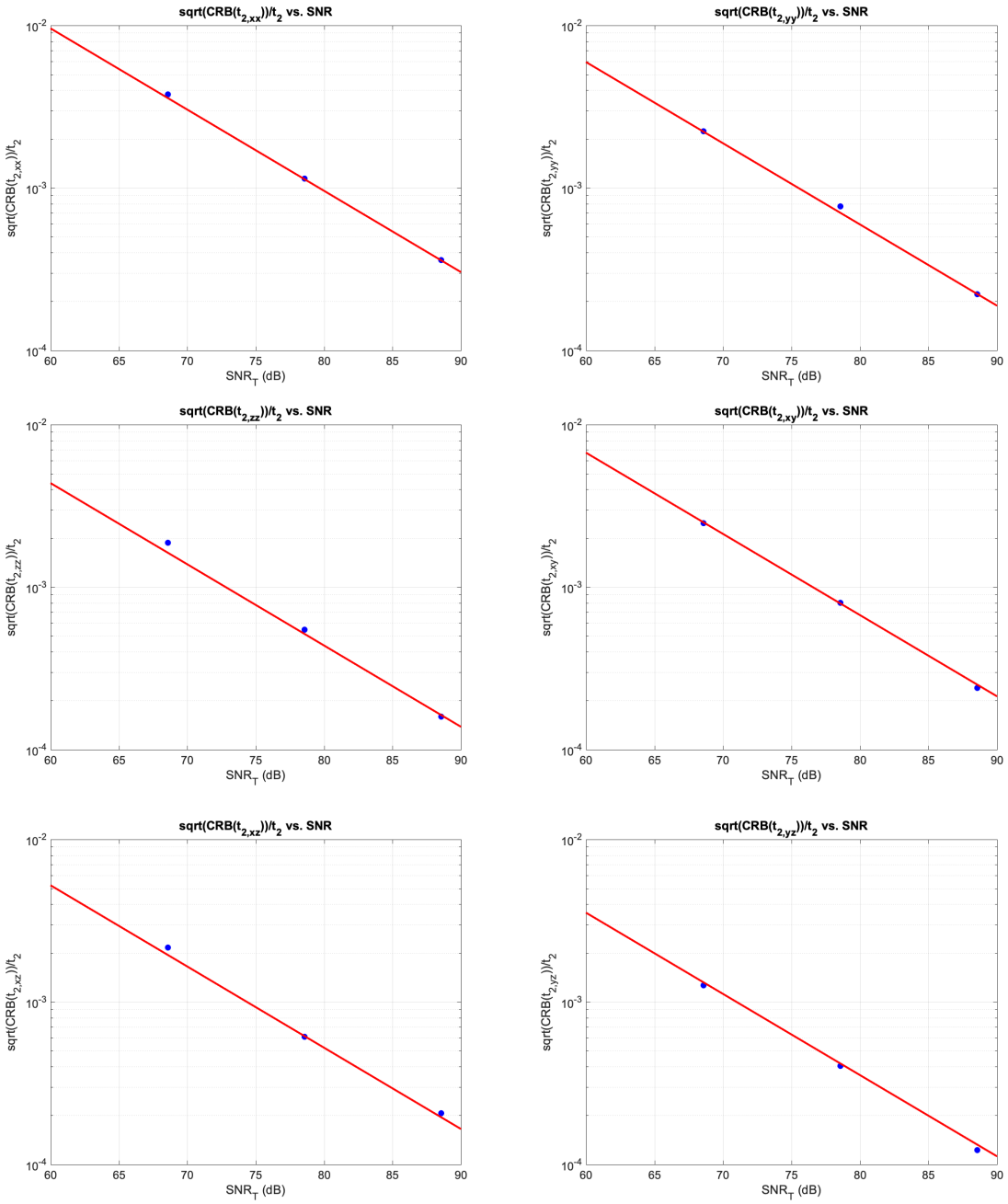

Figure 8.6: CRB($\tilde{t}_2$) for **Target 2: Rank-Two Target with Three Relaxation Frequencies**: Comparison of Monte Carlo results (circle blue markers) to the analytic CRBs (solid red line) for the six tensor components in $\tilde{t}_2$. Excellent agreement is observed between the Monte Carlo results and the analytic CRBs.

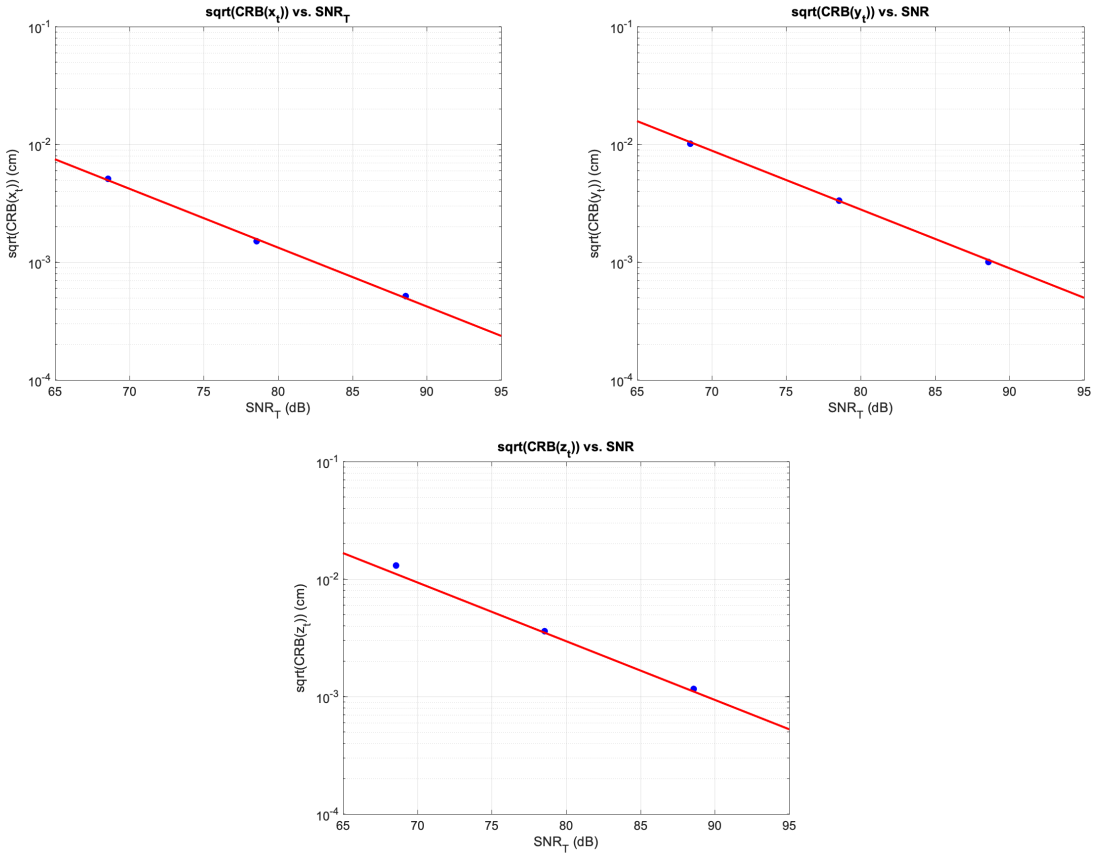

Figure 8.7: CRB($\boldsymbol{l}_t$) for **Target 2: Rank-Two Target with Three Relaxation Frequencies**: Comparison of Monte Carlo results (circle blue markers) to the analytic CRBs (solid red line) for the three location components in $\boldsymbol{l}_t$. Results are shown in centimeters (cm). Excellent agreement is observed between the Monte Carlo results and the analytic CRBs.

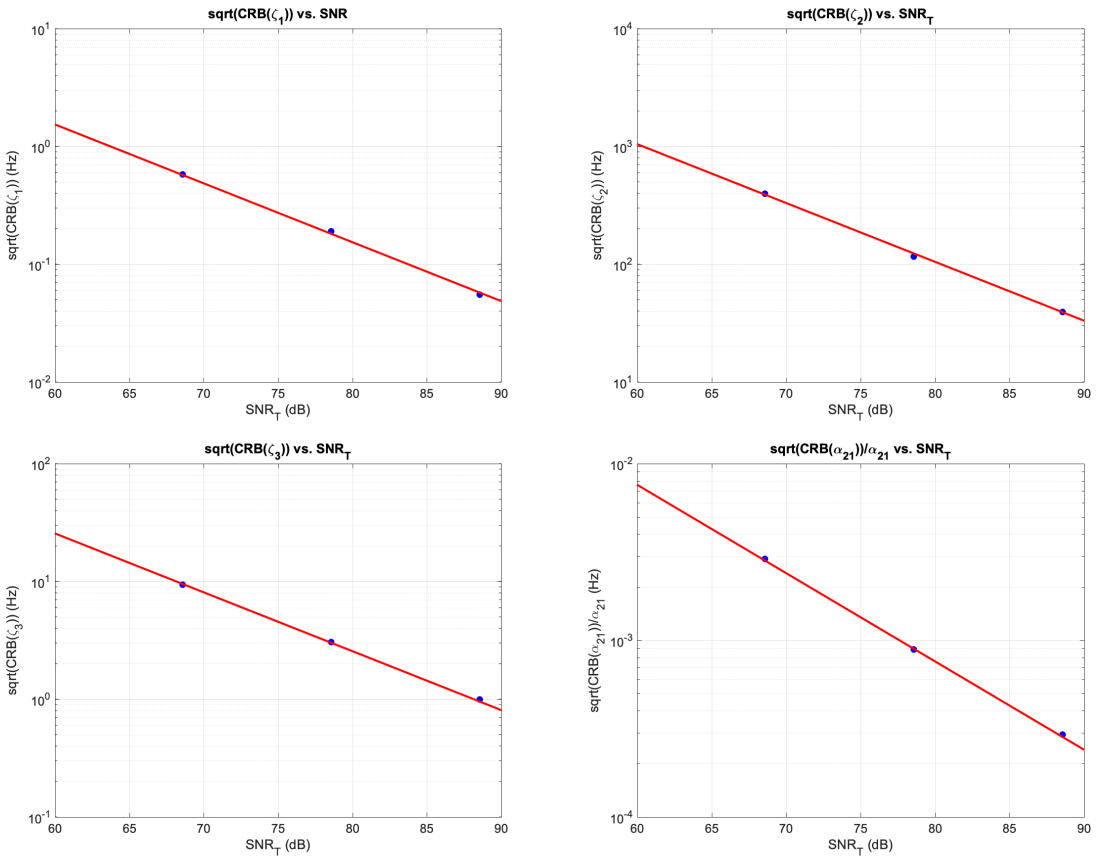

Figure 8.8: CRB($\boldsymbol{\zeta}$) and CRB(α_{21}) for **Target 2: Rank-Two Target with Three Relaxation Frequencies**: Comparison of Monte Carlo results (blue circle markers) to the analytic CRBs (solid red line). Excellent agreement is observed between the Monte Carlo results and the analytic CRBs for the three unknown relaxation frequencies and the one unknown amplitude. Note the y-axis extent for the unknown amplitude (lower right) is different than the three relaxation frequencies.

CHAPTER 9
CONCLUSIONS AND FUTURE WORK

In this chapter, we summarize the contributions presented in this thesis, organized by chapter, and identify a number of avenues for future work.

9.1 Summary of Contributions

The objective of this research is to derive and analyze the theoretical performance bounds for the variance of any unbiased estimator (i.e., Cramer-Rao lower bounds) of these target parameters given a set of EMI measurements. The goal is to provide a framework that is independent of how the signals are processed for assessing the theoretical performance of current and future EMI systems and to generate a benchmark for current estimation techniques of these parameters. The framework and corresponding analysis will provide a better understanding of the factors that influence these bounds, giving researchers additional insight to develop better EMI systems and estimators.

The contributions towards the aforementioned goals are described below according to the chapter in which they are discussed:

- **Chapter 3** We derive the CRBs for the tensors, relaxation frequencies, and target location for an arbitrary frequency-domain EMI system from the perspective of the sum of dipoles form of the signal model. We use the transformation property of the CRB to relate the CRBs of the tensors to actual parameters of interest for classification including the Frobenius and spectral norms of the tensors.

- **Chapter 4** We derive the CRBs for the unknown target parameters associated with the sum of tensor form of the signal model for rank-one targets, which is a special class of targets that can be modeled using a single independent basis tensor. This

derivation enables a direct connection between recent signal processing techniques for frequency-domain EMI data and the corresponding CRBs.

- **Chapter 5** We illustrate how a recent signal processing technique for processing EMI data factors the measurement into separate frequency and spatial responses, allowing the relaxation frequencies and their corresponding amplitudes to be estimated separately from the target location and the tensor [26]. We compare maximum likelihood estimators of the unknown parameters using this factorization to the CRBs derived in Chapter 4.

- **Chapter 6** We derive approximate CRB expressions based on the factored frequency and spatial models for targets that can be described by a single basis tensor. Although they are approximate, these bounds are essentially the same as the previously derived CRBs, and the expressions are a simplification over the CRBs derived in Chapter 3 and Chapter 4. These simplified expressions provide a means for developing intuition for the different factors influencing the CRBs.

- **Chapter 7** We use the approximate CRB expressions to carry out different types of analyses for the frequency and spatial unknowns. For the frequency parameters, we explore the dependence of the CRBs on the spacing between relaxation frequencies, their relative strength, and the number of relaxation frequencies for a given target model. For the spatial parameters, we explore the dependence of the CRBs as a function of the target depth, target rotation, and signal-to-noise ratio.

- **Chapter 8** We derive the CRBs for the basis tensors, relaxation frequencies, their corresponding amplitudes, and the target location for an arbitrary frequency-domain EMI system for a target with an arbitrary number of basis tensors from the perspective of the sum of tensors form of the signal model. This extension of Chapter 4 removes the restriction that the targets only have a single independent basis tensor.

9.2 Future Work

There is ample opportunity for future work related to this thesis. These opportunities can be broadly assigned to two categories: derivations that extend the ideas in this thesis, and ideas for using the results in this thesis to improve EMI systems. We have identified the following derivations that extend the work in this thesis:

- Derivation of the CRBs to include measurements of targets in the presence of the soil response as well as statistical noise. The problem of estimating the soil parameters and target parameters is considered in [36], where the soil model is also discussed. This can be accomplished by adding the soil parameters to the vector of unknowns $\boldsymbol{\theta}$, and taking the appropriate derivatives.

- Derivation of the CRBs for measurements of targets in the presence of the ground response, sensor self-response, and statistical noise. The sensor self-response manifests as an additional DC term in the frequency response [13]. This model is also discussed in [38]. These references are a reasonable starting point for model required for the derivation.

- Derivation of the CRBs for measurements of targets in the presence of noise with some covariance $\boldsymbol{\Sigma}$. This is a straightforward extension of the results in this thesis, and can be derived using the generic CRB expression which can be found on pg. 47, Equation (3.31) in [20].

- Derivation of ACRB expressions for targets with more than one independent tensor. This is an extension of the ACRB expressions derived in Chapter 6. A good starting point for doing this might be the model perspective in [25].

- Derivation of the CRBs for multiple targets (not co-located) in the sensor scene. Assuming the two targets are separated by enough distance so that they are non-interacting, the CRB for this scenario could be derived by including additional $\boldsymbol{l}_t$

terms for the different target locations in (3.1) and taking derivatives with respect to each $\boldsymbol{l}_t$ term.

We have identified the following ideas for improving EMI systems that are based on the work in this thesis:

- One could use the CRB or a function of the CRB as a criteria for determining the "optimal" frequency measurement scheme for frequency-domain EMI sensors. For example, one might set up an optimization problem to minimize some function of the CRB over the relaxation frequency bandwidth of interest.

- One could also explore the trade-off between power per frequency and number of frequency measurements using the CRB or some function of the CRBs for the relaxation frequencies as a metric.

- One could also incorporate the CRBs of the unknown parameters as a metric for evaluating sensor designs, in addition to sensitivity and soil rejection [31].

Appendices

APPENDIX A

RELATIONSHIP BETWEEN THE ROTATED TENSOR AND ITS DIAGONAL TENSOR ENTRIES IN THE TARGET COORDINATE SYSTEM

In this section, we describe a matrix $\boldsymbol{U}$ which is used to relate a tensor $\boldsymbol{t}_p$ to the diagonal entries of the tensor in the target coordinate system. The need for the matrix $\boldsymbol{U}$ first arises in this thesis in (2.39), and then later in (3.18).

We begin with (2.39), repeated below in (A.1).

$$\boldsymbol{\Lambda}_p = \boldsymbol{R}(\alpha, \beta, \gamma)\boldsymbol{T}_p\boldsymbol{R}^T(\alpha, \beta, \gamma) \tag{A.1}$$

where

$$\mathbf{T}_p = \begin{bmatrix} t_1 & t_4 & t_6 \\ t_4 & t_2 & t_5 \\ t_6 & t_5 & t_3 \end{bmatrix} \tag{A.2}$$

$$\boldsymbol{R}(\alpha, \beta, \gamma) = \begin{bmatrix} \cos\alpha\cos\beta & \cos\alpha\sin\beta\sin\gamma - \sin\alpha\cos\gamma & \cos\alpha\sin\beta\cos\gamma + \sin\alpha\sin\gamma \\ \sin\alpha\cos\beta & \sin\alpha\sin\beta\sin\gamma + \cos\alpha\cos\gamma & \sin\alpha\sin\beta\cos\gamma - \cos\alpha\sin\gamma \\ -\sin\beta & \cos\beta\sin\gamma & \cos\beta\cos\gamma \end{bmatrix} \tag{A.3}$$

and

$$\boldsymbol{\Lambda}_p = \begin{bmatrix} \lambda_1 & 0 & 0 \\ 0 & \lambda_2 & 0 \\ 0 & 0 & \lambda_3 \end{bmatrix} \tag{A.4}$$

The diagonal components of $\boldsymbol{\Lambda}_p$, referred to as $\boldsymbol{\lambda}_p \in \mathbb{R}^{3\times 1}$, are related to $\boldsymbol{t}_p = [t_1, t_2, t_3, t_4, t_5, t_6]^T$, the linear form of $\boldsymbol{T}_p$, through $\boldsymbol{\lambda}_p = \boldsymbol{U}\boldsymbol{t}_p$, where $\boldsymbol{U}(\alpha, \beta, \gamma) \in \mathbb{R}^{3\times 6}$ is the linear form of the

rotation. If $\boldsymbol{U}$ is partitioned into three vectors, where each vector is $\boldsymbol{u}_p \in \mathbb{R}^{1\times 6}$, then $\boldsymbol{U}^T = \begin{bmatrix} \boldsymbol{u}_1^T & \boldsymbol{u}_2^T & \boldsymbol{u}_3^T \end{bmatrix}$, where $\boldsymbol{u}_1^T, \boldsymbol{u}_2^T, \boldsymbol{u}_3^T$ are defined in (A.5).

$$
\begin{aligned}
\boldsymbol{u}_1^T &= \begin{bmatrix}
\cos^2\alpha\cos^2\beta \\
(\cos\alpha\sin\beta\sin\gamma - \sin\alpha\cos\gamma)^2 \\
(\cos\alpha\sin\beta\cos\gamma + \sin\alpha\sin\gamma)^2 \\
2(\cos\alpha\cos\beta)(\cos\alpha\sin\beta\sin\gamma - \sin\alpha\cos\gamma) \\
2(\cos\alpha\sin\beta\sin\gamma - \sin\alpha\cos\gamma)(\cos\alpha\sin\beta\cos\gamma + \sin\alpha\sin\gamma) \\
2(\cos\alpha\cos\beta)(\cos\alpha\sin\beta\cos\gamma + \sin\alpha\sin\gamma)
\end{bmatrix} \\
\boldsymbol{u}_2^T &= \begin{bmatrix}
\sin^2\alpha\cos^2\beta \\
(\sin\alpha\sin\beta\sin\gamma + \cos\alpha\cos\gamma)^2 \\
(\sin\alpha\sin\beta\cos\gamma - \cos\alpha\sin\gamma)^2 \\
2(\sin\alpha\cos\beta)(\sin\alpha\sin\beta\sin\gamma + \cos\alpha\cos\gamma) \\
2(\sin\alpha\sin\beta\sin\gamma + \cos\alpha\cos\gamma)(\sin\alpha\sin\beta\cos\gamma - \cos\alpha\sin\gamma) \\
2(\sin\alpha\cos\beta)(\sin\alpha\sin\beta\cos\gamma - \cos\alpha\sin\gamma)
\end{bmatrix} \\
\boldsymbol{u}_3^T &= \begin{bmatrix}
\sin^2\beta \\
\cos^2\beta\sin^2\gamma \\
\cos^2\beta\cos^2\gamma \\
2(-\sin\beta)(\cos\beta\sin\gamma) \\
2(\cos\beta\cos\gamma)(\cos\beta\sin\gamma) \\
2(\sin\beta)\cos\beta\cos\gamma)
\end{bmatrix}
\end{aligned}
\tag{A.5}
$$

REFERENCES

[1] L Robledo, M Carrasco, and D Mery, "A survey of land mine detection technology," *International Journal of Remote Sensing*, vol. 30, no. 9, pp. 2399–2410, 2009.

[2] A. C. Gurbuz, W. R. Scott, and J. H. McClellan, "Location estimation using a broadband electromagnetic induction array," in *Detection and Sensing of Mines, Explosive Objects, and Obscured Targets XIV*, International Society for Optics and Photonics, vol. 7303, 2009, 73030U.

[3] K. Krueger, W. R. Scott, and J. H. McClellan, "Location and orientation estimation of buried targets using electromagnetic induction sensors," in *Detection and Sensing of Mines, Explosive Objects, and Obscured Targets XVII*, International Society for Optics and Photonics, vol. 8357, 2012, p. 83570D.

[4] K. R. Krueger, J. H. McClellan, and W. R. Scott, "Tensor amplitude extraction in sensor array processing," in *Acoustics, Speech and Signal Processing (ICASSP), 2013 IEEE International Conference on*, IEEE, 2013, pp. 3895–3899.

[5] S. L. Tantum and L. M. Collins, "Performance bounds and a parameter transformation for decay rate estimation," *IEEE transactions on geoscience and remote sensing*, vol. 41, no. 10, pp. 2224–2231, 2003.

[6] Y. Das, J. E. McFee, J. Toews, and G. C. Stuart, "Analysis of an electromagnetic induction detector for real-time location of buried objects," *IEEE Transactions on Geoscience and Remote Sensing*, vol. 28, no. 3, pp. 278–288, 1990.

[7] D. P. Economou, F. Shubitidze, B. Barrowes, and N. K. Uzunoglu, "Music algorithm applied to advanced emi sensors data for uxo classification," in *2011 International Conference on Electromagnetics in Advanced Applications*, 2011, pp. 1160–1163.

[8] T. M. Grzegorczyk and B. E. Barrowes, "Real-time processing of electromagnetic induction dynamic data using kalman filters for unexploded ordnance detection," *IEEE Transactions on Geoscience and Remote Sensing*, vol. 51, no. 6, pp. 3439–3451, 2013.

[9] K. R. Krueger, W. R. Scott, and J. H. McClellan, "Extracting target orientation for different electromagnetic induction sensing geometries," in *2014 IEEE Geoscience and Remote Sensing Symposium*, 2014, pp. 3156–3159.

[10] X. Liao and L. Carin, "Application of the theory of optimal experiments to adaptive electromagnetic-induction sensing of buried targets," *IEEE Transactions on Pattern Analysis and Machine Intelligence*, vol. 26, no. 8, pp. 961–972, 2004.

[11] F. Shubitidze, B. Barrowes, K. O'Neill, and I. Shamatava, "Advanced emi modeling and processing approaches for uxo discrimination," in *2006 International Conference on Mathematical Methods in Electromagnetic Theory*, 2006, pp. 126–131.

[12] J. E. Gabbay, "Numerical methods for computing the modal decomposition of the magnetic polarizability of conducting objects," PhD thesis, Georgia Institute of Technology, 2019.

[13] W. R. Scott Jr, G. D. Larson, C. E. Hayes, and J. H. McClellan, "Experimental detection and discrimination of buried targets using an improved broadband cw electromagnetic induction sensor," in *Detection and Sensing of Mines, Explosive Objects, and Obscured Targets XIX*, International Society for Optics and Photonics, vol. 9072, 2014, p. 90720C.

[14] W. R. Scott, "Broadband array of electromagnetic induction sensors for detecting buried landmines," in *Geoscience and Remote Sensing Symposium, 2008. IGARSS 2008. IEEE International*, IEEE, vol. 2, 2008, pp. II–375.

[15] D. Steinhurst, G. Harbaugh, J. Kingdon, T Furuya, D. Keiswetter, and D. George, "Emi array for cued uxo discrimination," ENVIRONMENTAL SECURITY TECHNOLOGY CERTIFICATION PROGRAM OFFICE (DOD) ARLINGTON VA, Tech. Rep., 2010.

[16] C. Bruschini, *A multidisciplinary analysis of frequency domain metal detectors for humanitarian demining*, THESIS_LIB. Faculty of Applied Sciences of the, 2002.

[17] K. Ho and P. Gader, "On the estimation of target depth using the single transmit multiple receive metal detector array," in *Detection and Sensing of Mines, Explosive Objects, and Obscured Targets XVII*, International Society for Optics and Photonics, vol. 8357, 2012, p. 835 709.

[18] M. Oezdemir, E. L. Miller, and S. Norton, "Localization and characterization of buried objects from multifrequency array inductive data," in *Detection and Remediation Technologies for Mines and Minelike Targets IV*, International Society for Optics and Photonics, vol. 3710, 1999, pp. 26–36.

[19] W. M. Steedly and R. L. Moses, "The cramer-rao bound for pole and amplitude coefficient estimates of damped exponential signals in noise," *IEEE Transactions on Signal Processing*, vol. 41, no. 3, pp. 1305–1318, 1993.

[20] S. M. Kay, "Fundamentals of statistical signal processing, volume i: Estimation theory," 1993.

[21] J. C. Lagarias, J. A. Reeds, M. H. Wright, and P. E. Wright, "Convergence properties of the nelder–mead simplex method in low dimensions," *SIAM Journal on optimization*, vol. 9, no. 1, pp. 112–147, 1998.

[22] H. Vesselle and R. E. Collin, "The signal-to-noise ratio of nuclear magnetic resonance surface coils and application to a lossy dielectric cylinder model. i. theory," *IEEE Transactions on Biomedical Engineering*, vol. 42, no. 5, pp. 497–506, 1995.

[23] C. E. Baum, "Low-frequency near-field magnetic scattering from highly, but not perfectly, conducting bodies," in *Detection and identification of visually obscured targets*, CRC Press, 1998, ch. 6, pp. 163–218.

[24] K. R. Krueger, "Model design for algorithmic efficiency in electromagnetic sensing," PhD thesis, Georgia Institute of Technology, 2013.

[25] C. E. Hayes, W. R. Scott, and J. H. McClellan, "Low-rank model for wideband electromagnetic induction sensors," *IEEE Geoscience and Remote Sensing Letters*, vol. 14, no. 12, pp. 2413–2417, 2017.

[26] C. E. Hayes, J. H. McClellan, and W. R. Scott, "Low-rank physical model recovery from low-rank signal approximation," in *Acoustics, Speech and Signal Processing (ICASSP), 2017 IEEE International Conference on*, IEEE, 2017, pp. 3131–3135.

[27] J. E. Gabbay and W. R. Scott, "A simple method for computing discrete spectrum relaxations of body of revolution targets using eigenvalue decomposition," in *2012 IEEE International Geoscience and Remote Sensing Symposium*, IEEE, 2012, pp. 582–585.

[28] W. R. Scott and G. D. Larson, "Measured dipole expansion of discrete relaxations to represent the electromagnetic induction response of buried metal targets," in *Detection and Sensing of Mines, Explosive Objects, and Obscured Targets XV*, International Society for Optics and Photonics, vol. 7664, 2010, 76640E.

[29] S. L. Tantum and L. M. Collins, "A comparison of algorithms for subsurface target detection and identification using time-domain electromagnetic induction data," *IEEE Transactions on Geoscience and Remote Sensing*, vol. 39, no. 6, pp. 1299–1306, 2001.

[30] W. R. Scott, "Broadband electromagnetic induction sensor for detecting buried landmines," in *Geoscience and Remote Sensing Symposium, 2007. IGARSS 2007. IEEE International*, IEEE, 2007, pp. 22–25.

[31] M. A. Reed and W. R. Scott, "Optimization and analysis of wire-wound coil heads for emi systems," *IEEE Sensors Journal*, vol. 19, no. 5, pp. 1672–1682, 2018.

[32] K. B. Petersen and M. S. Pedersen, *The matrix cookbook (version: November 15, 2012)*, 2012.

[33] C. Eckart and G. Young, "The approximation of one matrix by nother of lower rank," *Psychometrika*, vol. 1, pp. 211–218, 1936.

[34] G. W. Stewart, "Perturbation theory for the singular value decomposition," Tech. Rep., 1998.

[35] G. Golub and V. Pereyra, "Separable nonlinear least squares: The variable projection method and its applications," *Inverse problems*, vol. 19, no. 2, R1, 2003.

[36] M.-H. Wei, "Electromagnetic induction spectroscopy for the detection of subsurface targets," PhD thesis, Georgia Institute of Technology, 2012.

[37] A. J. Kerr, W. R. Scott, and J. H. McClellan, "Performance analysis of parameter estimation in electromagnetic induction data," *IEEE Transactions on Geoscience and Remote Sensing*, 2019.

[38] C. E. Hayes, J. H. McClellan, W. R. Scott Jr, and A. J. Kerr, "Improved electromagnetic induction processing with novel adaptive matched filter and matched subspace detection," in *Detection and Sensing of Mines, Explosive Objects, and Obscured Targets XXI*, International Society for Optics and Photonics, vol. 9823, 2016, 98230E.

VITA

Andrew James Kerr was born in Charlotte, North Carolina on August 22, 1991, but grew up in Atlanta, Georgia. He received the B.S. degree in Electrical Engineering (summa cum laude) from Auburn University in 2013, and the M.S. and Ph.D. degrees in Electrical and Computer Engineering from the Georgia Institute of Technology in 2016 and 2020, respectively. His research interests include detection and estimation theory, radar signal processing, electromagnetics, and array processing. He is also a Research Engineer at the Georgia Tech Research Institute, where he has worked since May 2015.